INVESTIGATIONS OF THE STRUCTURAL CHANGES IN PROAPOPTOTIC PEROXIDASE-ACTIVE CARDIOLIPIN-BOUND CYTOCHROME C AND LIQUID-GEL PHASE TRANSITIONS IN LIPOSOMES USING SOLID STATE NMR SPECTROSCOPY

by

Abhishek Mandal

BS, Temple University, 2011

Submitted to the Graduate Faculty of

School of Medicine in partial fulfillment

of the requirements for the degree of

Doctor of Philosophy

University of Pittsburgh

2016

UNIVERSITY OF PITTSBURGH

SCHOOL OF MEDICINE

This dissertation was presented

by

Abhishek Mandal

It was defended on

November 30, 2016

and approved by

Ron Wetzel, Professor, Structural Biology

Jinwoo Ahn, Assistant Professor, Structural Biology

Valerian Kagan, Professor, Environment and Occupational Health, Chemistry, Pharmacology and Chemical Biology, Center for Free Radical and Antioxidant Health

Dissertation Advisor: Patrick van der Wel, Assistant Professor, Structural Biology

SOLID STATE NMR STUDIES OF PEROXIDASE ACTIVE CARDIOLIPIN BOUND CYTOCHROME C AND LIQUID-GEL PHASE TRANSITIONS IN LIPOSOMES

Abhishek Mandal, PhD

University of Pittsburgh, 2016

Mitochondrial cytochrome c (cyt-c) plays a key role in the activation of intrinsic apoptosis. Cyt-c gains a new function under apoptotic conditions; the peroxidation of mitochondrial lipid cardiolipin (CL) by cyt-c is a required step in the intrinsic apoptosis pathway. Understanding the mechanism of this alternate functionality in cyt-c has implications for treatment of neurological diseases like Huntington's disease and in cancer. In order to gain insights into this mechanism, structural and dynamical information on the membrane bound protein is required. Solid-state nuclear magnetic resonance (ssNMR) provides an array of tools to study this system and extract necessary structural and dynamical information on the protein as well as the membranes. In this thesis, magic-angle-spinning (MAS) NMR and static ssNMR are used in conjunction with various other biophysical tools to gain insights into the mechanism of cyt-c's peroxidase activity.

The effect of lipid peroxidation by cyt-c during apoptosis has also been implicated in modulating the structure, dynamics and behaviour of mitochondrial membranes, including facilitating pore formation in cyt-c-bound liposomes [1-3]. An understanding of lipid structure and phase behaviour has tremendous bearing on the study of lipids, membrane proteins and cryoprotection in general and cyt-c's role in apoptosis in particular. MAS NMR is used here to investigate the link between the freezing point depression of water and the lowering of the lipid transition temperature.

One of the requirements to performing MAS NMR is a method of sample preparation that provides highly concentrated samples in tiny microliter sized MAS sample rotors. Additionally,

for biological samples, as the ones under study here, it is very important to maintain hydration of the sample at all times in order to preserve function of the protein and the membranes, prevent damage to the sample, obtain better quality NMR spectra and most importantly, maintain biological relevance. Thus, the design and use of an ultracentrifuge based packing tool, that fulfills the requirements listed above, is discussed and illustrated here.

TABLE OF CONTENTS

LIST OF TABLES

LIST OF FIGURES

PREFACE

I owe heartfelt gratitude to the many people in my life that helped me in my journey towards completing my graduate studies. First of all I would like to thank my advisor and mentor, Dr. Patrick van der Wel, for supporting me through the typical ups and downs in the life of a graduate student. I am thankful for having the opportunity to work with him and learn from him, and especially for his patience, understanding and help when I wasn't able to keep up. I owe him many thanks for not only teaching me everything I know about NMR but also for pushing me to learn many skills outside the lab. His impressive grasp on the detailed and complete workings of solid state NMR *and* the biological background of all the different projects in the lab was amazing and *inspiring* to me. The lessons in the importance of proper (scientific or non-scientific) communication is one of the most useful skills I have picked up during my graduate studies and one that I hope will serve me well in my future career. And finally, I owe him thanks for pushing me to be my best self (especially when I really needed it) in order for me to get here. I would also like to thank my thesis committee for their helpful advice and feedback on my research, and for helping me in my journey from the start of my PhD candidacy to this defense.

I am incredibly grateful to Dr. Cody L. Hoop for being an amazing mentor. She taught me the practical aspects of NMR, and mentored me both during, and after her time in the lab. I am thankful for the support she provided during the rough times and grateful for the fun times. I would also like to thank Jennifer C. Boatz and Dr. Hsiang-Kai Lin for being a core part of my support group in the last few years. Together, the three of them were key in my success here. I especially appreciate them for not only their technical expertise in the lab but their friendship outside it. I will remember the many fun times we had and all the cool things we got to do together, even if I don't want to necessarily do all of them again (e.g. running another 5K anytime soon).

I would also like to thank my fellow MBSB graduate students, and particularly Dr. Sean Carney, Muwen (Ben) Kong, Ryan Slack and Patricia Campbell. I am indebted to them for their help and kindness to me throughout my time here in matters both academic and personal. I will forever cherish the many friendships fostered during my graduate studies here at Pitt.

Finally, I would like to thank my family and friends for their steadfast support these past five years. I am in eternal gratitude to my parents for the sacrifices they made to get me here and my only wish is to make them proud and happy. I am also incredibly grateful for all the prayers that my parents and sister sent on my behalf. You guys, I think it worked!

LIST OF ABBREVIATIONS

AFM	Atomic force microscopy
AR	Amplex red
CL	Cardiolipin
CP	Cross polarization
CSA	Chemical shift anisotropy
Cyt-c	Cytochrome c
DARR	Dipolar assisted rotational resonance
DLS	Dynamic light scattering
DMPC	1,2-dimyristoyl-*sn*-glycero-3-phosphocholine
DOPC	1,2-dioleoyl-*sn*-glycero-3-phosphocholine
DSC	Differential scanning calorimetry
FTIR	Fourier transformed infrared spectroscopy
IMM	Inner mitochondrial membrane
IMS	Intermembrane space
INEPT	Insensitive nuclei enhanced by polarization transfer
LUV	Large unilamellar vesicle
MAS NMR	Magic-angle-spinning nuclear magnetic resonance
MLV	Multilamellar vesicle

OMM	Outer mitochondrial membrane
OPPC	1-oleoyl-2-palmitoyl-*sn*-glycero-3-phosphocholine
P/L	Protein to lipid molar ratio
POPC	1-palmitoyl-2-oleoyl-*sn*-glycero-3-phosphocholine
PUFA	Polyunsaturated fatty acid
ROS	Reactive oxygen species
SOPC	1-stearoyl-2-oleoyl-*sn*-glycero-3-phosphocholine
ssNMR	Solid-state nuclear magnetic resonance
TEM	Transmission electron microscopy
TM	Melting temperature (denotes transition from liquid crystalline phase to gel phase)
TOCL	1’,3’-bis[1,2-dioleoyl-*sn*-glycero-3-phospho]-*sn*-glycerol (tetraoleoyl cardiolipin)
TPPM	Two pulse phase modulation
UCR	Ultracentrifuge rotor

1.0 INTRODUCTION

1.1 CYTOCHROME C'S ROLE IN PROGRAMMED CELL DEATH

Mitochondrial cytochrome c (cyt-c) is a 105 residue protein whose normal function is in the transfer of electrons from Complex III to Complex IV in the electron transfer pathway for the production of adenosine triphosphate (ATP). Cyt-c has also been implicated to play a key role in activating intrinsic apoptosis, a closely regulated cell death mechanism. A complete understanding of intrinsic apoptosis has implications for treatment of neurological diseases like Huntington's disease [4, 5], where blocking this pathway has been shown to be protective, as well as cancer [6, 7], where it would be beneficial to trigger this pathway in affected cells. A required signaling event in this apoptotic pathway is the peroxidation of mitochondrial lipid cardiolipin (CL) by cyt-c [8]. Normally, cyt-c has limited peroxidase activity, but binding to CL during apoptosis increases this drastically. The purpose of this thesis is to investigate the mechanism of this very important activity involving cyt-c.

1.1.1 Intrinsic apoptotic pathway

Apoptosis, or as it is sometimes called "programmed cell death", is a very strictly regulated biological process whereby cell contents are systematically degraded leading eventually to cell death. Apoptosis is a distinct process from necrosis and can be easily distinguished based on key morphological differences that the cells undergo in each process [9]. There are two main pathways that cells use to initiate apoptosis, extrinsic and intrinsic apoptosis. The difference between the two pathways lies in the origin of the initiation signal that activates apoptosis. Extrinsic apoptosis is initiated when the apoptotic signal originates outside the cell and activates "death receptors", which are members of the tumor necrosis factor receptor superfamily. However, intrinsic apoptosis relies on non-receptor mediated stimuli that produce intracellular signaling events involving the mitochondria (Figure 1.1).

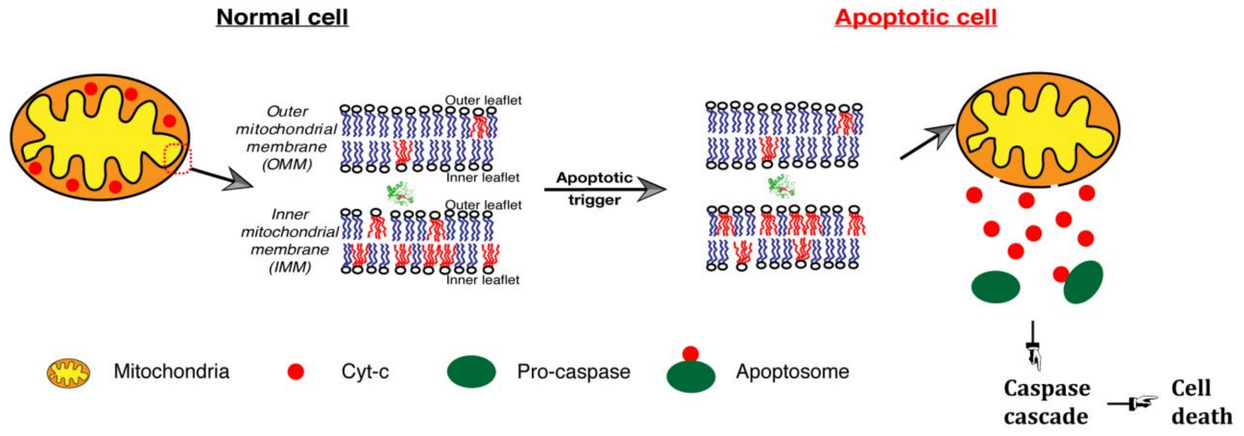

Figure 1.1. Location of CL and cyt-c in healthy and apoptotic cell

In a normal, healthy cell, cyt-c is located in the intermembrane space (IMS) and cardiolipin (lipids with red acyl chains) is sequestered primarily in the inner leaflet of the inner mitochondrial membrane (IMM). During apoptosis CL is redistributed in the inner mitochondrial membrane and allows for cyt-c to bind and oxidize the lipids. Eventually this is followed by the release of cyt-c from mitochondria to the cytosol where it binds and activates pro-caspases to form apoptosomes that lead to cell death.

Upon initiation of the intrinsic apoptotic pathway, the mitochondrial membrane undergoes changes, particularly in the distribution of CL amongst the inner and outer leaflet of inner mitochondrial membrane (IMM). This exposes cyt-c, normally sequestered in the mitochondrial intermembrane space (IMS) (Figure 1.1), to CL, whereupon cyt-c binds to CL and gains lipid peroxidase activity. The peroxidase-active cyt-c then oxidizes CL and subsequently is released into the cytosol (Figure 1.1). Upon release of cyt-c into the cytosol, it binds and activates Apoptotic protease activating factor 1 (Apaf-1) [10]. Normally, Apaf-1 is an inactive monomer in solution, but upon binding to cyt-c (at an Apaf-1 to cyt-c ratio of 1:1) it forms a quaternary structure consisting of seven Apaf-1/cyt-c complexes [11]. The activated complex, known as apoptosome, then binds and triggers procaspase-9, which repeats the same on further downstream caspases, eventually leading to cell death.

1.1.2 Disruption of cardiolipin asymmetry

Since CL binding is thought to enhance the lipid peroxidase activity of cyt-c, it is important to note that under normal physiological conditions, cyt-c does not have access to CL in large concentrations. This acts as a safeguard and prevents the cell from committing itself to intrinsic apoptosis unless specifically triggered. Most of the CL is normally sequestered in the inner leaflet of the IMM [12] away from cyt-c which resides in the IMS (Figure 1.1). During intrinsic apoptosis, this balance is disrupted and CL population is redistributed within the IMM and starts being exposed to the IMS [8] (Figure 1.1). There is a rearrangement of CL population from the inner leaflet of the IMM to the outer leaflet of the IMM. This allows cyt-c in the IMS to have increased access to CL thus activating its lipid peroxidase activity eventually leading to its release from mitochondria and subsequently to cell death.

1.1.3 Lipid peroxidase activity of cytochrome c

It has been established that prior to release from mitochondria, cyt-c gains a new function, i.e. it becomes a potent lipid peroxidase with high specificity for CL [13]. As a result of gaining this function, cyt-c catalyzes the peroxidation of CL and this activity has been shown to be a necessary step in the series of downstream effects that lead to the release of cyt-c from mitochondria and results in cell death [8]. Thus, CL is not only required for the activation of lipid peroxidase activity of cyt-c but is also the substrate for the peroxidase-active cyt-c. While soluble cyt-c present in the IMS has low levels of peroxidase activity, the peroxidase activity increases significantly as a consequence of selective binding to CL [13, 14].

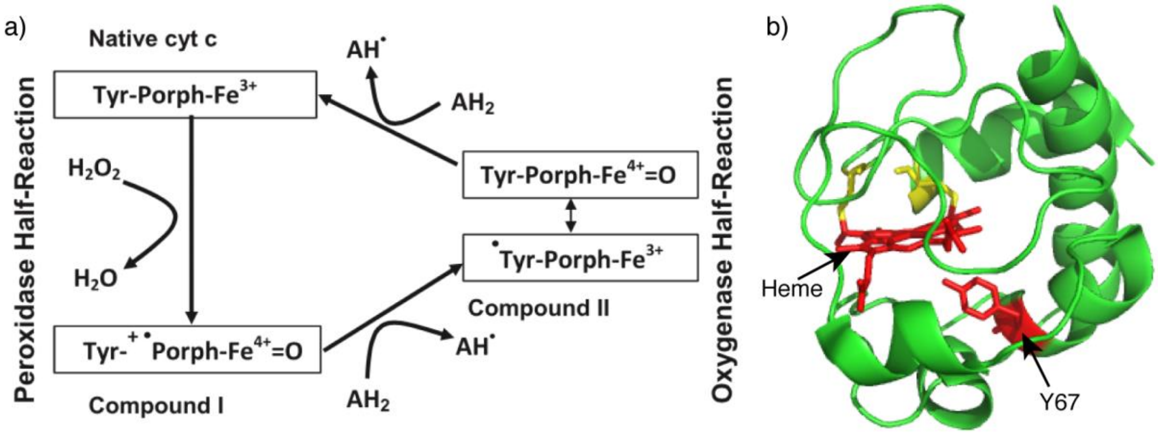

Figure 1.2. Role of heme and Y67 in peroxidase activity of cyt-c

a) This figure from [15] illustrates the chemical reactions responsible for the peroxidase activity of the cyt-c as well as the role of residue Y67 in this process. Figure reprinted from [15], Copyright 2011, with permission from Elsevier. b) This x-ray structure of cyt-c from ref [16] is used to highlight the two peroxidase active catalytic sites in the protein, the heme and Y67 residue (colored in red). The covalent attachment of the heme moiety to two cysteines, C14 and C17 (colored in yellow), is also marked in the figure.

The peroxidase activity of cyt-c is a cycle of chemical reactions composed of two half reactions: a peroxidase half-reaction and two oxygenase half-reactions [15] (Figure 1.2a). The peroxidase half-reaction relies on oxidizing chemicals like hydrogen peroxide or fatty acid hydroperoxides to oxidize and activate cyt-c, with the latter increasing the peroxidase half-reaction by three orders of magnitude compared to hydrogen peroxide and other small organic hydroperoxides. This catalysis effect of the hydroperoxides acts as a signal amplifier during intrinsic apoptosis to rapidly peroxidize the CLs in the IMM. The activated cyt-c from the peroxidase half-reaction is missing two electrons, one from the porphyrin moiety of the heme and one electron from the iron to yield a charged, radical [15] (Figure 1.2a). This activated cyt-c is then recovered back to the native state by two one-electron reactions in the oxygenase half-reactions starting with an intermediate where the porphyrin radical is first reduced by oxidizing the Y67 residue in cyt-c [15] (Figure 1.2a). The oxygenase half-reaction recovers the native state of cyt-c by oxidizing as its substrate CL.

Lipid peroxidase activity of cyt-c thus requires that CL acyl chains have access to the catalytic sites on cyt-c, which are the heme group and Y67 [15], shown in Figure 1.2b. It is important to note that unlike many other heme-containing proteins, cyt-c’s heme group is covalently attached to the protein at two sites, C14 and C17 (Figure 1.2b). In addition to the covalent attachment at those two sites, H18 and M80 axially coordinate the iron atom at the center of the heme. Altogether, this makes the heme moiety a very stable component of cyt-c. Thus, a crucial open question is regarding the structural changes in the membrane bound cyt-c that allow its covalently attached heme to catalyze the peroxidation of CL acyl chains in the membrane core. This thesis reports on the progress made in answering this question.

1.2 LIPID PHASE BEHAVIOUR

Biological activity of membrane-associated proteins, both peripheral and integral, is reliant on the structure and dynamics of the membranes encapsulating various organelles and the cell itself. Many important biological processes require modifications in the structure of the bilayers, and some of these are briefly discussed here. Physiological conditions in a cell dictate that lipid bilayers exist primarily in a mobile, liquid crystalline (or lamellar) phase (L_α) (Figure 1.3b). However, changes in conditions and lipid composition can induce alterations in the lipid phase behaviour. Changes in hydration and temperature can result in lipid phase transition from the highly dynamic liquid crystalline phase to the gel phase (L_β), which is characterized by a rigidification of the membrane (Figure 1.3a). The temperature required to induce the transition between the liquid crystalline and gel phase is defined as the transition temperature (T_m). Under physiological conditions, lipids in gel phase play an important role in the formation of lipid rafts and for sequestering membrane proteins to activate cell-signaling mechanisms [17].

Lipids in both liquid-crystalline and gel phase still form bilayers. However, under certain conditions lipid bilayers can undergo a transition to non-bilayer phases that can have significant physiological implications. For example, peroxidation of CL has been shown to increase the pore formation activity of certain mitochondrial proteins like Bax, promoting the release of cyt-c during apoptosis [1]. The mechanism of pore formation was indicated to involve a transition in the lipid phase from liquid crystalline to inverted hexagonal phase [1] (Figure 1.3c). An important predictor of the formation of the non bilayer H_{II} phase is the shape of the lipids in a membrane. Lipids with a small headgroup volume compared to the volume of the acyl chains (like cardiolipins in mitiochondria) have a higher propensity to form H_{II} phase. The ability to form inverted hexagonal phase in lipids also has important implications in many cellular processes like membrane fusion and fission and insertion of transmembrane proteins [18, 19]. Additionally, cyt-c itself has been implicated in the formation of non-bilayer, inverted hexagonal phase during apoptosis leading to pore formation and its subsequent release from mitochondria [20, 21]. Thus, comprehension of the lipid structure and dynamics has significant implications for obtaining a complete picture of cyt-c's role in apoptosis. Chapter 4.0 describes the way that MAS NMR is used to determine the depression in the freezing point of water and the lowering of the lipid liquid-gel phase transition temperatures under MAS conditions.

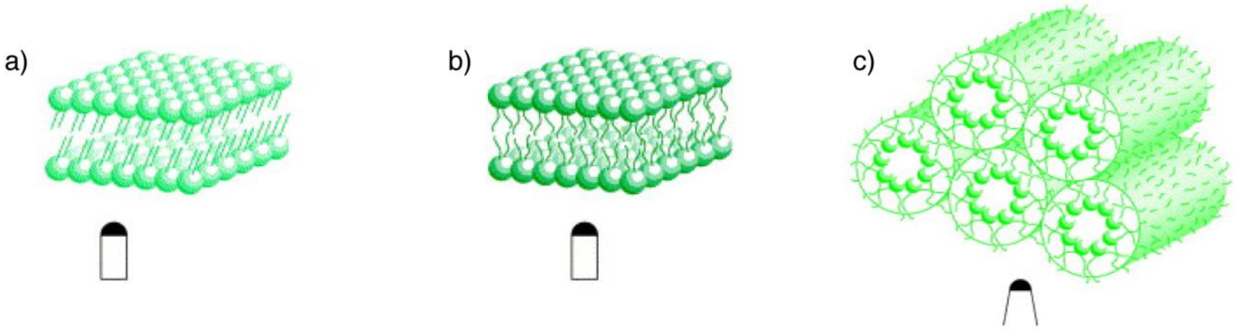

Figure 1.3. Possible lipid structures under physiological conditions

Figure adapted from ref [22] illustrates three lipid structures found under physiological conditions. (a) Lipid bilayer in a gel phase (L_β), (b) lipid bilayer in liquid crystalline phase (L_α) and (c) lipids in an inverted hexagonal phase (H_{II}). Figure reprinted from [22], Copyright 1998, with permission from Elsevier.

1.3 INVESTIGATIVE METHODOLOGIES

1.3.1 Simulating pro-apoptotic mitochondrial conditions for the study

In order to mimic the pro-apoptotic conditions in mitochondria where cyt-c becomes a lipid peroxidase, specially formulated liposomes were used in the studies. Since the system under study is a peripherally binding protein, there are multiple reasons for using large unilamellar vesicles (LUVs) versus multilamellar vesicles (MLVs). LUVs maximize the lipid-protein binding compared to MLVs as cyt-c only binds to the outer layer of the liposome. Thus LUV samples maximize the ratio of protein to lipids in the final samples compared to MLVs. Lipids were mixed in chloroform to contain 20 mol% of CL and 80 mol% of 1,2-dioleoyl-*sn*-glycero-3-phosphocholine. This is to simulate the outer leaflet patches in the IMM, rich in CL that we believe to be the binding sites for cyt-c. The rehydrated liposomes were subjected to freeze-thawing and extrusion to obtain 200 nm sized LUVs, to which U-^{13}C,^{15}N or unlabeled cyt-c is added before packing the samples in the 3.2 mm MAS rotors. This identical protocol of sample preparation was used both in structural studies by magic-angle spinning (MAS) nuclear magnetic resonance (NMR) spectroscopy and FTIR, as well as in all complementary functional studies using fluorescence based peroxidase activity assays.

1.3.2 Considerations for MAS NMR experiments

There are many benefits to performing MAS NMR; these experiments can be done on samples that are neither readily soluble nor crystallizable, and thus cannot be subjected to solution NMR or X-ray crystallography studies. This allows for the use of MAS NMR in the study of membrane-associated proteins, as is the case with the system under study here. However, there are a few key requirements that need to be fulfilled before performing MAS NMR experiments on biological samples. One of the main requirements is that the samples under study need to be isotopically labeled before MAS NMR experiments are conducted on these samples. Additionally samples need to be concentrated into microliter sized MAS rotors at large concentrations to achieve good signal/noise sensitivity in the NMR signal. While packing, it is also very important to maintain hydration of the sample during the entire process as dehydration can lead to irreparable sample damage due to the separation of the protein from lipid-rich domains, non-bilayer phase formation and increased propensity for gel phase formation [23-25].

High-density packing of samples while maintaining hydration is a non-trivial concern, especially for samples that do not sediment or pellet easily. For example, samples with liposomes tend to form pellets of high viscosity that are difficult to handle and do not easily transfer without significant sample loss. Thus, Chapter 2.0 describes the rationale, design and use of custom built ultracentrifugal packing devices that can easily and routinely pack difficult MAS samples, like those containing lipid vesicles.

1.3.3 Solid State NMR background

Solid-state NMR (ssNMR) is increasingly becoming an essential tool in the suite of biophysical techniques available to study important biological systems. SSNMR allows for a molecular level study of samples that are not readily water-soluble, providing structural and dynamical information on the system under investigation using both static and MAS NMR techniques. A brief overview of some of the important ssNMR concepts and applications are provided here.

1.3.3.1 Magic angle spinning NMR

One of the key features of solution NMR is the requirement of fast molecular tumbling of the sample molecule. This means that the sample needs to be dissolved in a soluble medium where the sample can experience fast tumbling. The necessity of fast molecular tumbling thus imposes a size limit on the molecules that can be studied using solution NMR methods as larger molecules experience slower tumbling rates [26]. Additionally, in the case of biological molecules it also requires that the sample be water-soluble. This additional constraint rules out the use of solution NMR in the study of significant, biologically relevant, insoluble complexes such as protein aggregates (e.g. amyloid like fibrils in Huntington's disease) and protein-lipid complexes as is the case in the study of membrane proteins. Application of static ssNMR to study such samples results in spectra with very broad peaks and thus low sensitivity, making it unsuitable for meaningful analysis. MAS NMR overcomes these limitations by rapidly spinning the NMR sample at an angle of 54.7° to the magnetic field of the NMR spectrometer. This fast spinning at the "magic angle" simulates the molecular tumbling experienced by molecules in solution, allowing one to obtain sharp peaks in the NMR spectra analogous to solution NMR data.

1.3.3.2 Chemical shift anisotropy

NMR signals are very sensitive to local chemical structure and dynamics. In an NMR sample, each unique atom in a particular orientation gives rise to a unique chemical shift in an NMR spectrum upon the application of a specific magnetic field to the sample. This phenomenon of orientational dependence of the chemical shifts is called chemical shift anisotropy (CSA). However, if a sample experiences rapid isotropic motion, i.e., it is rotating in all possible directions, then a single, averaged peak at the isotropic chemical shift is observed. In solution NMR, the isotropic Brownian motion of the molecules leads to an averaging of the CSA resulting in relatively sharp peaks for every unique atom in an NMR sample. In MAS NMR, a similar effect is achieved by spinning the sample at an angle of 54.7° (the magic angle) from the applied magnetic field in order to obtain narrow peaks at isotropic chemical shifts analogous to the data obtained from solution NMR.

Contrary to solution and MAS NMR, in static ssNMR the CSA is not averaged out and instead can be used to extract structural information on the orientation of the samples under study. Additionally, in lipid samples the motion of the individual lipids in the plane of the bilayer causes changes in the average orientation of the phosphate head group relative to the acyl chain. Thus, ^{31}P static ssNMR is an incredibly useful tool for the study of lipid structure and dynamics. ^{31}P static ssNMR data can be used to easily determine information about the lipid structure and dynamics [27]. As illustrated in Figure 1.4, the peak shape of a ^{31}P NMR spectrum can be used to easily distinguish the presence of different lipid structures present in a sample. Additionally, the peak can be fit to obtain key parameters to calculate the CSA of the lipids in the sample.

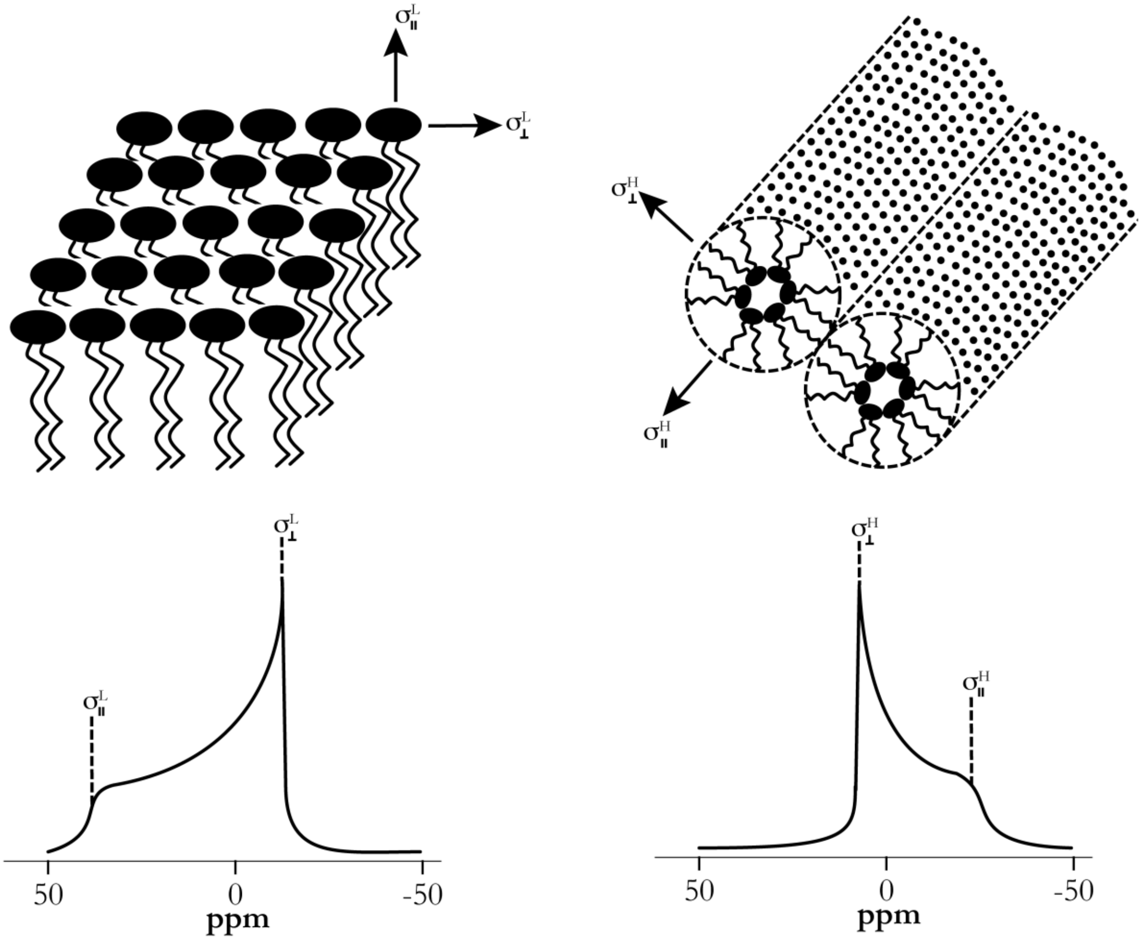

Figure 1.4. Using ^{31}P ssNMR to study lipid structure

Figure adapted from ref [27] illustrates two possible lipid structures a membrane can adopt under physiological conditions: liquid-crystalline (L_{α}) phase lipids (top left) and inverted hexagonal (H_{II}) phase lipids (top right). Below them are simulated ^{31}P NMR spectra for the L_{α} phase lipids (bottom left) and H_{II} phase lipids (bottom right). Figure adapted from [27], Copyright 1984, with permission from Elsevier.

1.3.3.3 MAS NMR experiments

In this study various MAS NMR experiments were used to probe the structure and dynamics of system under investigation. These experiments are used in this work to detect and record ^{1}H, ^{13}C, ^{15}N, and ^{31}P chemical shifts. Some of these experiments are briefly described here.

Cross Polarization (CP) (ref. [28]) – This is a MAS NMR experiment that is used to transfer polarization from nuclei with high sensitivity (donor nuclei, usually ^{1}H) to one with lower sensitivity (acceptor nuclei, ^{13}C and ^{15}N for the experiments used here) using dipolar coupling. Dipolar coupling is the interaction between two nuclei through space due to the magnetic dipole generated by one nucleus affecting another nucleus' magnetic dipole. Briefly, the protons in the sample are excited by the application of radiofrequency (RF) pulse and then another pulse is applied simultaneously to the donor and acceptor nuclei to transfer polarization from the protons to the acceptor nuclei. NMR signal is acquired, obtaining signal from the acceptor nuclei (either the ^{13}C or ^{15}N atoms) while a low-powered RF pulse is applied on the ^{1}H channel (heteronuclear decoupling). The application of heteronuclear decoupling increases the NMR signal observed by reducing signal losses due to coupling between ^{13}C (or ^{15}N) and ^{1}H atoms. There are many decoupling schemes available for use in MAS NMR experiments and the primary one used in the work here is the two pulse phase modulated (TPPM) scheme [29]. The resulting spectrum is a 1D with either ^{13}C or ^{15}N chemical shifts of isotopically labeled carbon or nitrogen atoms. This experiment can also be used to obtain data on natural abundance samples such as lipids, as the presence of 1% naturally occurring ^{13}C atoms in these samples provide good sensitivity to be easily detected by NMR. The ssNMR studies described here always use natural abundance lipids. The CP experiment also forms the basic building block that facilitates polarization exchange between atoms/nuclei in many two- and three-dimensional (2D and 3D) MAS NMR experiments.

Insensitive Nuclei Enhanced by Polarization Transfer (INEPT) (ref. [30]) – This is another 1D experiment used to transfer polarization from high sensitivity nuclei to low sensitivity nuclei. This method uses scalar coupling, reliant on chemical bonds between two nuclei for the transfer of polarization from a donor nuclei to an acceptor nuclei. Unlike dipolar coupling, scalar or J-couplings are not averaged by dynamics and are thus well suited for use in samples containing dynamic protein or lipids. In NMR experiments there are many pathways that result in the loss of polarization/NMR signal which can affect final spectra. INEPT is very sensitive to one of these relaxation mechanisms called T_2 relaxation and thus suffers large signal losses for all but the most mobile sites. Only the most mobile atoms have long enough T_2 relaxation times to allow for enough signal acquisition to obtain detectable NMR peaks. As is the case with CP experiments, these experiments can also be used to build more complex multidimensional MAS NMR experiments.

Dipolar Assisted Rotational Resonance (DARR) – This is a 2D experiment where after the initial polarization transfer from protons to carbons (using a CP block), a subsequent transfer between the carbons is allowed for a specific amount of time (called the mixing time). ^{13}C NMR signals are detected both before and after the second transfer step. The resultant ^{13}C-^{13}C 2D spectrum has all individual carbons on the diagonal with cross-peaks indicating correlation between carbons that are close to each other. This information is used to generate intra- or inter-residue correlations between the carbons depending on the mixing time employed in the experiment. Modification of the second transfer step allows for the examination of carbons-carbon correlation at different distances.

NCACX – This is a 3D MAS NMR experiment that provides a ^{13}C-^{13}C spectrum at different ^{15}N frequencies. It also uses CP for the polarization transfer steps between ^{1}H and ^{15}N and ^{15}N and ^{13}C. This is one of the many triple-resonance experiments used to generate complete assignment of a protein by NMR [31]. In these studies, NCACX data is essential for the identification of specific Ala residues in cyt-c (Chapter 3.0

1.3.3.4 Manifestation of dynamics in ssNMR spectra

In addition to providing key structural insights on a molecular level, ssNMR provides tools to extract dynamical information on the proteins and lipids under study. Components of biological samples studied under physiologically mimicking conditions experience dynamics on varying timescales. For example, a soluble protein has a higher degree of freedom in its dynamics compared to a membrane bound protein. Additionally, lipid headgroups, which are in closer proximity to water molecules experience motion on a faster timescale than the hydrophobic acyl chains. Sample dynamics is an important parameter that can be used to selectively detect specific molecules in a biological system under study by ssNMR. In MAS NMR studies, the binding of a protein to lipid membranes significantly reduces the dynamics experienced by the protein, and this stabilization makes it become visible in a CP spectrum. Reducing the thermal motion of the protein by cooling the sample can further increase NMR signal in a CP spectrum (Section 3.3.2). In our studies, INEPT based experiments are programmed to detect molecules undergoing fast motion. Thus, only the very mobile protein residues and all lipid molecules are observed in these experiments. Furthermore, changes in dynamics experienced by the lipid molecules result in fluctuations in the lipid CSA that can be detected using ^{31}P static ssNMR experiments. The use of ssNMR experiments to discriminate and detect sample dynamics is further explored in the studies of membrane bound cyt-c in Chapter 3.0

2.0 ON THE USE OF ULTRACENTRIFUGAL DEVICES FOR ROUTINE SAMPLE PREPARATION IN BIOMOLECULAR MAGIC-ANGLE-SPINNING NMR

Mandal, A., Boatz, J.C., Wheeler, T. and van der Wel, P.C.A. (2017) On the use of ultracentrifugal devices for routine sample preparation in biomolecular magic-angle-spinning NMR, *manuscript in preparation*.

Author contributions: T.W. and P.v.d.W. designed the packing tool. T.W. fabricated the packing tool. A.M. prepared samples. A.M. packed samples. A.M. and J.C.B. performed MAS NMR experiments. J.C.B. performed TEM measurements. A.M. and P.v.d.W. wrote the manuscript.

A number of recent advances in the field of magic-angle-spinning (MAS) solid-state NMR have enabled its application to a range of biological systems of ever increasing complexity. To retain biological relevance, these samples are increasingly studied in a hydrated state. At the same time, experimental feasibility requires the sample preparation process to also attain a high sample concentration within the final MAS rotor. We discuss these considerations, and how they have led to a number of different approaches to MAS NMR sample preparation. We describe our experience of how custom-made (or commercially available) ultracentrifugal devices can facilitate a simple, fast and reliable sample preparation process. Whilst some groups have adapted such tools, in some cases to prepare samples for sedimentation NMR or freezing rotational diffusion of protein solutions at low temperature and high viscosity (FROSTY)-style

experiments, we argue for a more widespread adoption for routine sample preparation for MAS ssNMR.

2.1 INTRODUCTION

Biological solid-state NMR (ssNMR) has undergone tremendous development in recent years, providing new insights into the structure and dynamics of membrane proteins, protein aggregates, and a variety of other biologically interesting samples [32-37]. Most of these results stem from the use of magic angle spinning (MAS) ssNMR. The burgeoning application of MAS ssNMR for biological samples has been enabled by technological improvements in the equipment available for ssNMR. This includes higher magnetic fields, faster MAS, and improved probe designs [38-40]. An equally important contribution comes from improvements in sample preparation including increasing use of selective and extensive isotopic labeling strategies [41]. Together, these factors have improved the sensitivity and resolution that can be obtained by MAS ssNMR.

The improved performance of ssNMR enables the study of a variety of biological systems, whether aggregated proteins, membrane-bound proteins or membranes themselves. A key factor in the application of ssNMR over other structural techniques continues to be the ability to probe proteins (or other biomolecules) in an appropriate biological context. Proper sample hydration is critical in this respect [42]. Enzymatic protein activity is reliant on hydration [43, 44]. The folding and function of membrane proteins requires not only a lipid bilayer environment, but also a minimal level of hydration. Dehydration can have adverse impacts on membranes: lateral separation of membrane proteins from lipid-rich domains, formation of non-bilayer lipid phases and an increased propensity for gel phase formation can result [23-25]. Some of these dehydration-induced changes can be directly observed via ssNMR [42, 45-48]. In many cases, a lack of proper hydration results in reduced spectral quality, for instance due to the entrapment of multiple structural conformations that manifests itself as increased NMR line widths [49-52]. Thus proper sample hydration is critical in the design and execution of modern biomolecular ssNMR, and needs to be considered during the process of packing or preparing the actual samples.

The rotor packing process should achieve multiple goals: maximize signal/noise, ensure biological relevance, and be robust, reproducible and easy. Maximizing signal means the maximum sample needs to be packed into the small μL-sized volumes of typical MAS rotors, usually at the expense of excess buffer. Traditional MAS NMR packing methods have taken different approaches. One approach has been to pack and study samples that were completely dry, maximizing the amount of (labeled) protein or peptide, but also sacrificing biological relevance in the pursuit of maximum signal [53-55]. As noted above, this approach also often suffers from line broadening and reduced spectral quality. Other studies therefore have packed the rotor with dry material, but followed this with a controlled rehydration inside the rotor [56]. However, it is currently most common that samples are packed into the rotor in an already hydrated state. In some cases this still involves the controlled de- and re-hydration of the sample, which is however completed before, instead of after, packing the sample into the rotor [57, 58]. In other cases, once the protein (complex) of interest is reconstituted or assembled, dehydration of the samples is avoided. In such cases, centrifugation is typically employed to sufficiently concentrate the biological solids to fit them into the MAS rotor volume. One can centrifuge the hydrated sample into a dense pellet, and then transfer the latter into a rotor. The latter can be done by carefully scooping to sample with micro-spatulas [42], but this is time-consuming, and risks both sample losses and partial or local dehydration. An improved approach centrifuges these pre-condensed pellets into the rotor using funnel-shaped devices that fit in a tabletop (micro)centrifuge [59, 60]. This sometimes involves a fixed-angle tabletop centrifuge that could lead to an uneven packing of the sample material, which can compromise stable spinning during MAS.

Here we describe the approach that our lab has been using to pack all types of hydrated biological samples for MAS NMR. This approach combines the pelleting of the sample and the packing into the rotor into a single process, enabled by the use of swinging-bucket ultracentrifugal packing tools. It is designed to balance the need to maximize the signal/noise, maintain biological relevance and achieve easy reproducibility. We note that such devices are successfully used by ourselves [14, 61-67] and various other groups [50, 68, 69], but that there are many others that have not adopted this approach.

To the best of our knowledge, the earliest such application was described in the literature in 2009, when it was used for the packing of crystalline protein samples [68]. In subsequent years this methodology was also applied to the packing of amyloid fibrils [63, 70]. Around the same time the high centrifugal forces during MAS were used to sediment large soluble proteins, in methods known as sedimentation NMR and freezing rotational diffusion of protein solutions at low temperature and high viscosity (FROSTY) MAS NMR [71, 72]. This led to the use of ultracentrifugal packing devices to directly sediment soluble proteins into MAS rotor, during the packing process [69, 73]. In this work, we argue that these devices should serve as ideal packing tools for the routine preparation of all types of (hydrated) biological samples. Design considerations as well as applications are discussed, showing our everyday use of this approach as a standard practice when packing MAS ssNMR samples.

2.2 METHODOLOGY

2.2.1 Construction of sample packing tool

The ultracentrifugal packing devices were constructed in the Department of Cell Biology machine shop at the University of Pittsburgh, based on designs made by the authors. The packing device was converted from concept to 3D solid model using SolidWorks software package (Waltham, MA). Prior to fabrication, the 3D solid model was programmed for machining using Mastercam (Tolland, CT). Finally, individual parts were machined out of unfilled polyether ether ketone (PEEK) obtained from McMaster Carr (Elmhurst, IL) using a Hardinge GS-150 CNC (computer numerical controlled) lathe (Elmira, NY). As described, the tools are explicitly designed for use with Bruker-style MAS rotors, and for use in a swinging-bucket SW 32 Ti ultracentrifuge rotor from Beckman Coulter (Indianapolis, IN).

2.2.2 Sample packing protocol

An empty MAS NMR rotor, with the rotor drive cap removed, is placed into the open packing tool base. After manual assembly of the packing tool, the aqueous sample suspension is pipetted into the device’s funnel. Depending on preference, the device may be inserted into an empty centrifuge tube, in order to catch inadvertent sample leakage. The tube pictured in Figure 2.1a below is a Beckman Coulter (Indianapolis, IN) part number 344058 made out of Ultra-Clear^{TM}. The filled device is carefully inserted into one of the buckets of the swinging bucket rotor (Beckman Coulter SW 32 Ti). A second, counter-balance bucket is balanced carefully, by filling it with a second packing tool (see Results) and water. The packing process is then performed by ultracentrifugation for the specified times in a Beckman Coulter Optima L-100 XP ultracentrifuge at up to 32,000 RPM (~175,000 x *g*).

2.2.3 Preparation of the reference samples

The cytochrome-c containing sample was prepared as previously described [14]. Briefly, tetra-oleoyl-cardiolipin (TOCL) and di-oleoylphosphatidylcholine (DOPC), obtained in chloroform solution from Avanti Polar Lipids (Alabaster, AL), were mixed at a molar ratio of 1:4, dried under N_2 gas, further dried under vacuum and resuspended in 20mM HEPES (pH 7.4). The resuspended liposomes were subjected to freeze thawing and extrusion through 200 nm polycarbonate membranes to generate 200-nm diameter large unilamellar vesicles (LUVs), confirmed by DLS [14]. Pre-dissolved uniformly ^{13}C and ^{15}N (U-^{13}C,^{15}N) labeled horse heart cytochrome c, obtained by expression in *Escherichia coli*, was added to the LUVs. The vesicle-bound proteins were then packed into a MAS rotor using the described ultracentrifugal packing device, either by centrifugation at 143,000 x *g* for 3 hours and 175,000 x *g* for 4.5 hours, or by centrifuging at 143,000 x *g* for 5 hours. For more details see ref. [14].

Mutant huntingtin (htt) exon 1 samples were prepared as described [64]. U-^{15}N-labeled and U-^{13}C-labeled fusion proteins were expressed in *Escherichia coli* and purified. The purified proteins were mixed together after which aggregation was initiated upon cleavage of the fusion protein by factor Xa protease (Promega Corporation, Madison, WI). The amyloid-like fibrils that result were washed with buffer, and then packed into MAS rotors using the described ultracentrifugal packing device. Packing was done by first centrifuging the sample at 154,000 x *g* for one hour. Subsequently, 1 mL of buffer was used to rinse the original sample tube in order to recover residual sample that may have been left behind. The sample was then centrifuged a second time under identical conditions as the first round. A second rinse and a third centrifugation cycle was performed before the rotor was sealed for study by MAS NMR.

Nanofibers assembled by the acylated peptide amphiphiles were prepared as described [67], starting with site-specifically labeled peptides obtained by solid-phase peptide synthesis. The divalent peptide conjugate molecule featured a C_{18} organic tail attached to two identical gold-binding peptide sequences. The peptide sequence in the molecule was AYSSGAPPMPPF. In the construct studied, the methionine was oxidized prior to assembly of the entire molecule. The construct, named C_{18}-($PEP_{Au}^{M\text{-}ox}$)$_2$, featured U-^{13}C,^{15}N-labeling in residues A1 and P10. The mature assembled fibrils were packed into MAS rotors using the ultracentrifugal packing device, in a single step process involving ultracentrifugation for 1 h at 175,000 x *g*.

2.2.4 MAS ssNMR experiments

The huntingtin exon 1 fibril measurements were performed on an 800 MHz (18.8 T) spectrometer (Bruker Biospin, Billerica, MA), with a 3.2 mm HCN Bruker MAS ssNMR probe [64]. Experiments were performed at a set temperature of 275 K while spinning at 13 kHz. Using a CP contact time of 1.5 ms, 1000 scans were acquired with a RD of 3 s and an applied TPPM decoupling on ^{1}H at 83 KHz. All other experiments were performed on a wide-bore 600 MHz (14.1T) spectrometer (Bruker Biospin, Billerica, MA) using a 3.2mm HCN Bruker MAS ssNMR probe outfitted with an “EFree” coil. MAS NMR on cyt-c sample was performed at a sample temperature of 233 K while spinning at 8.33 KHz [14]. Using a CP contact time of 1 ms, 256 scans were collected with a RD of 3.2 s and an applied TPPM decoupling on ^{1}H at 83 KHz. Experiments on the C_{18}-dipeptide nanoparticles were performed at a set temperature of 277 K while spinning at 10 KHz [67]. Using a CP contact time of 1 ms, 1000 scans were obtained with a RD of 3 s and an applied TPPM decoupling on ^{1}H at 83 KHz.

2.2.5 Electron Microscopy and Atomic Force Microscopy

Transmission electron microscopy (TEM) and atomic force microscopy (AFM) measurements on htt exon 1 fibrils and C_{18}-dipeptide nanoparticles were performed as previously reported [64, 67]. The previously unpublished TEM data in Figure 2.4a were obtained as follows. Unlabeled cyt-c obtained from Sigma Aldrich (St. Louis, MO) was added to liposomes at a lipid to protein molar ratio of 40:1. The liposomes were prepared as described above using a mixture of TOCL, DOPC and cholesterol at a molar ratio of (0.15:0.75:0.10) obtained from Avanti Polar Lipids. The sample was diluted in half with ddH_2O and absorbed on to a freshly glow discharged carbon coated copper EM grid for at least one minute. Excess sample was wicked away with a filter paper. The grid was stained with 1% (wt/vol) uranyl acetate. The grid was allowed to fully air dry before being images were acquired. The TEM measurements were performed on a Technai T12spirit transmission electron microscope (FEI, Hillsboro, OR) operating at 120 kV and equipped with an UltraScan 1000 CCD camera (Gatan, Pleasanton, CA).

2.3 RESULTS

2.3.1 MAS NMR sample packing design considerations

The process of MAS NMR sample packing essentially constitutes the concentrating of hydrated 'solid' samples of interest, ideally while avoiding dehydration of the sample. The most common and convenient way of achieving this is by pelleting the solid (or soluble) macromolecules from their initial aqueous suspension or solution by centrifugation. To avoid dehydration and ensure time efficiency, this ideally is done in a one-step fashion directly into the rotor. Finally, the resulting pellet should not only be compact, but also evenly distributed in the MAS rotor to avoid compromising rotor stability during the MAS. The latter argues against use of fixed-angle centrifuge rotor systems.

All these requirements are conveniently and perfectly met with the use of funnel-shaped packing devices designed for use in swinging bucket rotors. For the most general applicability, the device should permit pelleting of all kinds of (hydrated) ssNMR samples. The time and speed of centrifugation required for pelleting the sample depends on the nature of the sample. Protein crystals and aggregates often have densities that are significantly larger than that of water (1.24 to 1.54 g/mL [74, 75]), which facilitates pelleting at relatively moderate g-forces, even in small table top centrifuges [76]. Samples featuring lipid LUVs require the use of ultracentrifugation, due to the small density differences (~1.03 g/mL) with the aqueous buffer. Ultracentrifugation can also be used to sediment soluble protein complexes out of solution, for study by ssNMR [69, 71].

Thus, in 2009 we set out to design an ultracentrifugal packing device, with similar features as those used (and described) by others in the ssNMR community [68, 69, 73, 77].

Primary goals were to obtain a robust and long-lived tool (i.e. a simple design), limit sample losses during tool usage, assure ease of use, and speed up the sample preparation process. The guiding principle was to start with a typical Eppendorf-style microcentrifuge-tube-sized sample (~1 mL) of a suspension or solution and pellet the “solid” fraction into the μL-sized MAS rotor in a single step.

Table 2.1. Properties of swinging-bucket rotors available for Beckman Coulter ultracentrifuges

Ultracentrifuge rotor (UCR)	Max spinning rate (RPM)	G-force on sample	Maximum swinging bucket volume (ml)
SW 32 Ti	32,000	175,000	38.5
SW 40 Ti	40,000	285,000	14
SW 60 Ti	60,000	485,000	4

2.3.2 Packing device design

To allow for the pelleting of a broad range of samples, we designed a tool that can withstand and achieve high g-forces: i.e. it is suitable for use in an ultracentrifuge. As noted above, symmetric and even rotor packing requires the use of swinging bucket ultracentrifuge rotors (UCR), such as the ones listed in Table 2.1. Thus, the design discussed here fits the 38.5 mL tubes of an SW 32 Ti UCR capable of achieving g-forces up to 175,000 x g on the tool itself. Greater g-forces can be achieved by the use of other UCR types, requiring the design of more compact tools that fit the smaller tube sizes (Table 2.1). Note that the placement of the MAS rotor within the device determines the g-forces that the sample itself will experience. For example, our packing tool can be spun at a maximum rate of 32,000 RPM corresponding to 175,000 x *g* forces felt by the device itself. However, the actual MAS rotor within our packing device experiences a maximum g-force of up to 162,000 x *g*. As discussed in more detail below, it is important to note that these g-forces are significantly less than the typical g-forces experienced by the sample while under MAS (Table 2.2).

Table 2.2. Characteristics of Bruker MAS rotors

Bruker MAS rotor	Max. MAS rate b)		G-force on sample	Sample volume a)
	(kHz)	(RPM)		(μl)
0.7mm	111	6,660,000	11,180,000	0.5
1.3mm	67	4,020,000	8,140,000	2.5 – 3
1.9mm	42	2,520,000	5,330,000	10 – 14
2.5mm (regular)	35	2,100,000	3,700,000	12 – 16
2.5mm (thinwall)	35	2,100,000	4,200,000	12 – 20
3.2mm (regular)	24	1,440,000	2,550,000	30 – 40
3.2mm (thinwall) b)	5	300,000	130,000	42 – 50
	8.3	500,000	360,000	
	12	720,000	750,000	
	24	1,440,000	3,020,000	
4mm	15	900,000	1,360,000	89 – 92

a) Sample volume estimates for all rotors (except 0.7mm) were obtained, and calculated from dimensions published by Cortecnet (Brooklyn, NY). Sample volume estimate for 0.7mm rotor was obtained from Bruker Biospin.

b) Additional lower MAS rates are reported for the 3.2mm MAS rotors.

We designed two devices that fit the SW 32 Ti UCR buckets: one for 3.2mm and one for 4mm OD Bruker MAS rotors. The former tool is shown in Figure 2.1 and Figure A.1 (in Section 1.01(a)(i)Appendix A), while the latter is shown only in Figure A.1. The design features three discrete pieces, each of which is machined from unfilled PEEK, in order to withstand the repeated and extensive exposure to high g forces. The bottom piece (part I in Figure 2.1) holds the 3.2 mm (or 4 mm) flat-bottomed Bruker rotors without the drive cap in place. Piece I is machined for a tight fit around the MAS rotor, in order to avoid excessive local stresses and forces during the packing process. The middle piece screws on to the bottom piece to seal the rotor in place, while also featuring a funnel designed to hold the initial sample suspension (Figure 2.1c-d). The funnel is designed to hold a sample up to ~1 mL. Importantly, an O-ring is placed around the rotor to seal the parts and avoid sample losses (Figure A.1) [69, 73]. A proper seal is assured by the usage of an O-ring slightly thicker (1.5 mm) than the vertical gap separating the parts I and II (Figure 2.1d). The outer dimensions of the assembled device are such that it fits inside a clear centrifuge tube (Figure 2.1a; middle), in case there is a concern of accidental spillage or leakage. In the current design, the only function of the top piece (part III in Figure 2.1b-c) is to prevent possible collapse of the thin-walled centrifuge tube. In principle, one can extend the height of part II to generate a bigger funnel, but this may interfere with inspection (or handling) of the pelleted sample after the sample packing process. The external centrifuge tube acts as a backup in case of spills, which might occur if there is a failure of the O-ring or the bottom parts are not assembled properly. This fail-safe has rarely been necessary over the lifetime (~7 years) of our devices.

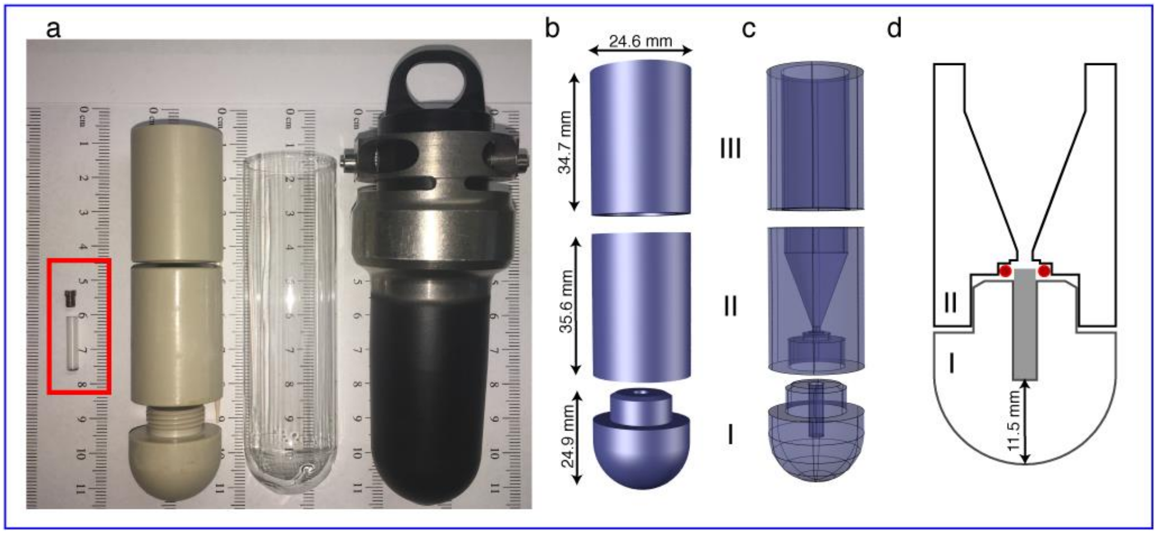

Figure 2.1. Schematics of the ultracentrifugal device for packing 3.2mm MAS rotors

(a) (L – R) Photo of 3.2mm Bruker MAS rotor with a cap (red rectangle), packing tool, an empty centrifuge tube and bucket holder for the SW 32 Ti UCR. (b) Exploded view of the packing tool with outer dimensions of the three components. This design drawing does not show the threading of part I (see panel a). (c) X-ray view showing the internal design. The bottom piece (I) holds the rotor, the middle piece (II) is the funnel in which the sample suspension is applied and the top piece (III) stabilizes the ultracentrifuge tube and packing device in the UCR bucket. Pieces I and II thread together for a tight seal (unsealed state shown in panel a). (d) Sliced-through view of parts I-II showing the relative dimensions and locations of the funnel, 3.2 mm Bruker rotor (grey rectangle), and O-ring (red). The parts are shown partly unscrewed for clarity.

2.3.3 Usage of ultracentrifuge packing tool

The protocol for packing MAS samples with these ultracentrifugal devices is illustrated in Figure 2.2. Since the sample will be centrifuged into the rotor, one end of the rotor is fully pre-assembled with any bottom spacers or bottom caps needed to seal it. For many Bruker-made rotors one end is closed anyway, so this may require no assembly. The empty rotor (lacking the drive cap) is inserting into the device’s bottom part (Figure 2.1d). The dimensions are such that the rotor sticks out slightly, such that it will insert into the O-ring (shown red in Figure 2.1d).

After verifying the positioning and presence of said O-ring, the funnel (part II in Figure 2.1b-d) is screwed on tightly by hand. This compresses the O-ring to seal the device against leakage. The device is now ready for administering the sample.

The sample of interest is prepared as a hydrated suspension or solution. Up to 1 mL of the aqueous sample is transferred into the funnel (Figure 2.2a-b), after which the filled device is encapsulated in the appropriate swinging-bucket tube holder (e.g. Figure 2.1a). To avoid drying out of the sample in the evacuated ultracentrifuge, it is critical that the bucket holder itself is carefully sealed. A secondary tube containing either dense solution or a second packing tool is then carefully weight-balanced, and used as a counter balance during centrifugation. During centrifugation (Figure 2.2c-d) the sample will be pelleted into an evenly distributed pellet at the bottom of the rotor. While the funnel can hold more than 1 mL, we typically limit the capacity to accommodate potential motion of the liquid sample during the centrifugation process (Figure 2.2c). When feasible, samples to be used for packing are designed to have a volume of no more than ~1 mL (i.e. roughly the size of a typical microcentrifuge tube), to facilitate a single-step packing process. Alternatively, one can pack a larger volume by repeating the ultracentrifuge step multiple times (see also below).

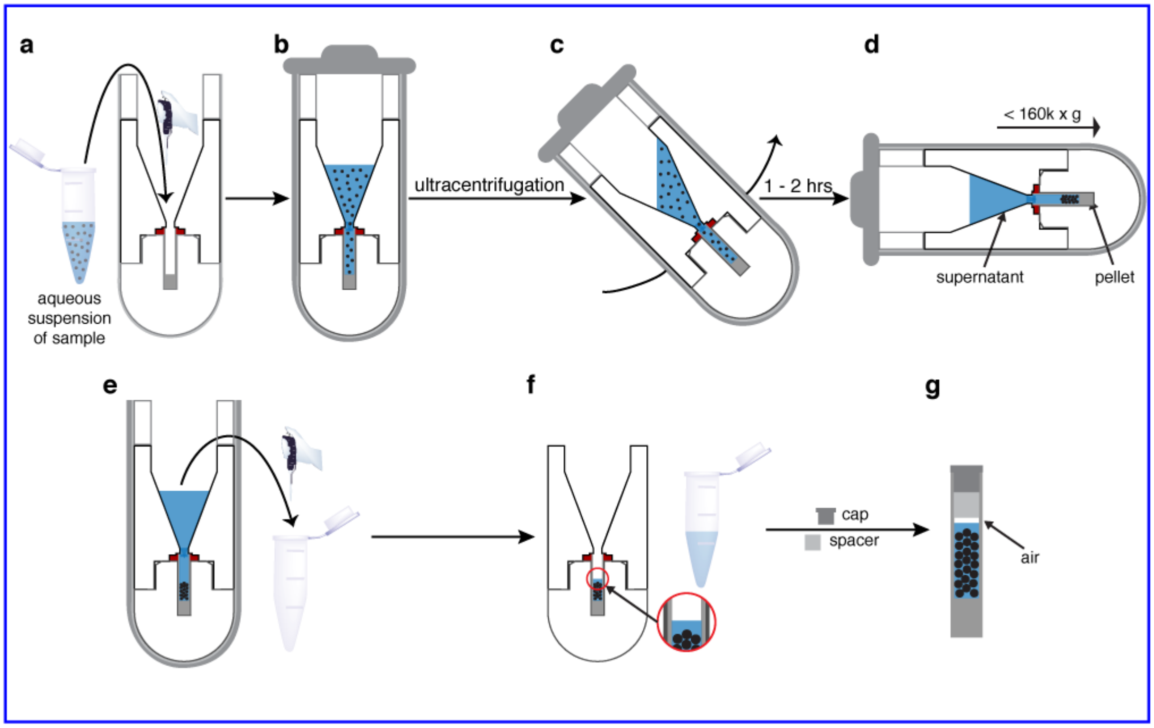

Figure 2.2. Overview of packing process using the ultracentrifuge packing tool

(a) The sample suspension is placed in the funnel, (b) up to a 1 mL volume. The packed tool is inserted in its swinging bucket and sealed. (c, d) During UC the bucket achieves a horizontal orientation that ensure even pelleting of the sample within the rotor. (e) After completion of the UC, excess supernatant is removed. (f) A small amount of supernatant is left to maintain excess hydration. (g) After disassembly of the packing tool the rotor is capped. Note that it is important to leave a small gap between the liquid and the spacer or cap (see text).

The desired end result of a the packing process is to have the “biosolid” forming an even pellet or sediment in the rotor, with a clear supernatant filling the funnel and top of the rotor (Figure 2.2e). The packing efficiency is evaluated by visual inspection and through the use of UV-Vis absorbance measurements on small samples taken from the supernatant. Next, the clear supernatant is carefully extracted from the funnel, such that an amount of supernatant remains atop the sample within the rotor (Figure 2.2f). The packing tool is then carefully disassembled, to avoid accidental spillage of the supernatant remaining in the rotor and to ensure that the pellet is not disturbed. Once the MAS rotor has been extricated, additional supernatant can be carefully removed using a pipette such that there is only a small layer of supernatant on top of the pellet. This supernatant ensures excess hydration, but should be small enough that a gap remains between it and the spacer (or drive cap) used to seal the rotor (Figure 2.2g). Performing this step after the disassembly of the tool allows for easier and careful judgment of the depths at which the pellet and supernatant lie in the rotor so as not to disturb the pellet. The supernatant removed in this final step can be added to the pool of supernatant that was removed in prior steps, which can then be analyzed by UV absorbance (or otherwise) to estimate how much protein was packed into the rotor. The gap above the sample is crucial for allowing thermal expansion, which can occur due to frictional heating during the MAS spinning and/or due to heating from RF pulses (in particular ^{1}H decoupling). A failure to leave room for sample expansion risks the drive cap being dislodged during NMR experiments, which would in turn cause rotor crashes.

2.3.4 Troubleshooting and optimization

Although the described procedures are suitable for a wide variety of samples (see below), the employed sample volume, centrifugation rate and centrifugation times may require some trial-and-error optimization. When packing a new kind of sample one may start at lower g-forces (~100,000 x g) for shorter periods of time (30 minutes to 1 hour), and evaluate the pelleting efficiency. The latter can be done by taking a small aliquot of the supernatant at the end of a run and submitting it to UV-Vis analysis. If there is sample still present in the supernatant, another round of UC either at higher speeds or for longer duration is performed as needed. If subsequent rounds of UC still fail to completely pack the entire sample, some troubleshooting is required. First, it is possible that the braking at the end of the runs is too severe and disturbs the pellet at the end of the run. Using low or no braking during UC can rectify this problem. Second, there may simply be more sample than can physically fit in the rotor. This may be fairly predictable for nanocrystalline proteins or peptides, but can be harder to predict for samples such as hydrated proteoliposomes. It is also possible that the sample needs to be subjected to higher g-force ultracentrifugation for extended durations.

2.3.5 Applications

Centrifugal packing tools have already been used by ourselves and others for preparing a wide variety of MAS NMR samples like protein micro- or nanocrystals [68], sedimented soluble proteins [69, 73], fibrillar aggregates [64, 66], and membrane-based samples [14, 59, 60]. As we discuss below, this approach is particularly beneficial for those samples were ultracentrifugation is critical to achieve efficient pelleting or sedimentation.

2.3.5.1 Case Study 1 – Membrane-associated proteins

We first examine the application of this approach to the ssNMR study of lipid vesicles, or vesicle-bound proteins, using our recent work as an example [14, 25]. Unilamellar lipid vesicles of varying sizes are frequently used to mimic biological membranes in studies of protein-lipid or peptide-lipid interactions [14, 78-82]. Unilamellar vesicles expose a maximum amount of membrane surface for binding by peripherally binding membrane proteins [14] or antimicrobial peptides [33]. Given their common use in vesicle leakage or vesicle fusion assays, ssNMR studies of LUV-based samples also allow a correlation to the results of such functional assays. As illustrated in Figure 2.3a, LUVs feature a single spherical lipid bilayer filled with aqueous solution, with diameters ranging from 100 nm to ~500 nm [83, 84]. For most common applicable sizes, the water-filled LUVs have densities in the range of 1.02 – 1.08 g/mL (Figure 2.3b) compared to protein aggregates or protein crystals with densities ~1.3 g/mL or higher [74, 75]. Note that, as indicated in Figure 2.3a, the lipid bilayer itself has a notably higher density, but only makes up a very small fraction of the entire LUV [64]. The low LUV density means that they are not easy to pellet unless one employs ultracentrifugation [85]. This is different for multilamellar vesicles (MLVs), which are more readily pelleted, as they can be 10-100x heavier than typical LUVs (Figure 2.3). LUVs, and in particular, LUVs sized less than 200 nm, increasingly require high g-forces that can only be achieved by ultracentrifugation. This has led prior studies to increase their effective density by the inclusion of halogenated [86] or biotinylated lipids [85]. Others achieve a similar effect by loading them with sucrose [87, 88]. However, this is not always practical, for instance if the vesicles are made porous by the addition of pre-amyloid oligomers or membrane-active peptides.

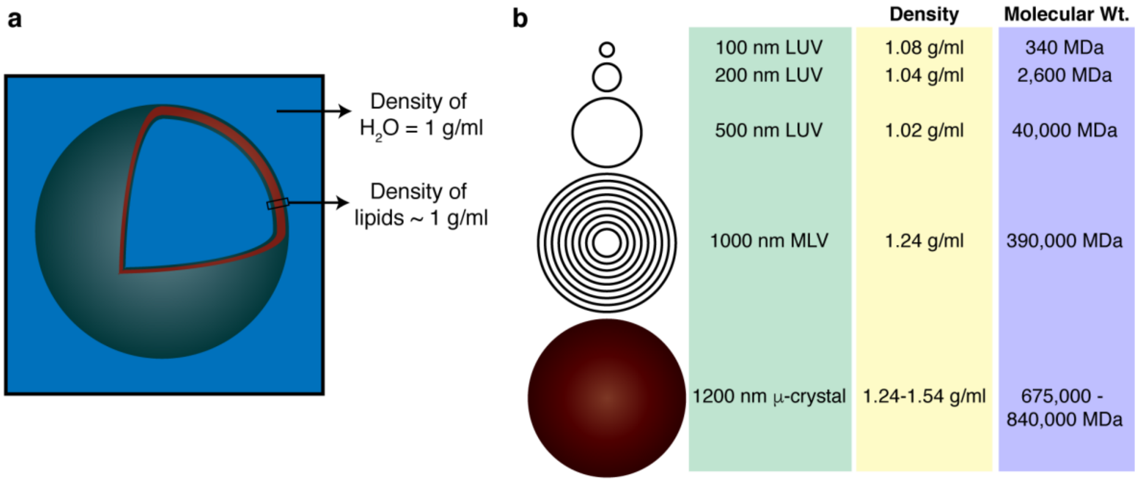

Figure 2.3. Dimensions and densities of lipid vesicles

(a) Schematic LUV shown approximately to scale. The (local) density of the lipid bilayer is higher than that of the water phase, but the overall density of the whole LUV is quite similar to that of water. (b) Typical size, density and molecular weight of differently sized LUVs, MLVs and protein μ-crystals.

The use of ultracentrifugal sample packing was especially advantageous in our recent studies of the peripheral membrane protein cytochrome c (Figure 2.4a-b) [14]. For both functional assays and for MAS ssNMR, the protein was bound to the membrane surface of 200-nm-sized LUVs. To achieve sample pelleting for ssNMR, the packing device containing the protein/LUV mixture was initially spun at 143,000 x *g* for 3 hours. Since UV measurements on the supernatant indicated that there was still LUV-bound protein left in the supernatant, a second UC step was performed at 175,000 x *g* for 4.5 hours. The final UV measurements confirmed that the 1.7 mg of (labeled) membrane-bound cytochrome c had completely pelleted in the rotor. A second, smaller sample featuring 0.75mg of protein was fully packed after 143,000 x *g* for 5 hours. The resultant samples were studies by 1D, 2D and 3D MAS ssNMR, with an example spectrum shown in Figure 2.4b [14]. As described elsewhere, these NMR studies provided new insights into the membrane-induced structural changes in cytochrome c, as well as the dynamics and phase behavior of the lipids themselves [14, 64].

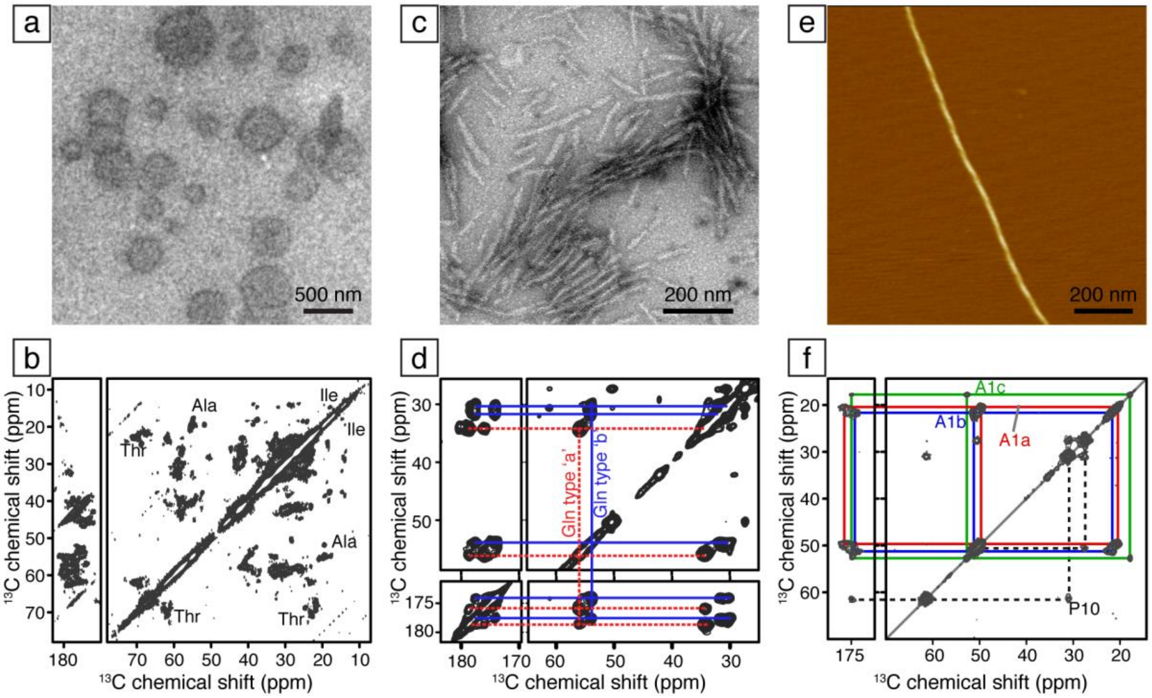

Figure 2.4. Examples of samples packed with ultracentrifugal devices

(a) TEM of TOCL/DOPC/cholesterol (0.15:0.75:0.10 molar ratio) vesicles with bound cytochrome c. (b) ^{13}*C-*^{13}*C CP DARR spectrum of 1.7 mg of U-*^{13}*C,*^{15}*N cytochrome c bound to TOCL/DOPC (1:4 molar ratio) vesicles. (Adapted from [14], Copyright 2015, with permission from Elsevier.) (c) TEM on [U-*^{13}*C-*^{15}*N]-labeled huntingtin exon 1 fibrils prepared for ssNMR. (d)* ^{13}*C-*^{13}*C CP DARR spectrum of 4.4 mg of htt exon1 fibrils. Panels (c-d) are adapted from [64]. (e) AFM on* C_{18}*-(*$PEP_{Au}^{M\text{-}ox}$*)*$_2$ *fibers. (f)* ^{13}*C-*^{13}*C CP DARR spectrum of 1.9 mg of* C_{18}*-(*$PEP_{Au}^{M\text{-}ox}$*)*$_2$ *peptide nanofibrils. Panels (e-f) are adapted with permission from [67]. Copyright 2016 American Chemical Society.*

2.3.5.2 Case Study 2 – Fibrillar samples

Another application of the packing tool is in the study of fibrillar protein and peptide aggregates, whether in a biological context or for materials-science applications. These can present a challenge for packing due to their elongated and sometimes quite rigid fibrillar structure, which turns the samples into hydrogels. Such hydrogels can resist compaction unless they are subjected to high g-forces. Depending on the sample, pre-treatments involving sonication or ultracentrifugation may be beneficial prior to the actual packing process.

We have successfully used the ultracentrifuge-packing tool to prepare a variety of fibrils [62-64, 66]. Our most recent studies on huntingtin exon1 (Figure 2.4c-d) [64, 66] involved the packing of htt exon1 fibrils into 3.2 mm MAS rotors. The packing protocol used here was slightly modified, based on the fact that here the sample size was limited by the amount of available protein fibrils rather than the size of the MAS rotor. After the first round of centrifugation at 154,000 x *g* for one hour, the supernatant was removed. At that time, 1 mL of buffer was used to rinse the original sample tube in order to recover residual sample that may have been left behind. This second batch was then added to the funnel and submitted to another round of centrifugation. A second rinse and centrifugation cycle was performed before the rotor was sealed for study by MAS NMR. At each stage, the supernatant collected was checked by UV-Vis absorbance spectrometry to determine the final amount of sample packed in the rotor. Figure 2.4d shows an example spectrum obtained on such a sample, with more data shown in our published work on huntingtin exon 1 fibrils and other polyQ aggregates [62, 64, 66].

2.3.5.3 Case Study 3 – Nanocrystals and other nanoassemblies

Some samples, especially protein nano-crystals and non-fibrillar aggregates do not necessarily require ultracentrifugation for efficient pelleting. Nonetheless, we find the described approach equally useful for these samples as it renders the process convenient, fast and reproducible. Thus, we have similarly used this approach for peptide-based or protein-based nanocrystals [89, 90]. Figure 2.4e-f illustrates a more recent application to acylated divalent peptide-derived nanoparticles (C_{18}-$(PEP_{Au}^{M\text{-}ox})_2$ where PEP denotes the sequence AYSSGAPPMPPF) that are designed to induce formation of chiroptical gold particle assemblies (Figure 2.4e-f) [67]. The packing protocol used here was very simple. After applying the nanoparticle suspension to the packing tool, it was subjected to ultracentrifugation for 1 hour at 175,000 x *g* at 4 °C. UV measurements on the supernatant collected at the end of the centrifugation run confirmed that 1.92 mg of particles were packed into the rotor. Various MAS NMR spectra (e.g. Figure 2.4f) were then used to probe the structural and motional features of the nanoparticle assemblies.

2.4 DISCUSSION

2.4.1 Potential concerns and caveats

We have delineated how ultracentrifugal packing tools facilitate a generally applicable, convenient and effective way to pack hydrated samples for MAS ssNMR. The resulting samples retain their fully hydrated state, which is valuable to assure biological relevance, but also can be beneficial for spectral quality [49-52, 60]. At the same time, one can minimize excess buffer, which not only maximizes the ssNMR signal but also may improve the RF distribution in the sample [68]. In this section, we want to discuss and address a number of potential concerns with this approach.

Perhaps most importantly, one may express concern about the consequences of submitting potentially sensitive (biological) samples to ultracentrifugation during the packing process. The g-forces associated with the advocated sample packing approach can exceed 100,000 *x g* (Table 2.1), which may indeed lead to irrevocable changes in certain samples [91-93]. Whilst this is not an unreasonable concern, it is important to realize that this may be a moot point when samples are used for MAS ssNMR. Table 2.2 lists maximum (and typical) spin rates for different types of MAS rotors along with the corresponding g-forces that will be exerted on the sample. Comparing Table 2.1 and Table 2.2, it is clear that that most MAS experiments are done at conditions that result in larger g-forces on the sample than exerted by an ultracentrifugal packing device. Thus, it seems unnecessary to avoid ultracentrifugal packing due to concerns of sample damage.

Another concern affecting the design and use of these devices is whether the g-forces involved would (over time) cause damage and deformations in either the packing device or the MAS rotors. The two ultracentrifugal packing devices described in this paper were purposely designed to be simple, solid and robust. Since their construction in January 2010, they have been subjected to hundreds of hours of centrifugation. A few cosmetic scratches notwithstanding the tools continue to function as designed without leakage. Given that the g-forces associated with MAS exceed those of the packing process, one may think that there is no need to worry about rotor damage. However, the direction of the forces during packing will be along the length of the rotor. Depending on the design and execution of the packing device, one may also end up with particularly high forces being applied to specific points on the rotor. However, after almost seven years of usage, we have not observed any evidence or indication of negative consequences for the MAS rotors.

The described designs are based on Bruker design MAS rotors, and in particular their 3.2 and 4 mm rotors. Devices suitable for packing other rotor sizes or rotor designs will require design changes. For instance, some rotors have two open ends. Although one could insert an end-cap before packing the sample, it is likely that these caps may not withstand the forces involved in the packing process. Thus, one may need to replace the end cap after sample packing, or adapt the design of the packing device. For other rotor sizes, and in particular the advent of increasingly small rotors, it is likely that design changes will be needed beyond a mere "scaling down" of the described devices. That said, it may also be that this kind of approach is actually particularly beneficial for the tinier rotor sizes (more on this below).

Finally, although we focused on the study of hydrated samples, there are certainly scenarios where packing tools are not needed for the ssNMR study of entirely dry samples. For instance when investigating transient or unstable intermediates [94, 95], one may trap and stabilize these states by freezing and lyophilizing the samples. In addition, it is also true that complete dehydration, followed by controlled re-hydration, is likely to remain the best way of retaining complete control of the sample hydration. This is particularly true when low levels of sample hydration as necessary or desired [96, 97].

2.4.2 Alternative designs and commercial availability

As noted above, similar devices have been used in a variety of ssNMR labs and have been described in the literature. Typically these have been custom-built devices that each feature different design choices and priorities. One of the differences in the various designs in the literature so far is the materials used for construction of the packing tool components. It is important to use a material that can be milled to high precision, is strong, durable and protective of the rotor during centrifugation. In our case these considerations and the expertise and tools available to us dictated our choice to use unfilled PEEK to construct all components of our packing tool. Other packing tools have been constructed usually using different materials like polyoxymethylene (POM), PEEK with 30% glass, delrin®, vespel®, aluminum and epoxide glass for the various components [68, 73, 77]. There are examples of centrifugal tools designed for packing samples for ultrafast MAS NMR in the literature, for instance those used for packing amyloid fibril samples into 1.3 mm sized rotors [64]. Some of these devices are also commercially available. For instance, we have successfully used a device from Giotto Biotech (Sesto Fiorentino, Italy) to prepare 1.3 mm sample rotors. Finally, there are scenarios where one may need to reach higher g-forces than possible in the devices described here. This includes samples containing small LUVs and SUVs, or sedimentation NMR applied to smaller proteins. Such cases require packing tools designed for used in a swinging-bucket UCR that achieves even higher g-forces (Table 2.1). For instance, a prior report described an ultracentrifugal packing device for use with a SW 60 Ti UCR allowing a maximum g-force up to 485,000 x *g* [69]. Given that this still stays well below the g-forces associated with commonly used MAS NMR rates (Table 2.2), it seems likely that this may be the optimal approach going forward, assuming that these centrifugal forces are found to not affect the structural integrity of the MAS rotors themselves.

2.5 CONCLUSION

In this report we discuss and advocate the more general use of ultracentrifugal packing devices for routine preparation of samples for modern MAS NMR. This approach maintains hydration throughout the packing process while at the same time making the entire process simpler and faster than more manual sample transfer methods. As discussed, these devices have a proven track record in applications to a wide array of sample types, but still are underused in the ssNMR community. We expect that a wider adoption of this methodology will help make ssNMR sample preparation faster, more routine, and more reproducible.

2.6 ACKNOWLEDGEMENTS

We thank Mike Delk for technical assistance. Funding support was from the University of Pittsburgh and the National Institutes of Health grants R01GM112678 and R01GM113908 (P.v.d.W.).

3.0 STRUCTURAL CHANGES AND PRO-APOPTOTIC PEROXIDASE ACTIVITY OF CARDIOLIPIN-BOUND MITOCHONDRIAL CYTOCHROME C

Adapted with permission from: **Mandal, A.**, Hoop, C.L., DeLucia, M., Kodali, R., Kagan, V.E., Ahn, J., and van der Wel, P.C.A. Structural changes and pro-apoptotic peroxidase activity of cardiolipin-bound mitochondrial cytochrome c, *Biophysical Journal 109(9),* 1873-1884. Copyright 2015 with permission from Elsevier.

Author contributions: A.M. and M.D. performed protein expression and purification; A.M., C.L.H., and R.K. made samples and performed spectroscopic (non-NMR) measurements; A.M., C.L.H., and P.v.d.W. performed ssNMR experiments; A.M. and P.v.d.W. analyzed data; A.M., V.E.K., J.A., and P.v.d.W. designed research; A.M. and P.v.d.W. wrote the paper.

The cellular process of intrinsic apoptosis relies on the peroxidation of mitochondrial lipids as a critical molecular signal. Lipid peroxidation is connected to increases in mitochondrial reactive oxygen species (ROS), but there is also a required role for mitochondrial cytochrome c (cyt-c). In apoptotic mitochondria, cyt-c gains a new function as a lipid peroxidase that catalyzes the ROS-mediated chemical modification of the mitochondrial lipid cardiolipin (CL). This peroxidase activity is caused by a conformational change in the protein, resulting from interactions between cyt-c and CL. The nature of the conformational change and how it causes this gain-of-function remain uncertain. Via a combination of functional, structural and biophysical experiments we investigate the structure and peroxidase activity of cyt-c in its membrane-bound state. We reconstituted cyt-c with CL-containing lipid vesicles, and determined the increase in peroxidase activity resulting from membrane binding. We combined these assays of CL-induced pro-apoptotic activity with structural and dynamic studies of the membrane-bound protein via solid-state NMR (ssNMR) and optical spectroscopy. Multidimensional magic-angle-spinning (MAS) ssNMR of uniformly ^{13}C,^{15}N-labeled protein was used to detect site-specific conformational changes in oxidized and reduced horse heart cyt-c bound to CL-containing lipid bilayers. MAS NMR and FTIR measurements show that the peripherally membrane-bound cyt-c experiences significant dynamics, but also retains most or all of its secondary structure. Moreover, in 2D and 3D MAS NMR spectra the CL-bound cyt-c displays a spectral resolution, and thus structural homogeneity, that is inconsistent with extensive membrane-induced unfolding. Cyt-c is found to interact primarily with the membrane interface, without significantly disrupting the lipid bilayer. Thus, membrane binding results in cyt-c gaining the increased peroxidase activity that represents its pivotal pro-apoptotic function, but we do not observe evidence for large-scale unfolding or penetration into the membrane core.

3.1 INTRODUCTION

Intrinsic apoptosis, one of the pathways for programmed cell death, is initiated by signaling events in mitochondria [7, 98]. The mitochondrial apoptotic pathway is implicated in various diseases and represents an important target for drug design. In neurodegenerative diseases, including Huntington’s Disease, mitochondrial apoptosis leads to neuronal degradation and mitochondrially targeted antioxidant drugs have been shown to be protective [4, 99]. Conversely, the triggering of apoptosis is considered a potential anti-cancer treatment [7]. As a result, there is a need to understand the underlying mitochondrial signaling events. Early stages of the cell death process require functionally important changes in mitochondrial proteins, lipids, and membranes, with a particularly central role for the mitochondrial lipid cardiolipin (CL). This unique lipid is normally found in the matrix-facing inner leaflet of the inner mitochondrial membrane (IMM) [12, 100]. As a precursor to apoptosis, this tightly controlled distribution is disrupted and CL becomes increasingly exposed to the inter-membrane space (IMS) and the outer mitochondrial membrane (OMM) [1, 8, 101-103]. CL is then recognized, in both locations, by different proteins that trigger lipid peroxidation, permeabilization of the OMM, and release of pro-apoptotic factors [104, 105]. Crucially, the arrival of CL in the OMM and the peroxidation of CL polyunsaturated fatty acid (PUFA) chains are pivotal mitochondrial signals that trigger apoptosis or mitophagy [8, 15, 87]. The pro-apoptotic peroxidation reaction is mediated by mitochondrial reactive oxygen species (ROS), but also requires the involvement of mitochondrial cytochrome c (cyt-c) [8, 106]. As the normal asymmetric distribution of CL in the IMM is disrupted, there is an increase in the normally very low IMS-facing CL concentration. As this occurs, cyt-c becomes able to interact in new ways with the IMM, most likely through an interaction with multiple CL lipids. A CL-cyt-c complex is then formed, which turns cyt-c into a potent lipid peroxidase with high selectivity for CL over other lipids [13, 107, 108]. Despite substantial interest and effort, it has proved challenging to gain insight into the CL-induced structural changes in cyt-c and how they trigger the lipid peroxidase activity. Of particular biological importance are the initial interactions of cyt-c with CL-containing membrane domains under conditions where the accessibility of CL and ROS (H_2O_2) represents a rate-limiting “bottle-neck” that triggers the entire process.

Mechanistically, oxidation of the lipid acyl chains requires access of the PUFA to the catalytic reactive intermediates of cyt-c. These intermediates involve the protein's covalently attached heme as well as protein-associated radicals, recently localized to Tyr67 [15]. These sites are buried in cyt-c's native fold, which is visualized in Figure 3.1a. Some studies have suggested that accessibility of the catalytic site upon CL binding results from cyt-c acquiring a largely unfolded or molten-globule-like state within the membrane [109-114]. In contrast, the "extended lipid anchorage" model [115-118] proposes that cyt-c stays on the bilayer surface, but extracts one or two CL acyl chains from the membrane. Hydrophobic interactions between the extracted acyl chains and a hydrophobic cleft on the protein surface then facilitate the necessary proximity to cyt-c's catalytic site. Solution NMR and X-ray crystallographic studies have yielded high-resolution structures of cyt-c mutants with enhanced peroxidase activity due to a local structural change, without a loss of native tertiary fold [119, 120]. However, these structures were obtained in absence of lipid bilayers, and the relevance of the data to the peroxidase activity gains induced by CL-binding remains unclear.

Experimental characterization of membrane-bound cyt-c has proved challenging. Applicable techniques tend to yield relatively low-resolution structural insights and often also require the introduction of potentially disruptive fluorescent or spin labels. Solid-state NMR (ssNMR) spectroscopy permits the site-specific determination of structure and dynamics in proteins associated with lipid bilayers [65, 121-124]. Labeling for ssNMR involves non-disruptive stable isotopes, which can be uniformly applied since site-specific information is accessible via multidimensional spectra [123, 125]. Here we apply multidimensional MAS ssNMR to uniformly U-^{13}C,^{15}N-labeled cyt-c in its membrane-bound and peroxidase-active form. Prior ssNMR studies have provided important insights into the effect of bound, unlabeled cyt-c on the membrane, revealing for instance a propensity to disrupt the lipid bilayer structure [21, 109, 110, 121, 126-130]. Previously, ssNMR on cyt-c itself was limited due to challenges with the isotopic labeling, with prior reports relying on methionine $^{13}C^{\varepsilon}$ labeling or ^{2}H back exchange [109, 127]. These studies revealed dynamics and disorder in the membrane-bound protein. Using peroxidase assays, Fourier-transform infrared (FTIR) spectroscopy and advanced MAS NMR we probe the CL-induced peroxidase activation, and the structural features of both the membrane and the membrane-bound protein. Cyt-c is found to bind tightly to the CL-containing unilamellar vesicles, which causes the expected increase in peroxidase function. Static and MAS NMR spectra show no evidence of lipid bilayer disruption and indicate that the protein is present at the membrane interface. The membrane-bound cyt-c experiences substantial dynamics, but in room temperature FTIR studies as well as low-temperature 2D and 3D MAS ssNMR experiments we find that the secondary structure and much of the tertiary fold are retained.

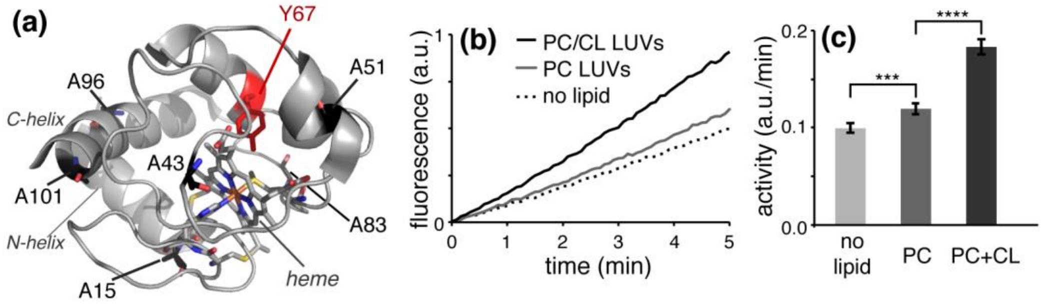

Figure 3.1. Cytochrome c structure and peroxidase activity

(a) X-ray structure of oxidized cyt-c [16]. Labels mark the catalytic sites of peroxidase-active protein (heme and Tyr67). Cyt-c's six alanines are also indicated. (b) Generation of the fluorescent oxidation product resorufin by 0.5 μM cyt-c. Measurements were performed at room temperature in absence (dashed) and presence of DOPC LUVs (grey solid line) or DOPC/TOCL (4:1) LUVs (black solid line). (c) Relative peroxidation rates obtained from linear fits to the data in (b).

3.2 METHODOLOGY

3.2.1 Expression and purification of $^{13}C,^{15}N$-cytochrome c

Uniform $^{13}C,^{15}N$-labeling of horse heart cyt-c was performed by overexpression in Escherichia coli. In line with previous reports, an expression-optimized mutant (H26N; H33N) was employed that eliminates kinetic folding traps, but is structurally similar to the wild-type protein [15, 131, 132]. A pETDuet plasmid (EMD Millipore, Billerica, MA) was used to co-express cyt-c and the heme lyase required for covalent attachment of the heme [131, 133]. The respective cDNAs were cloned in the NcoI/EcoRI and NdeI/XhoI sites of the vector. For U-$^{13}C,^{15}N$ isotopic labeling, the protein was expressed in minimal media with 0.1% (w/v) $^{15}NH_4Cl$ and 0.4% (w/v) ^{13}C-labeled D-glucose, as well as 0.5 mM $FeCl_3$ and 580 µM of unlabeled 5-aminolevulinic acid hydrochloride. At an optical density (OD) of ~1.1, overexpression was induced by addition of IPTG, along with supplementary $^{15}NH_4Cl$ and ^{13}C-D-glucose (0.1 and 0.2 g/L, respectively). After ~16 h at 18 °C, cells were recovered by centrifugation, resuspended in 25 mM sodium phosphate buffer (pH 6.5) with 0.02% sodium azide, and lysed. Cell debris was removed centrifugally, yielding a pink-colored supernatant. Purification of the labeled protein utilized a cation exchange HiTrap SP HP column, using a 25 mM sodium phosphate running buffer (pH 6.5) with 10% (v/v) glycerol and 0.02% sodium azide, and a 0-1 M NaCl salt gradient. The eluate was further purified on a gel filtration Superdex 75 26/60 column, using 25 mM sodium phosphate buffer at pH 6.5, with 150 mM NaCl, 5% glycerol and 0.02% sodium azide. Fully oxidized protein was obtained by treatment with a 5-fold molar excess of potassium hexacyanoferrate (III), which was removed by extensive dialysis. Buffer exchanges to the experimental buffer (freshly degassed 20 mM HEPES buffer at pH 7.4) were performed via dialysis or use of 10kDa Amicon Ultra-15 centrifugal filters. Typically, the yield of U-^{13}C,^{15}N-labeled cyt-c was 2.4 mg/L of cell culture.

3.2.2 Preparation of samples for solid-state NMR

Di-oleoylphosphatidylcholine (DOPC) and tetra-oleoylcardiolipin (TOCL) were obtained from Avanti Polar Lipids (Alabaster, Alabama, USA). The lipids (in chloroform) were mixed in a 4:1 molar ratio, after which the solvent was removed under N_2 flow and by drying under vacuum overnight. Next, 1 ml of freshly degassed 20 mM HEPES buffer (pH 7.4) was added, followed by gentle vortexing for 20-30 mins. After freeze-thawing of the lipid mixture 10 times, eleven extrusion steps were performed using a mini-extruder (Avanti Polar Lipids) outfitted with 100 or 200 nm polycarbonate membranes, to yield large unilamellar vesicles (LUVs). Vesicle sizes were evaluated using dynamic light scattering (DLS), performed at room temperature on a DynaPro Plate Reader (Wyatt Technology, Santa Barbara, CA). The DLS data were analyzed using Wyatt's DYNAMICS software (version 7) and plotted with Prism 6 (GraphPad, La Jolla, CA) and Microsoft Excel. When applicable, stock solution of cyt-c (in 20 mM HEPES pH 7.4) was added to a 1:40 protein/lipid molar ratio (P/L ratio), followed by gentle vortexing and incubation at 4°C. For MAS ssNMR, an ultracentrifugal sample packing device was used to pellet the LUVs or protein-lipid complexes into 3.2- and 4-mm MAS rotors. Centrifugation was either 3 hrs at ~143,000 x g and 4.5 hrs at ~175,000 x g, or ~143,000 x g for 5 hrs, in a Beckman Coulter Optima L-100 XP ultracentrifuge with a SW-32 Ti rotor. The packing devices were designed and built in-house, and resemble 'sedimentation' devices [73]. The supernatant was removed and UV-VIS measurements on the supernatant were used to determine the amount of cyt-c bound to the pelleted, red-colored LUVs. MAS rotors were from Bruker Biospin (Billerica, MA, USA) and CortecNet (Mill Valley, CA).

3.2.3 Solid-state NMR spectroscopy

All ssNMR spectra were acquired on a wide-bore 600 MHz (14.1 T) spectrometer (Bruker Biospin, Billerica, MA), using 3.2 mm MAS probes with a HCN “EFree” coil or HFCN-tuned solenoid coil, unless otherwise noted. 1D ^{13}C spectra were obtained at 8.333 kHz MAS, using either ramped ^{1}H-^{13}C cross-polarization (CP) (1 ms contact time) [28], the rotor-synchronized refocused insensitive nuclei enhanced by polarization transfer (INEPT) scheme with $\tau_1 = 1.44$ ms and $\tau_2 = 0.72$ ms [30], or a 50 kHz 90° ^{13}C excitation pulse. During acquisition, two pulse phase modulation (TPPM) ^{1}H decoupling was applied [29]. 2D ^{13}C-^{13}C spectra were obtained using dipolar assisted rotational resonance (DARR) ^{13}C-^{13}C mixing [134], and a 3D ^{15}N-^{13}C NCACX spectrum was recorded using a standard NCA(CX) pulse sequence. Additional experimental details for the various ssNMR experiments are listed in Table B.1 in Section 1.01(a)(i)Appendix B. Static ^{31}P NMR was performed with a Bruker ^{31}P/^{1}H ssNMR probe outfitted with a horizontal “EFree” reduced electric field coil, using high-power ^{1}H decoupling. The sample temperature was regulated at the indicated temperatures with cold cooling gas. The temperatures indicated throughout this article reflect internal sample temperatures that were calibrated using both external reference samples and internal referencing, following previously described protocols [68, 135, 136]. Spectra were processed using Bruker Topspin and NMRPipe software [137]. Except where specified otherwise (Figure 3.2, Figure 3.4), processing involved apodization with a cosine-bell function, and zero-filling of the direct and indirect dimensions with once or twice the original data size, phase correction and Fourier transformation. Spectral analysis, plotting and assignments were done using the CcpNmr Analysis program developed by the Collaborative Computation Project for the NMR community (CCPN) [138, 139]. ^{31}P NMR spectra were analyzed using the lineshape fitting routines of Topspin. The resulting CSA parameters are reported as CSA span values (Ω, as defined in ref. [140]), which are here equivalent to the shielding anisotropy $\Delta\delta$. Lipid peaks were assigned based on reference samples and previous reports [65, 129, 141]. ^{31}P isotropic chemical shifts were referenced to phosphoric acid based on MAS NMR on hydroxylapatite (from Acros Chemicals, Geel, Belgium) [142]. ^{1}H, ^{13}C, and ^{15}N chemical shifts were referenced to dilute aqueous DSS and liquid ammonia, via external indirect referencing of adamantane ^{13}C chemical shifts [140, 143]. Synthetic spectra were generated using utilities from the NMRPipe toolkit, and chemical shifts were predicted from a published crystal structure [16] using the SPARTA+ program [144].

3.2.4 Optical spectroscopy

Quantitative analysis of the cyt-c oxidation state was performed based on the UV-VIS absorbance profiles for reduced and oxidized protein, measured at room temperature [145]. The absorbance at 434 nm was employed to determine the protein concentration. Corrections were applied for baseline shifts due to any turbidity in lipid-containing samples, where needed. FTIR spectroscopy was performed at room temperature for both soluble cyt-c and for cyt-c bound to 1:4 (molar) TOCL/DOPC, using an MB series spectrophotometer (ABB Bomem, Quebec City, QC). The buffer signal was subtracted from each of the FTIR spectra using PROTA software (Biotools Inc., Jupiter, FL). Peak deconvolution was then applied to the amide I region after using the Savitzky-Golay algorithm to apply a 2.9% smoothing and baseline correction. Second derivative analysis was used to determine peak positions, and peak fitting was performed using Gaussian lineshapes in the PeakFit v4.12 program (Systat Software Inc., San Jose, California).

3.2.5 Activity measurements

Peroxidase activity measurements were performed based on previous reports [15, 87]. Fluorescence measurements were performed at room temperature, using a Horiba Scientific Fluoromax-4 spectrofluorometer (Edison, NJ). Samples were prepared analogous to the NMR samples. LUVs were prepared by extrusion in 20 mM HEPES pH 7.4 buffer, which here included 100 μM of the chelating agent diethylene triamine pentaacetic acid (DTPA). Stock solution of unlabeled cyt-c was added, followed by the substrate amplex red (AR) (ThermoFisher Scientific, Waltham, MA), to a 50 μM final AR concentration and a final protein to AR ratio of 1/100. A 5-min baseline was measured, after which H_2O_2 was added at 50 μM final concentration. Peroxidase activity was monitored based on the time-dependent increase in fluorescence from the oxidation product resorufin [146]. Relative activity rates were determined by linear fitting.

3.3 RESULTS

3.3.1 Peroxidase activity of LUV-bound ^{13}C,^{15}N-labeled cyt-c

Unilamellar vesicles were prepared from a mixture of TOCL and DOPC, in order to assure optimal access of the protein to the lipids. DLS measurements showed that the obtained vesicles were homogeneous in terms of their diameter (Figure B.2 in Section 1.01(a)(i)Appendix B). The desired amount of protein stock solution was added to the LUVs at room temperature, resulting in CL-dependent binding. Membrane-binding was observed by pelleting the cyt-c/LUV samples by centrifugation, followed by UV-VIS measurements of the supernatant to measure residual unbound cyt-c, and further confirmed by monitoring the color of the pelleted LUVs. In the activity assays and all other experiments, the same variant of horse heart cyt-c was expressed in-house as described in the methods, and added to the vesicles at a 1:40 protein-to-lipid (P/L) molar ratio. This ratio is designed to mimic conditions during the early stages of the pro-apoptotic process. As discussed in the introduction, the CL asymmetry across the IMM becomes disrupted, which allows for the formation of CL-rich domains in the IMS-facing leaflet of the IMM. Our *in vitro* experiments are designed to probe the cyt-c peroxidase activity and molecular features of protein and lipid bilayer under these kinds of conditions. We measured the peroxidase activity of the LUV-bound cyt-c in fluorescence-based assays, performed at room temperature in presence and absence of LUVs. Figure 3.1b shows the time-dependent generation of fluorescent product, and Figure 3.1c the corresponding activity rates for the different samples. Binding to CL-containing LUVs causes a significant increase in peroxidase activity, relative to the nascent activity of the protein, in line with previous reports [15, 87].

3.3.2 Lipid-bilayer-bound cyt-c experiences significant dynamics

Using the same protocols, uniformly ^{13}C and ^{15}N-labeled (U-^{13}C,^{15}N) cyt-c was bound to 4:1 (molar) DOPC/TOCL LUVs, and the membrane-bound cyt-c was pelleted into ceramic MAS sample holders using home-built ultracentrifugal sample packing tools. This packing method ensured the fast, straightforward and highly reproducible preparation of LUV-based MAS NMR samples without risk of sample dehydration during transfer of membrane pellets. Analysis of the supernatant by UV-VIS showed that typically ~75% of the U-^{13}C,^{15}N cyt-c was pelleted, in LUV-bound form, into the MAS rotor.

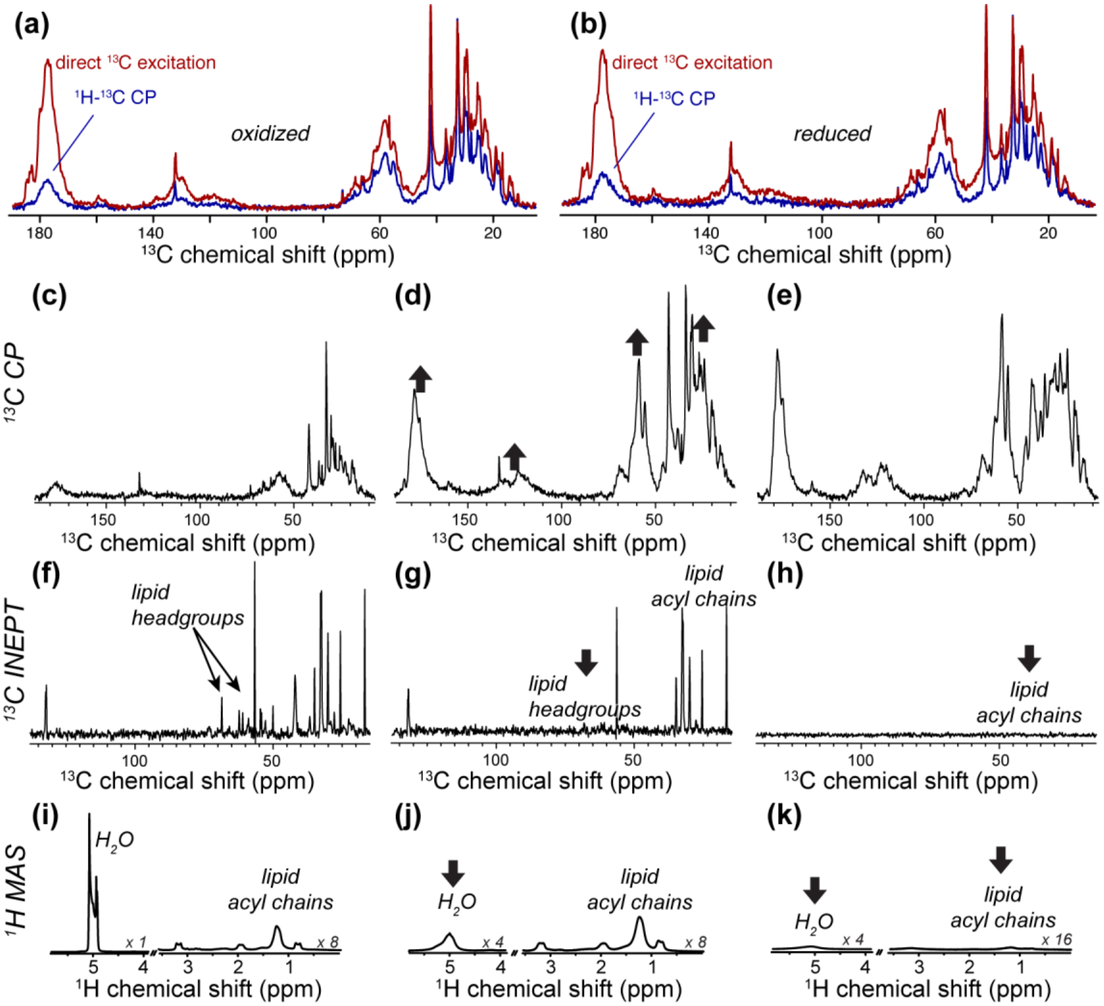

Figure 3.2. 1D MAS NMR spectra of oxidized and reduced U-^{13}C,^{15}N cyt-c bound to TOCL/DOPC LUVs

(a,b) ^{1}H-^{13}C CP and direct excitation ^{13}C spectra of oxidized and reduced membrane-bound cyt-c, at 271 K. The spectra in each panel are plotted with absolute intensities, and were processed with 25 Hz exponential line broadening and four-fold zero-filling. (c) ^{1}H-^{13}C CP spectrum at 257 K, showing mostly lipid signals. (d) CP spectrum at 250 K, and (e) 236 K, with much increased protein signals (up arrows). (f) 1D ^{1}H-^{13}C refocused INEPT spectrum at 257 K, with mostly lipid peaks (head groups marked). (g,h) INEPT data at 250 K and 236 K, showing loss of lipid headgroup and acyl chain signals, respectively (down arrows). (i) 1D ^{1}H spectrum at 257 K, with intense liquid water peak. (j) 1D ^{1}H spectrum at 250 K, after freezing of solvent (down arrow). (k) ^{1}H 1D at 236 K, showing a loss of acyl chain signals (down arrow). Data obtained at 600 MHz (^{1}H) and 8.33 kHz MAS, and processed with a cosine-bell apodization function and zero-filling to twice the original size. Selected spectra are scaled as indicated.

Figure 3.2a shows 1D ^{13}C MAS NMR spectra acquired on such a sample featuring oxidized U-^{13}C,^{15}N-labeled cyt-c, using either direct ^{13}C excitation (red) or ^{1}H-^{13}C CP (blue). The CP spectrum shows fewer peaks and much lower intensity peaks compared to the direct excitation data. The strongest ^{13}C signals in the CP spectrum are lipid signals rather than those of the labeled protein. Similar results were obtained with the reduced form of the protein (Figure 3.2b), providing no direct evidence of excessive paramagnetic broadening or relaxation due to the heme. The spectra in Figure 3.2a-b were obtained at 271 K internal sample temperature. Little change is seen at higher temperatures (up to room temperature), or down to 257 K (Figure 3.2c,f,i). Note that the water present in the typical densely packed, mm-sized MAS NMR samples have a much suppressed freezing temperature [68], causing the water to remain liquid down to -15 to -20°C. The (lack of) freezing of the water is conveniently probed by observation of the water ^{1}H signals. The liquid water has a narrow and intense signal (e.g. Figure 3.2i), which is greatly reduced and broadened upon freezing (e.g. Figure 3.2j). Similarly, these ^{1}H spectra will also reveal changes in the fluidity of lipid acyl chains (see below).

The initially low intensity in the CP spectra is due to the dynamics experienced by the protein and lipids. These protein and lipid dynamics occur on distinct time scales, as becomes more evident in other types of NMR spectra. In a ^{1}H-^{13}C INEPT spectrum (Figure 3.2f) we see again primarily lipid peaks (see also Figure B.3) and virtually no protein signals. The INEPT experiment is very sensitive to T_2 relaxation, and suffers large intensity losses for all but the most mobile atomic sites. The lipid molecules have long T_2 values as they undergo rapid diffusion and dynamics within the fluid bilayer. Cyt-c must be experiencing motion on a slower timescale than the surrounding lipids, leading to shorter T_2 relaxation times [147] and a lack of INEPT signal. Thus, the protein is dynamic but its motion is constrained while it is associated with the membrane. The lack of cyt-c INEPT peaks and the distinct dynamics of the protein and lipids have another important implication. Any unfolded cyt-c segments would be expected to be highly flexible, such that they match the dynamic features of surrounding solvent or lipid molecules [147]. Thus, the lack of INEPT peaks appears inconsistent with a large-scale unfolding of the membrane-bound protein.

Figure 3.2d shows that cooling of the sample results in a dramatic increase of the protein's CP signal. At the same time, the lipid acyl chains still retain their mobility, as evidenced from their intense INEPT (Figure 3.2g) and ^{1}H signals (Figure 3.2j). Immobilization of the protein is therefore coupled to the rigidification of the lipid headgroups (Figure 3.2g) and freezing of the solvent (Figure 3.2j), rather than the immobilization of the lipid acyl chains. The latter occurs at lower temperatures, when we observe a subsequent loss of the lipid acyl signals in the INEPT and ^{1}H spectra (Figure 3.2h,k). This acyl chain rigidification does not translate into a significant increase in the protein's CP signal (Figure 3.2e), further indicating cyt-c's dynamics being coupled to the lipid headgroups rather than the hydrophobic membrane core. This strongly suggests the protein to be located outside the hydrophobic membrane core, in a peripherally bound state, and mirrors prior ssNMR studies of a different peripheral membrane protein [148].

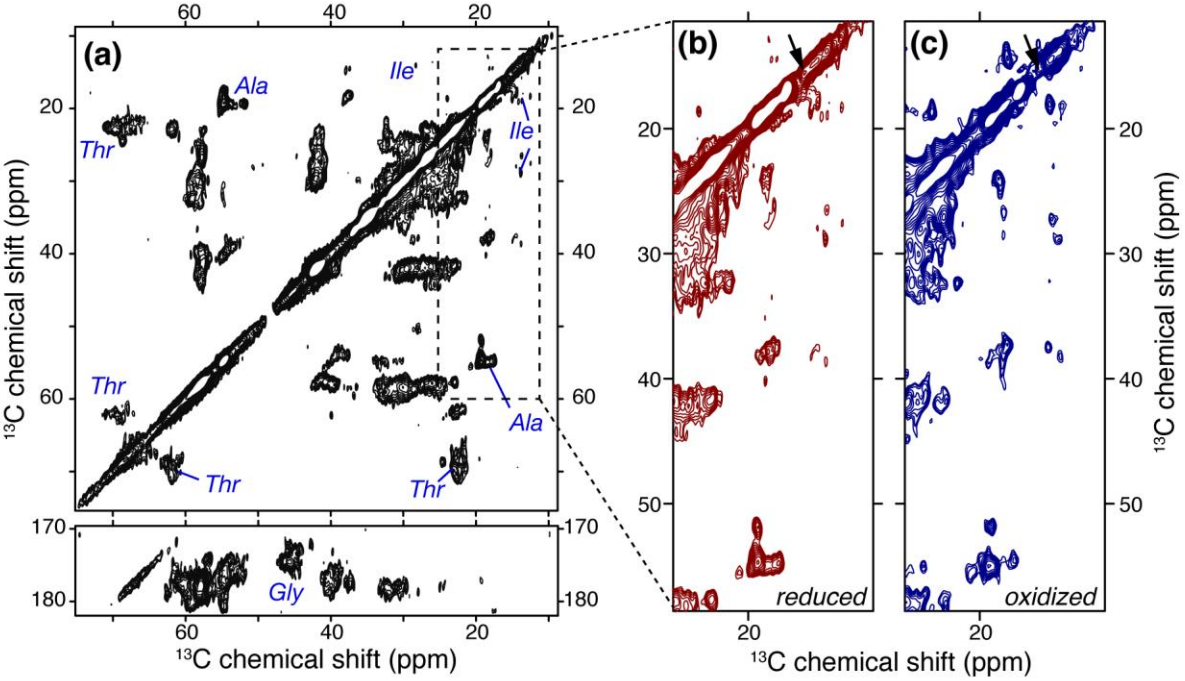

Figure 3.3. 2D MAS ssNMR on LUV-bound U-^{13}C,^{15}N cyt-c

(a) ^{13}C-^{13}C ssNMR spectrum on 0.75 mg reduced ^{13}C,^{15}N-cyt-c bound to DOPC/TOCL (4/1) LUVs at a P/L = 1:40. Off-diagonal cross-peaks are due to ^{13}C-labeled protein, with selected residue types indicated. The dashed box indicates the region enlarged in (b). The spectrum was obtained using 15 ms DARR mixing, at 236 K, 8.33 kHz MAS and 600 MHz (^{1}H frequency). (b,c) Spectral regions before and after conversion of membrane-bound reduced cyt-c to the oxidized state. Minor chemical shift and intensity changes affect Ile and other methyl-bearing residues. Arrows indicate the Met80 ^{13}C$^{\varepsilon}$ chemical shift for reduced cyt-c in solution [132].

3.3.3 Bound cyt-c retains a well-defined conformation

The enhanced CP efficiency at reduced temperatures enabled multidimensional MAS ssNMR studies of the labeled protein. This will allow site-specific insight into the structure of the immobilized protein, although it also implies the loss of direct insight into the dynamics that the protein experiences at the higher temperatures employed in the activity assays. Figure 3.3a shows a 2D ^{13}C-^{13}C MAS NMR spectrum that was obtained on the LUV-bound reduced U-^{13}C,^{15}N cyt-c. It features many protein-derived cross peaks that can only be from the fully ^{13}C-labeled protein. These peaks are sufficiently narrow to resolve many individual atomic sites in distinct residues, which then allows for site-specific insight into protein structure. Residues throughout a protein tend to have distinct NMR signals (high dispersion) in folded proteins, or quite similar NMR signals (low dispersion) in the absence of a well-defined fold. The observed resolution and dispersion of the membrane-bound cyt-c are not consistent with a disordered unfolded state, and show that the protein retains a high degree of structural order. The evidence supporting this conclusion will be examined in more detail below. Previous reports indicated differences in conformation, dynamics, and membrane-binding characteristics of cyt-c as a function of its oxidation state [126, 130, 149-151]. We examined whether this translates into a detectable change in conformation of the LUV-bound protein. The reduced sample (Figure 3.3a-b) was recovered, treated with ferricyanide for in-situ oxidation [152], and then re-packed into its sample holder. The change in redox state was monitored by UV absorbance (Figure B.4) [145]. The complete 2D ^{13}C-^{13}C spectra of the reduced and oxidized samples are shown in Figure B.5 in Section 1.01(a)(i)Appendix B, and enlarged regions shown in Figure 3.3b-c. Separately, another sample of U-^{13}C,^{15}N-cyt-c was oxidized *prior to* LUV binding and packed for MAS NMR. In both cases, 2D ^{13}C-^{13}C MAS ssNMR spectra resemble those of the reduced protein, in terms of resonance frequencies, line widths, and peak counts (Figure 3.3; Figure 3.4a). A few specific differences are visible in the spectral regions in Figure 3.3b-c, which will be examined in more detail in the Discussion in 3.4**.**

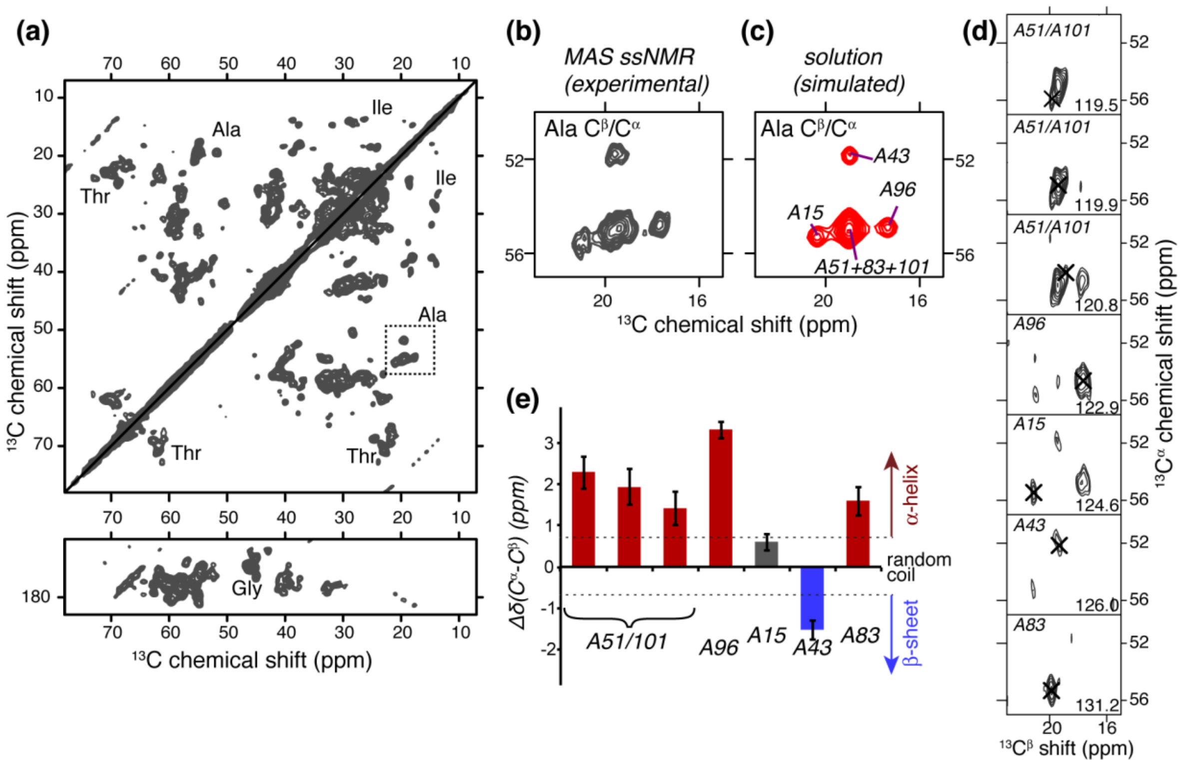

Figure 3.4. 2D and 3D MAS NMR

(a) 2D ^{13}C-^{13}C spectrum on 1.7 mg oxidized ^{13}C,^{15}N-cyt-c bound to DOPC/TOCL LUVs, obtained with 10 ms DARR mixing. Selected residue types are indicated and the dashed box marks Ala C^{α}-C^{β} cross-peaks. The spectrum was processed with four-fold zero-filling after 15 Hz Lorentzian line sharpening and 40 or 50 Hz Gaussian line broadening in the direct and indirect dimensions, respectively. (b) Enlargement of the Ala C^{β}-C^{α} cross-peaks; (c) Analogous (simulated) peaks from solution NMR data [132] on the soluble protein (see text for details). (d) 2D slices from a 3D NCACX spectrum reveal distinct Ala signals (black X), at ^{15}N shifts shown at bottom right. Tentative assignments based on correspondence to solution NMR shifts are indicated. (e) MAS NMR secondary chemical shifts $\Delta\delta(C^{\alpha}$-$C^{\beta})$ deviate from random coil values (at zero) and indicate mostly α-helical structure for the Ala, in line with the native structure (Figure 3.1a). Dashed lines at ±0.7 ppm indicate the typical boundaries to the random coil regime. Experiments performed at 233 K, 8.33 kHz MAS, and 600 MHz (for ^{1}H).

3.3.4 On the conformation of the membrane-bound oxidized cyt-c

These multidimensional MAS NMR spectra on the oxidized sample obtained at low temperatures provide new insight into the conformation of the membrane-bound cyt-c. First, we examine the easily identifiable cross-peaks from cyt-c's Ala residues, which are distributed throughout the protein (Figure 3.1) and thus should reveal both global and local structural changes. In the 2D spectrum four distinct Ala C^{α}-C^{β} cross-peaks are seen with varying peak intensities (boxed in Figure 3.4a and enlarged in Figure 3.4b). As cyt-c has six Ala residues (see Figure 3.1a), this could indicate missing peaks due to unfolding-induced disorder or dynamics, peak overlap, or a combination thereof. To evaluate this, we also obtained a 3D NCACX spectrum on the sample, which offers the ^{15}N resolution needed to reveal the existence of as many as seven Ala $^{15}N/^{13}C^{\alpha}/^{13}C^{\beta}$ peaks (Figure 3.4d). The C^{α} and C^{β} chemical shifts depend on the presence or absence of secondary structure, with opposite effects of α-helical or β-sheet structure. This is reflected clearly in the "secondary shift" $\Delta\delta_{C\alpha\text{-}C\beta}$ (the difference between C^{α} and C^{β} shifts minus the corresponding random coil value), which is zero for random coil conformations and deviates in positive or negative directions, depending on the type of secondary structure (see. Figure 3.4e) [153]. The secondary shifts of the Ala seen in the 3D spectrum are plotted in Figure 3.4e, and indicate that most are α-helical in structure (red bars), rather than random coil. Similar analyses applied to other residue types also show that there are many peaks that are inconsistent with random coil structure. However, broad lines and extensive peak overlap in the 105-residue protein (with e.g. ten Thr) limit this analysis for other residue types. A different kind of analysis proved more fruitful, as will be discussed next.

We used the NMR chemical shifts obtained in these low-temperature ssNMR experiments to compare the membrane-bound structure to that of the un-bound protein. NMR shifts are highly sensitive to a protein's conformation, and both the structure and the NMR signals of the soluble protein are known [132]. Based on these solution NMR shifts, we created synthetic ^{13}C-^{13}C spectra as shown in Figure B.6, in Section 1.01(a)(i)Appendix B, with the Ala peaks reproduced in Figure 3.4c. Comparison of Figure 3.4b and Figure 3.4c illustrates the remarkable similarity that characterizes most of the spectrum (Figure B.6). Clearly, the Ala peak pattern is perfectly reproduced, and even the individual ^{13}C shifts show only minor differences. Based on this close correspondence, we were even able to make the Ala assignments indicated in Figure 3.4d-e. More generally, there is a good correspondence between the peak patterns of various easily identifiable residue types (Figure B.6g-i). That said, it does appear that a number of peaks are moved, missing, or attenuated. Whilst other Ile peaks are easily identified (Figure 3.3), Ile81 is for instance missing or showing up at a different chemical shift. This Ile is part of a proposed membrane-binding site (more below) and stands apart in the solution data by its particularly high-field $^{13}C^{\delta}$ shift, which is not seen in our ssNMR data. Based on observed variations in the peak intensities, it is also likely that a subset of peaks is affected by line broadening due to structural heterogeneity or residual dynamics, causing them to be hard to resolve or detect. Nonetheless, Figure B.6 shows that the degree of correspondence between the ssNMR and solution NMR signals is remarkable. This implies a strong preservation of the native conformation and is not consistent with the membrane-bound protein experiencing a large degree of unfolding or denaturation [109-114]. A more detailed analysis of the protein's structure will require *de novo* ssNMR assignments and further structural measurements.

3.3.5 FTIR corroborates the preservation of secondary structure

We also performed FTIR on membrane-bound and free cyt-c at room temperature, using analogous samples as used for ssNMR. The employed cyt-c was not isotopically labeled, but was otherwise obtained using the same construct and expression protocols as used for the NMR samples. We obtained analogous data for the wild-type protein, similar to prior studies [114, 154]. Figure 3.5 shows the experimental FTIR data, along with a deconvolution of the amide I region. The indicated C=O signals in the membrane-bound spectrum are dominated by the lipids [155]. These room-temperature FTIR results corroborate the preservation of secondary structure in the membrane-bound peroxidase-active protein, consistent with various prior studies (e.g. [111, 112, 154]).

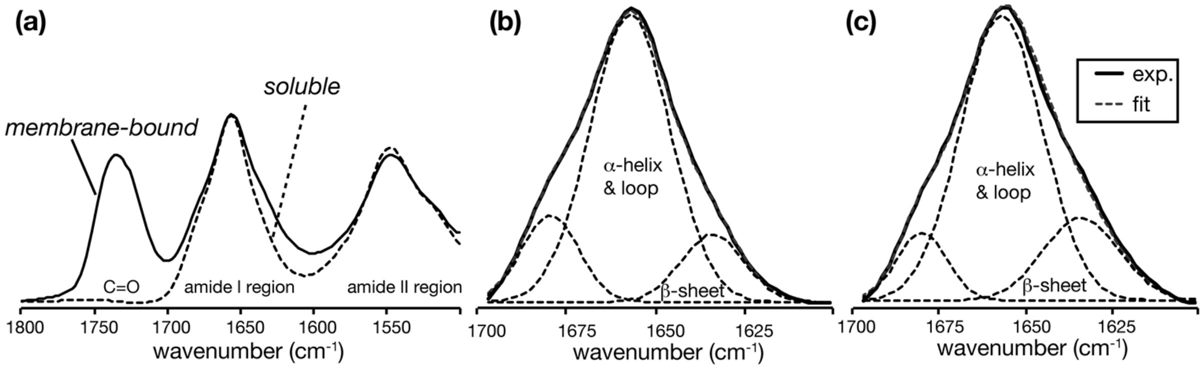

Figure 3.5. FTIR on free and bound cyt-c

(a) FTIR on unlabeled cyt-c in buffer (dashed), and bound at 1:40 P/L to DOPC/TOCL (4:1) LUVs (solid line) at room temperature. (b,c) Deconvolution of the amide I region of soluble and membrane-bound cyt-c, respectively. Individual fit components are shown as dashed black lines and their sum as a dashed grey line.

3.3.6 The cyt-c-bound vesicles retain a lipid bilayer conformation

Several studies have emphasized the ability of cyt-c to cause non-bilayer formation in CL-rich membranes, with potential implications for membrane disruption and OMM permeation in mitochondrial apoptosis [20, 156]. “Static” ^{31}P ssNMR (without MAS) is an excellent tool to detect such bilayer disruption, since bilayer and non-bilayer lipid phases have distinct lineshapes [124, 157]. Briefly, lipid mobility in liquid crystalline bilayers results in uniaxial motional averaging of the phosphate’s ^{31}P chemical shift anisotropy (CSA). This results in characteristic spectra featuring a low-field, low-intensity shoulder and a high-field intense maximum, with an averaged CSA span of 30-40 ppm. Non-bilayer phases feature additional modes of motional averaging, resulting in much narrower line shapes. Cubic phases and (inverted) micellar structures allow for isotropic averaging, resulting in narrow isotropic peaks. Tubular inverted hexagonal (H_{II}) phases have a narrowed, but still anisotropic lineshape with a low-field maximum and a high-field shoulder (i.e. the opposite of bilayers). Figure 3.6 shows the 1D ^{31}P ssNMR spectrum for the sample studied by MAS NMR in Figure 3.4. The spectrum features the characteristic line shape of lipids in a liquid crystalline bilayer. The ^{31}P lineshapes do display the typical features of slightly elongated, not-quite-spherical vesicles in high magnetic fields, as observed previously by us and others [65, 158-160]. This manifests itself as a slight reduction in the low-intensity shoulder (lipids aligned with the field) and an increase in the high-intensity maximum that reflects the lipids oriented perpendicular to the field. The individual components of the CL and DOPC headgroups are visible, allowing extraction of their ^{31}P CSA span values [140], which are found to be 31 and 40 ppm, for TOCL and DOPC, respectively, consistent with prior work [129]. However, we observe no detectable non-bilayer phase signals. Thus, our FTIR and MAS ssNMR data reflect cyt-c as it interacts with the lipids in a bilayer state. This contrasts with prior ^{31}P NMR studies that showed non-bilayer phases, seemingly due to the presence of higher amounts of cyt-c than employed here [21, 110, 127, 161].

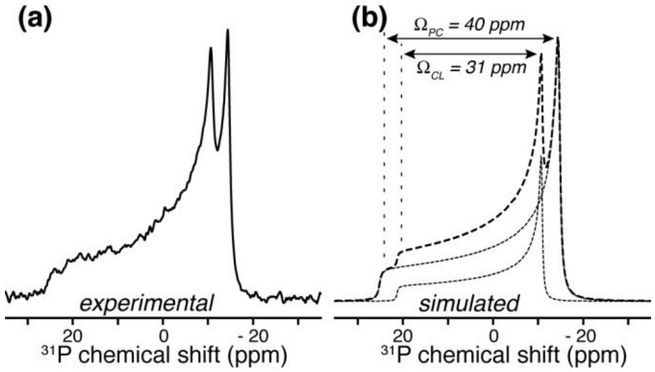

Figure 3.6. Static ^{31}P ssNMR indicates a lipid bilayer structure

(a) 1D ^{31}P static ssNMR spectrum on the oxidized ^{13}C,^{15}N-labeled cyt-c/LUV sample from Figure 3.4. *(b) Simulation of the spectral lineshape (dashed) based on two CSA components (dotted). The magnitudes of the ^{31}P CSA spans (Ω) for CL and PC are indicated.*

3.4 DISCUSSION

3.4.1 Disorder and dynamics of the membrane-bound cyt-c

FTIR, static ssNMR, and MAS NMR were used to probe cyt-c that is bound to LUVs featuring the mitochondrial lipid CL, which is the condition where it displays its proapoptotic peroxidase activity. Previous ssNMR studies suggested the bound protein to be dynamic and largely unfolded, but provided only partial insights due to the limited degree of isotopic labeling [109, 110, 127]. We applied MAS ssNMR to U-^{13}C,^{15}N-labeled, membrane-bound cyt-c, representing one of the first MAS NMR studies of a fully labeled peripheral membrane protein [148]. In line with the known affinity for CL [129, 162], cyt-c was found to associate tightly with CL-containing LUVs, causing the protein to gain significantly increased peroxidase activity (Figure

3.1b-c). The ssNMR spectra revealed extensive dynamics of the bound protein (Figure 3.2). These dynamics occur on a ms-time-scale, explaining the initially low efficiency of both CP- and INEPT-based experiments. Increased dynamics were also noted in previous ssNMR on $^{13}C^{\varepsilon}$-Met-labeled cyt-c [127], and explained as a full or partial unfolding induced by binding to CL-containing membranes. Pronounced protein dynamics have also been reported by studies that employ other spectroscopic methods [111, 112, 154, 163]. Disordered or unstructured proteins or protein segments normally feature dynamics and relaxation behavior that match those of surrounding lipids [147, 164]. However, we found that cyt-c exhibits dynamics that are significantly different from those of the lipids, as evidenced by the lack of protein peaks in the INEPT spectra (Figure 3.2f-h). This complete lack of INEPT signals is inconsistent with an extensively unfolded CL-bound cyt-c, and provides one piece of evidence that the protein dynamics are not necessarily representative of an unfolded state within the membrane. A similar behavior was noted in ssNMR studies of another folded but dynamic peripheral membrane protein [148].

3.4.2 Conformation of the membrane-bound protein

Our low-temperature-enabled 2D and 3D ssNMR spectra, as well as room temperature FTIR, show that the membrane-bound cyt-c retains its secondary structure. In the NMR data, there is little evidence of global structural or dynamic disorder, which would have induced much more substantial line broadening and reduced spectral dispersion [164]. The reproducible observation of these spectral features across multiple samples (in both redox states) shows that membrane-induced unfolding is not occurring under the sample conditions studied here. We do note that much of the ssNMR was performed at low-temperature (unlike the activity measurements). Thus, it is possible that functionally relevant intramolecular dynamics are not represented in those spectra. The observed NMR peak positions are highly sensitive indicators of (changes in) the protein structure, since NMR resonance frequencies are directly correlated to the local protein structure. Comparisons between solution and solid-state shifts can be used to detect structural changes upon protein misfolding, aggregation or membrane binding [63]. The experimental ssNMR spectra closely match the peak patterns predicted from the known solution NMR structure (Figure B.6). This observation is not only inconsistent with the protein being unfolded within the membrane, but also indicates that the retained conformation is rather similar to that of the unbound, soluble state. We examined in particular detail the Ala residues that are distributed throughout the protein (Figure 3.4). As illustrated in Figure 3.1a, cyt-c's Ala are found at the end of N-helix (A15), in the partly α-helical loop before the 60's helix (A43; A51), within the 71–85 Ω loop (A83), and within the C-helix (A96, A101) [165]. Changes in their NMR signals should accompany any significant changes in structure throughout the molecule. Our 2D and 3D data (Figure 3.4) revealed as many as seven Ala signals, with secondary ($^{13}C^{\alpha}$-$^{13}C^{\beta}$) chemical shifts [153] that differ from random coil values (Figure 3.4e) and are mostly α-helical as expected for the native protein (Figure 3.1a). The Ala ^{15}N, $^{13}C^{\alpha}$, and $^{13}C^{\beta}$ shifts are also strikingly similar to previously published solution NMR data for native cyt-c [132]. There is some variation in peak intensities, which may be due to some variation in residue-specific dynamics along the length of the protein. Nonetheless, these data require that cyt-c retains a relatively well-ordered protein conformation.

Several key ssNMR spectra (Figure 3.3 and Figure 3.4) were obtained at low temperature, unlike the activity measurements. Suppression of the proteins' dynamics was critical to obtain high quality multidimensional ssNMR spectra, as often seen in membrane protein ssNMR. Low temperature measurements are commonly applied to enable structural studies, whether in X-ray crystallography, ssNMR or other techniques. Naturally, this does modulate and abolish certain dynamical modes present at elevated temperatures. Indeed, the NMR data in Figure 3.2 show clearly the presence of extensive dynamics, which may include some degree of intramolecular motion that could be functionally important. It seems however unlikely that the protein would be largely unfolded or denatured [109-114]. In prior ssNMR studies of highly disordered or “unfolded” membrane-bound proteins or peptides, the membrane-embedded polypeptides maintained a similar (lack of) structure and similar peak positions upon freezing of the membrane [164, 166]. For cyt-c, prior FTIR and binding studies provide no evidence of a dramatic change in structure or membrane-binding between liquid crystalline and gel phase lipids [115, 154]. As discussed above, much (though maybe not all) of the dynamics experienced by cyt-c are likely due to its peripheral association with the dynamic membrane [148].

3.4.3 Location of membrane-bound cyt-c

The MAS NMR data in Figure 3.2 examined the dynamical properties of the solvent, the lipid headgroups, lipid acyl chains and the membrane-bound protein. It was found that changes in the protein’s motion did not correlate to the changes in the hydrophobic acyl chains. Instead, it accompanied the immobilization of lipid head groups, and freezing of the solvent motion. These observations are most consistent with a shallow, peripheral interaction with the membrane. We note that the high degree of similarity of chemical shifts and tertiary structure to those of soluble cyt-c would also be hard to reconcile with the protein being embedded within the highly hydrophobic membrane core, and be more consistent with a relatively hydrophilic environment.

Specific chemical shift differences observed for Met80 and Ile81 lend some support to prior suggestions of their involvement in the membrane facing side of the protein [167]. Prior studies have also shown Met80 to be dislodged upon membrane binding [8, 127, 162, 163, 167]. Moreover, the binding of cyt-c to the negatively charged membranes is greatly reduced upon increasing salt concentrations (data not shown; [168]), which is a characteristic feature of an electrostatically driven peripheral interaction, rather than a hydrophobic interaction with the membrane core. Thus, our data indicate that in our samples cyt-c retains a native-like fold and interacts with the CL-containing membrane via a peripheral interaction with the lipid headgroups. Prior studies showed significant membrane disruption in presence of cyt-c [21, 110, 127, 161]. ^{31}P ssNMR showed that, under the experimental conditions employed here, the lipid bilayer remains intact (Figure 3.6). The abovementioned membrane disruption was seen under different experimental conditions and most importantly with significantly higher P/L ratios. It is possible that the protein's membrane impact would differ qualitatively under such conditions, since electron spin resonance, Raman and other methods have shown membrane-bound cyt-c to undergo further structural changes at higher P/L ratios (beyond P/L ~ 1/20) [167, 169].

3.4.4 Implications for cyt-c's role as a peroxidase in apoptosis and mitophagy

The interest in cyt-c's interactions with CL, and the lipid peroxidase activity that results, relate to the requirement for this cyt-c activity in mitochondrial apoptosis and mitophagy. It has long been argued that some kind of conformational change must underlie the formation of such a peroxidase-active cyt-c/CL complex. We observed the peroxidase activity for the membrane-bound protein and showed cyt-c to be highly dynamic. Our spectroscopic studies of the bound protein suggest that (at least under the employed experimental conditions) this motion is not due to a complete unfolding of the protein. Our data also indicate that cyt-c interacts primarily with the membrane interface without extensively perturbing the lipid bilayer or penetrating deeply into the hydrophobic membrane core. It is important to point out that the interaction of cyt-c with membranes is well known to depend on the experimental conditions. Whilst our measurements were performed at neutral pH, it has been shown that more acidic conditions enable a different binding mode relying on hydrogen bonding instead of ionic interactions [168]. This could in part explain some of the differences in prior ssNMR studies that were performed at pH 6-6.3 [109, 127]. As discussed above, the binding affinity and binding mode are also expected to be sensitive to the P/L ratio, salt concentration, lipid composition, and other experimental conditions [167, 169, 170].

Our observations fit well with the generally accepted idea that electrostatically driven interactions between cyt-c and the negatively charged CL head groups drive the initial protein-membrane interactions [115, 171, 172]. The surface-bound cyt-c would bind specifically and tightly to multiple charged CL headgroups, while locally enriching the membrane in CL lipids. Our data suggest however that this initial interaction is not necessarily followed by a large-scale loss of structure within the membrane core. Such unfolding would facilitate interactions between the heme and the lipid acyl chains and thus rationalize the lipid peroxidation activity. However, one might expect penetration of the largely unfolded protein to at least partly decouple the disordered polypeptide chain (and heme) from the CL that facilitated the initial binding event. Accordingly the freed heme could interact more easily with the diversity of acyl chains present within the membrane, predicting a somewhat indiscriminate peroxidation activity. However, as noted above and previously [13, 107, 108], the in vivo peroxidase activity displays remarkable selectivity, with specific types of lipids (in particular CL) and acyl chains being the preferred substrates for cyt-c's peroxidase activity. Based on our data, we propose that this may be explained by a formation of a more compact, folded CL-cyt-c complex in which the protein retains a native-like fold and the heme remains largely sequestered within the protein. This would preserve a specific interaction with a cluster of CL lipids, thus enhancing access to CL and limiting access to other lipids. Secondly, the more limited access of the active site in this peripherally bound state, would also place structural and dynamic constraints on the acyl chains, as is discussed next.

At first glance, one may wonder how an interfacial interaction would allow cyt-c to catalyze the efficient peroxidation of the acyl chain double bonds of CL, deep within the membrane core. The extended lipid anchoring model may suggest that a close interaction between the heme and an acyl chain necessitates the extraction of CL acyl chains from the bilayer [117, 118]. We propose an alternative model in which dynamics of the lipid bilayer and dynamics experienced by the protein, possibly combined with dynamics *within* the protein, are responsible for transient interactions with the active site of bound cyt-c. This could occur without a permanent loss of the native fold, without deep penetration into the lipid bilayer core or lipid acyl chain extraction. The peroxidase activity *in vivo* mostly targets CL that feature specific PUFA-based acyl chains, over other lipid types [108]. A noteworthy feature of such PUFA chains is that they feature pronounced flexibility along the membrane normal, placing acyl chain segments closer to the bilayer surface than one may expect [173, 174]. Simulation studies on linoleoyl acyl chains, which are preferentially oxidized by cyt-c [108], have noted the reduced density and high disorder of these acyl chains, in particular near the head groups [175]. This is dramatically different from what happens in saturated lipids. Thus, even in a superficial binding mode, the dynamic nature of both the PUFA-containing membranes and the membrane-associated protein may enable the necessary proximity between the protein's active site and the PUFA double bonds. Then, a relatively subtle or localized structural or dynamical change in the cyt-c would be sufficient to allow lipid peroxidation to occur. Recent X-ray crystallographic studies show how cyt-c mutants can gain a much enhanced peroxidase activity (in absence of lipids) through such localized structural changes [119, 120].

3.5 CONCLUSION

We have used an array of experiments to probe the structure and function of membrane-bound state of cyt-c. We found a CL-induced gain in peroxidase activity, but did not find evidence for a significant loss of the native structure, in contrast to various prior reports. Rather, our results suggest that a more modest change in the protein's structure may be sufficient to cause peroxidase activation. Of course, it is possible that more extensive unfolding occurs under other conditions, e.g. in terms of protein-to-lipid ratio and/or lipid composition,. The conditions employed here reflect limiting CL and ROS concentrations, as thought to be present early in the apoptotic process. Insights into the membrane-bound protein, and its effect on the lipid bilayer, were made possible by our use of complementary ssNMR measurements. We expect that these (and other) ssNMR methods will continue to be essential and powerful tools for ongoing and future efforts to elucidate the membrane interactions of cyt-c as well as other peripherally binding membrane proteins.

3.6 ACKNOWLEDGEMENTS

We thank Alexandr Kapralov for advice and training on the activity assays, Travis Wheeler at the Department of Cell Biology machine shop for construction of the packing tools, and Mike Delk for technical assistance. We thank Jun Li, Naveena Yanamala, and Judith Klein-Seetharaman for helpful discussions and the preparation of earlier ssNMR samples. Funding support was from the University of Pittsburgh (J.A., P.vdW.), the National Institutes of Health (grants HL114453, U19 AIO68021, and ES 020693 to VK; T32 GM088119 to C.L.H.), National Institute for Occupation Safety and Health (NIOSH) Grant OH008282 (V.K.), Human Frontier Science Program Grant HFSP-RGP0013/2014 (V.K.), and grant UL1 RR024153 from the National Center for Research Resources (NCRR).

4.0 MAS ^{1}H NMR PROBES FREEZING POINT DEPRESSION OF WATER AND LIQUID-GEL PHASE TRANSITIONS IN LIPOSOMES

Adapted with permission from: **Mandal, A.**, and van der Wel, P.C.A. MAS ^{1}H NMR probes freezing point depression of water and liquid-gel phase transitions in liposomes, *Biophysical Journal 111(9)*, 1965-1973. Copyright 2016 with permission from Elsevier.

Author contributions: A.M. made samples and performed experiments; A.M. and P.v.d.W. designed research, analyzed data and wrote the manuscript.

The lipid bilayer typical of hydrated biological membranes is characterized by a liquid-crystalline, highly dynamic state. Upon cooling or dehydration, these membranes undergo a cooperative transition to a rigidified, more ordered, gel phase. This characteristic phase transition is of significant biological and biophysical interest, for instance in studies of freezing-tolerant organisms. Magic-angle-spinning (MAS) solid-state NMR (ssNMR) spectroscopy allows for the detection and characterization of the phase transitions over a wide temperature range. Here we employ MAS ^{1}H NMR to probe the phase transitions of both solvent molecules and different hydrated phospholipids, including tetraoleoyl cardiolipin (TOCL) and several phosphatidylcholine lipid species. The employed MAS NMR sample conditions cause a previously noted substantial reduction in the freezing point of the solvent phase. The effect on the solvent is caused by confinement of the aqueous solvent in the small and densely-packed

MAS NMR samples. Here we report and examine how the freezing point depression also impacts the lipid phase transition, causing a ssNMR-observed reduction in the lipids' melting temperature (T_m). The molecular underpinnings of this phenomenon are discussed, and compared to previous studies of membrane-associated water phases and the impact of membrane-protective cryoprotectants.

4.1 INTRODUCTION

Integral membrane proteins are essential for many cellular functions and represent important drug targets. The ability of membrane-embedded proteins to perform their biological activity is frequently influenced by, and even dependent on, the structure, dynamics, and physical properties of the surrounding lipid bilayer [18, 176-178]. Moreover, critical biological processes such as membrane fusion and fission require the modulation of physical and structural properties of the membrane. To probe the molecular underpinnings of these processes, there has been an ongoing effort to understand the fundamental character of lipid bilayers, based in large part on the study of membrane-mimicking lipid vesicles [179]. Under biologically relevant conditions, biomembranes feature a lipid bilayer that is in a liquid crystalline, highly dynamic, state. Upon changing of conditions, lipid membranes can experience cooperative phase transitions between fluid and gel-like phases, and between bilayer and non-bilayer assemblies. These phase transitions occur in response to changes in the level of hydration, temperature and membrane composition. There is much interest in these phenomena, for instance in context of the protective mechanisms employed by drought- and freezing-tolerant organisms [23]. An improved understanding of the impact of solvent and lipid freezing on the structure of membranes is also important for structural biology methods that employ low temperature conditions to study lipid-bilayer-embedded proteins.

Both low temperature and sample dehydration can lead to a lipid or lipid mixture undergoing a transition from the liquid crystalline (L_α) to the gel state. The transition temperature between the L_α and gel phase is known as the melting temperature (T_m). This kind of phase transition has important biological consequences, affecting both the barrier function of the membrane and the structure and function of membrane-associated proteins. Thus, it is not surprising that organisms and cells modulate their membranes' acyl chain composition in response to changes in e.g. growth temperature [180-182]. It is also known that membrane-interacting proteins and peptides modify the phase behavior of their lipid membrane environment [123, 157].

Given the above, there has been a longstanding interest in studying the molecular underpinnings of lipid structure, dynamics, and phase behavior. Depending on their chemical structure, different lipids can have dramatically different transition temperatures. Although a lipid's T_m depends on both the type of lipid head group and the identity of the attached acyl chains (Figure 4.1), it is well-established that the acyl chains have a particularly prominent effect [183, 184]. Despite having different headgroups (in both charge and size), 1,2-dipalmitoyl -*sn*-glycero-3-phosphocholine (DPPC) and 1,2-dipalmitoyl -*sn*-glycero-3-phosphoglycerol (DPPG) have similar T_m values of 41.3 and 41.5 °C, respectively (Figure 4.1A-B) [184, 185]. In comparison, the mono-unsaturated variants, DOPC and DOPG have T_m values of -18.3 and -18 °C (Figure 4.1C-D). Thus, the T_m of a lipid bilayer strongly correlates to the acyl chain structure [183]. These data also illustrate the general observation that the introduction of double bonds cause increased disorder and thus lowers the T_m. Thus, the gel transition reflects an event that predominantly involves the acyl chains, and appears to be decoupled from the headgroup and solvent motion. The apparent independence of solvent and acyl chain dynamics can also be appreciated from the abovementioned DOPC and DOPG T_m values, which are well below water's freezing point.

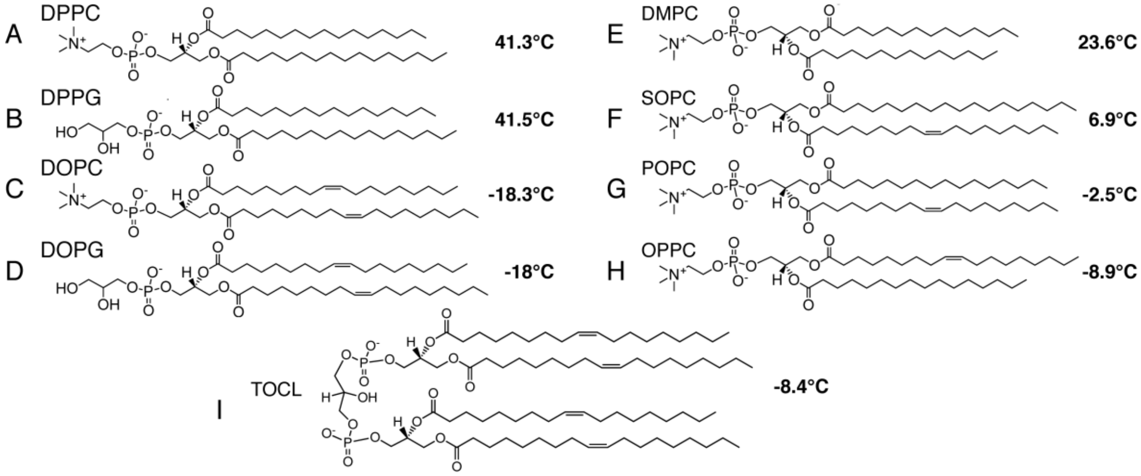

Figure 4.1. Phospholipid species and their gel-to-liquid crystalline phase transition temperatures (T_m)

(A) DPPC, (B) DPPG, (C) DOPC, (D) DOPG, (E) DMPC, (F) SOPC, (G) POPC, (H) OPPC, and (I) TOCL. The corresponding T_m value is indicated alongside each lipid species, based on literature reports [184, 185] and differential scanning calorimetry (DSC; Figure C.7 in Section 1.01(a)(i)Appendix C).

These insights are derived from numerous studies reporting transition temperatures based on a variety of techniques, including X-ray methods, calorimetry, and nuclear magnetic resonance (NMR). Among these methods, the use of solid-state NMR (ssNMR) is based on its ability to detect changes in the site-specific dynamics of lipids, which undergo dramatic changes at the transition temperatures [124, 186, 187]. SSNMR measurements of order parameters and relaxation rates provide direct insight into the dynamics of individual chemical groups along the lipid acyl chains and head groups. Classical ssNMR studies took advantage of the ability of ^{31}P NMR to probe the dynamics of the lipid headgroups and thus detect the phase transitions [188].

^{2}H NMR on lipids with deuterated acyl chains allows the extraction of site-specific order parameters, within the hydrophobic core of the lipid bilayer. More recent ssNMR studies of membranes increasingly employ magic-angle spinning (MAS) to permit the observation of individual ^{13}C and ^{1}H lipid sites, without isotopic labeling [189-193]. Another benefit of MAS-based ssNMR is that it also provides powerful tools to study proteins associated with the membrane [194, 195]. This allows unique opportunities to probe how membrane dynamics and phase behavior affect the structure and dynamics of membrane-bound proteins [14, 142, 147, 196].

We recently reported on our MAS ssNMR studies of peripherally membrane-bound cytochrome c [14], in which we observed the correlated dynamics of lipids and lipid-bound protein, in line with prior studies [142, 147]. In the course of that work we also noted a surprising degree of apparent correlation between the dynamics of the hydrophobic core of the membrane and the dynamic properties of the bulk solvent. Here, we provide an in-depth and systematic examination of this phenomenon, through the use of MAS NMR spectroscopy. We show a consistent impact on the T_m of a variety of hydrated lipids, in absence of protein. The observed phase transition behavior furthers our understanding of lipid bilayer dynamics and phase behavior, with associated implications for our understanding of membrane cryoprotection in biology and in low-temperature structural biology of whole cells and membrane proteins.

4.2 METHODOLOGY

4.2.1 Materials

Purified 1,2-dioleoyl-*sn*-glycero-3-phosphocholine (DOPC), 1,2-dimyristoyl-*sn*-glycero-3-phosphocholine (DMPC), 1-stearoyl-2-oleoyl-*sn*-glycero-3-phosphocholine (SOPC), 1-palmitoyl-2-oleoyl-*sn*-glycero-3-phosphocholine (POPC), 1-oleoyl-2-palmitoyl-*sn*-glycero-3-phosphocholine (OPPC) and 1',3'-bis[1,2-dioleoyl-*sn*-glycero-3-phospho]-*sn*-glycerol (TOCL) lipids were obtained from Avanti Polar Lipids (Alabaster, Alabama). The lipid structures are shown in Figure 4.1.

4.2.2 Sample preparation

Stock solutions containing 10 mg of single or mixed lipids in chloroform were dried to a film under N_2 flow and left under vacuum overnight to remove trace solvents. The lipid film was re-suspended by adding 1 mL of Milli-Q H_2O and shaking gently for 15 minutes on a tabletop shaker at room temperature. In the case of lipids with a T_m close to room temperature, the sample was shaken at 32 °C. Multilamellar vesicles (MLVs) were prepared by freeze-thawing the resuspended lipids 5 times as described before [14]. A final sample volume of 35 μl each was packed for all lipid samples. In order to maintain a hydrated environment in the samples, lipid MLVs were pelleted directly into 3.2 mm NMR sample rotors using ultracentrifugation. Excess supernatant was removed after which the sample rotors were sealed prior to ssNMR measurements. The sample pelleting was done as described before [14, 63, 65], using a custom built packing tool reminiscent of sedimentation devices [73]. The packing process involved ultracentrifugation in a Beckman Coulter L-100 XP centrifuge with a SW-32 Ti rotor for 1hr at 134,000 g. For most samples the packing was done at 4 °C, except for DMPC that was packed at 30 °C.

4.2.3 MAS ssNMR spectroscopy

MAS ssNMR experiments were performed on wide-bore 600 and 750 MHz spectrometers (Bruker Biospin, Billerica, MA), as indicated. The former system was used with a 3.2 mm MAS probe with a HCN "EFree" coil, whilst the latter employed a 3.2 mm HCN MAS probe. Unless indicated otherwise, the samples were studied at a MAS rate of 8.333 kHz. Spectra were obtained at specified MAS rates using direct ^{1}H detection at multiple temperature points across a wide temperature range. On the 750 MHz spectrometer, cooling and heating series of 1D spectra for DOPC/TOCL and DMPC samples were acquired at intervals of ~4 °C between 22 °C (49 °C for DMPC) and -38 °C sample temperatures. On the 600MHz spectrometer the 1D spectra for POPC, OPPC, and SOPC were acquired at intervals of 7 °C from 28 °C down to -7 °C, and then at intervals of 1.4°C from a sample temperature of -12 °C to -40 °C. The samples were allowed to equilibrate at each temperature for 15 minutes before a spectrum was acquired. Additional experimental details are specified in figure legends and in text. Temperature was regulated using cooled gas from a BCU-X or BCU II chiller units (Bruker Biospin). All reported temperatures reflect the internal sample temperature, as determined by a combination of external calibration and measurements on the sample itself. The external sample temperature calibrations were performed on a reference KBr sample under identical experimental conditions, in the form of ^{79}Br T_1 and chemical shift measurements [136, 197]. These measurements were complemented with an analysis of the ^{1}H shifts of unfrozen water and lipid methyl peaks, as previously reported

[135, 198]. NMR spectra were processed using Bruker Topspin and NMRPipe software [137]. Indirect referencing of the ^{1}H shifts relative to aqueous DSS (4,4-dimethyl-4-silapentane-1-sulfonic acid) was based on measurement of the adamantane ^{13}C chemical shift [14]. Phase correction, baseline correction and Fourier transformation was applied to all spectra. Exponential line broadening of 5Hz was applied to all spectra acquired on the 600MHz spectromter. Peak picking, peak intensity measurements and plotting were done using CcpNmr Analysis program from the Collaborative Computation Project for the NMR community (CCPN) [138, 139].

4.2.4 Differential Scanning Calorimetry

DSC measurements were performed on a PerkinElmer (Waltham, MA) Pyris 6 DSC instrument in the Materials Characterization Lab of the University of Pittsburgh. Lipid samples were prepared as discussed above. The hydrated MLVs were packed in a sealable sample pan (TA Instruments; New Castle, DE) and cold-welded to hermetically seal the sample. The DSC measurement started with an initial sample equilibration at -30 °C for ten minutes before ramping up the temperature to 20 °C at a scan rate of 2 °C/min. After a ten minute incubation at 20 °C, a cooling run was performed at the same scan rate and then the entire procedure was repeated once more.

4.3 RESULTS

4.3.1 MAS NMR probing of solvents and lipid dynamics

We recently reported on our MAS ssNMR studies of TOCL/DOPC (1:4 molar ratio) LUVs in presence of 2.5 mol-% of membrane-bound cytochrome c [14]. In variable temperature ^{1}H and ^{13}C MAS ssNMR measurements we detected the temperatures at which the solvent froze and the liquid-to-gel transition of the lipids occurred. In line with prior MAS ssNMR studies [68, 199-201], the aqueous solvent (20 mM HEPES buffer at pH 7.4) froze at temperatures significantly lower than 0 °C. This effect stems from the reduced length scales of water pockets in the sample, compared to bulk water that freezes at 0 °C (see Discussion in **4.4**). To our surprise, we also noted a substantial lowering of the lipid phase transition. To gain a better understanding of this unexpected observation, we pursued a series of systematic studies in absence of protein, which we report herein.

In analogy to our prior work [14], we probe the dynamics of the membrane and the solvent via ^{1}H MAS ssNMR measurements. At moderate MAS rates, as employed here, immobilized protons are strongly coupled to each other through ^{1}H-^{1}H dipolar interactions. These strong dipolar couplings lead to a large broadening of the ^{1}H signals in typical solid samples, which causes extensive peak overlap and a dramatic reduction in peak heights. This has led to (biomolecular) MAS ssNMR studies typically avoiding the detection of these ^{1}H signals, instead focusing on ^{13}C or ^{15}N detection. ^{1}H detection in liquid-state NMR experiments is not affected by this line-broadening effect, as the fast isotropic motion of molecules in solution cause motional averaging of the dipolar interactions. This averaging effect permits the detection of high-intensity, narrow peaks. Thus, only highly dynamic lipid and protein segments have narrow and intense ^{1}H signals in MAS NMR. The freezing of solvent and the liquid-to-gel lipid phase transition are detected as dramatic increases in ^{1}H line width and corresponding reductions in peak intensity [190-192].

4.3.2 Phase changes in mono-unsaturated mixed-lipid vesicles

First, we performed MAS ssNMR experiments on MLVs prepared from the same mixture of TOCL and DOPC, at a 1:4 molar ratio, as were used in our prior protein-bound vesicle studies [14]. Thus, we test that the observed lowering of the solvent and water melting points was not due to the membrane-bound cytochrome c. The results of our 1D ^{1}H MAS NMR measurements on hydrated TOCL/DOPC MLVs are shown in Figure 4.2. At room temperature (Figure 4.2A), the mobile water protons yield a sharp peak near 4.8 ppm. At this temperature, we also observe relatively narrow peaks for the lipids' methyl (CH_3) and methylene (CH_2) protons, showing up near 1 ppm (see inset). The CH_3 and CH_2 peak height and widths indicate that the lipid acyl chains are highly dynamic, consistent with the lipids forming a liquid crystalline bilayer phase (L_α) [14, 190-192]. As the temperature is decreased to -9 °C (Figure 4.2C), the water peak moves (in accordance to the known temperature dependence of water ^{1}H shifts [135, 198]), but remains intense and narrow. Thus, the water remains unfrozen even at -9 °C. As is discussed in more detail below, this kind of solvent freezing point depression is typically seen for densely packed MAS ssNMR samples [14, 68, 201]. Consistent with the T_m values of the DOPC and TOCL lipids, which are well below 0 °C (Figure 4.1), the lipid signals also remain narrow, indicating the persistence of the L_α phase [14]. The T_m of hydrated TOCL was not previously reported, to the best of our knowledge, but was determined to be -8.4 °C in differential calorimetry (DSC) measurements shown in Figure C.7 in Appendix C. The peak intensities change notably at -13

°C, when the intensity of the water peak dramatically decreases, indicating a freezing of most of the water in the sample (Figure 4.2C). However, a similar intensity change is not observed for the lipid protons (inset). These lipid proton signals remain intense until the sample is cooled to -22 °C. Ultimately there is a complete loss of signal at the final temperature of -38 °C (Figure 4.2E). The mid-point of the acyl chain dynamical transition was determined from the temperature-dependent acyl chain peak intensities to be at -20 °C (Figure 4.2F). The acyl chain intensity changes were very similar in heating and cooling runs (Figure 4.2F and Figure C.8 in Appendix C), with the cooling and heating transition points differing by a mere ~ 1 °C. Thus, in these pure-lipid samples, we obtain a behavior of both the solvent and lipid dynamics that reproduces the data that we previously reported on DOPC/TOCL LUVs in presence of 2.5 mol-% of membrane-bound cytochrome c [14]. Thus, the noted reduction in the lipid T_m is not due to the effect of the membrane-bound protein.

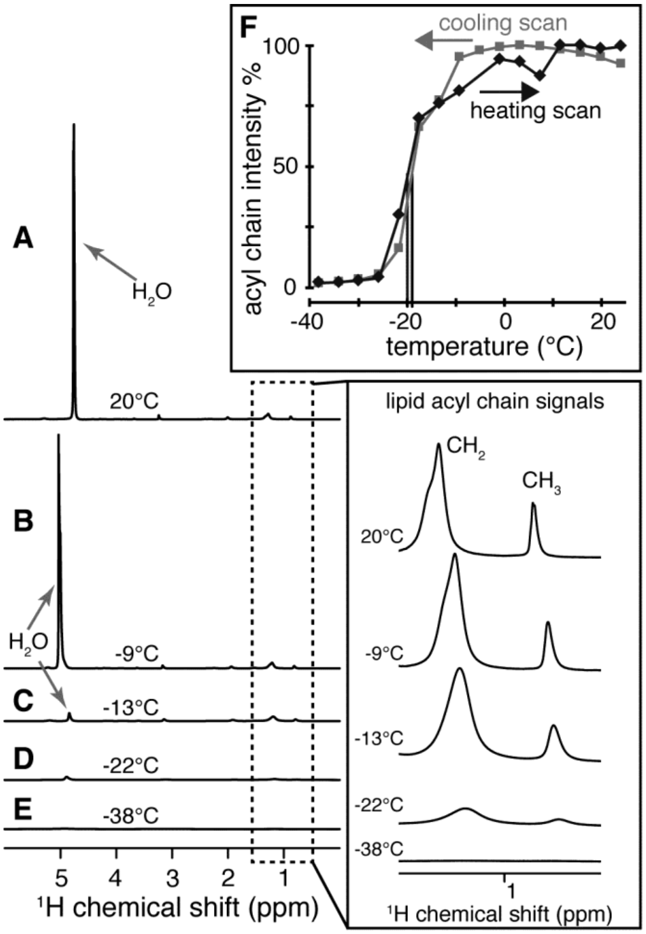

Figure 4.2. ^{1}H MAS ssNMR spectra of DOPC/TOCL MLVs at different sample temperatures

(A) Room temperature: narrow water (~4.8 ppm) and lipid CH_2 *and* CH_3 *peaks indicate liquid-like motion. (B) At -9 °C: Peaks remain narrow and intense. (C) At -13 °C: The water signal is attenuated due to ice formation, but lipid acyl chain signals remain intense. (D) At -22 °C: Water peak has completely disappeared; lipid peaks are partly attenuated due to the lipid phase transition. (E) At -38 °C: All* ^{1}*H peaks are broadened beyond detection. The inset to the right shows enlarged versions of the lipid peaks. (F) Temperature-dependent peak heights for the acyl chain* CH_2 *peaks.*

4.3.3 Lipid and solvent freezing for single-lipid vesicles

Intrigued by these data, we performed analogous variable-temperature measurements on samples consisting of pure lipids with higher transition temperatures (Table 4.1). These single-lipid samples were chosen as they are well characterized and have well-known T_m values determined by various different methods [183-185]. The selected lipid types reflect a range of T_m values: near room temperature (DMPC), near water's normal freezing point (SOPC and POPC), and significantly below zero degrees Celsius (OPPC). The chemical structures and T_m values of the four lipid species are shown in Figure 4.1E-H and Table 4.1. The fully saturated lipid DMPC has the highest T_m value, while the presence of double bonds in the mono-unsaturated lipids (SOPC, POPC, and OPPC) leads to lower T_m values.

Systematic series of ^{1}H MAS ssNMR spectra were obtained for each sample, with cooling runs starting at room temperature (or 49 °C for DMPC) and cooling down to ~ -38 °C sample temperature. As noted above, measured cooling and heating runs were found to yield very similar transition points (Figure 4.2, and Figure C.8 & Figure C.9 in Appendix C). As a function of temperature, we monitored the peak heights of the water and lipid methylene (CH_2) signals, in analogy to the data in Figure 4.2. The obtained results are plotted in Figure 4.3A-D, for each sample, as indicated. In all four samples, the water signal (blue markers) retains a similar intensity down to well below the normal freezing point (indicated with a vertical blue line at 0 °C). The freezing of water occurs around -20 °C, as determined from the midpoint of the observed transition (dashed blue vertical lines in Figure 4.3). We observe variations of a few degrees in the exact temperature at which water freezes in different samples, due to variability in the volume of the bulk water present in the samples or the stochastic nature of ice nucleation.

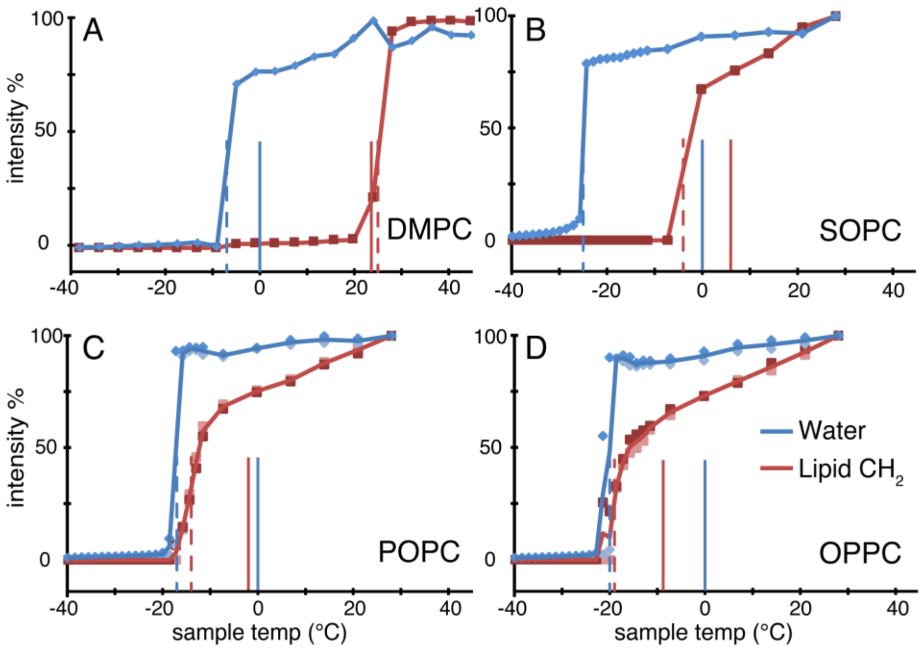

Figure 4.3. Temperature depended peak heights for various lipids

Intensity of ^{1}*H MAS ssNMR peaks of water (blue diamonds) and lipid* CH_2 *groups (red squares) as a function of sample temperature. These peak heights correlate to the dynamics of the solvent and lipid core, respectively. Data are shown for MLVs of DPMC (A), SOPC (B), POPC (C), and OPPC (D). For both water and lipid, the mid-point of the phase transition (*$T_{m,MAS}$*) is marked with dashed vertical lines. Solid vertical lines show the normal* T_m *(red), and 0 °C (blue).*

We determined the lipids' phase transition via a similar analysis of the change in intensity of the CH_2 lipid signals. Figure 4.3 shows these peak heights after normalization relative to the maximum peak intensity across the entire temperature range under study. Similar to the solvent, the lipid acyl chain signals show a relatively sudden intensity drop across a narrow temperature range, as they undergo the cooperative L_α to gel transition. One difference with the solvent molecules is that the lipid acyl chain signals also show a gradual, but notable, temperature-dependent intensity decrease prior to the phase transition. We attribute this to temperature-dependent changes in acyl chain fluidity within the motional regime that affects the NMR relaxation behavior. These motions are sensitive to the viscosity of the membrane core, which is dictated by lipid composition, presence of sterols, and the presence of double bonds. The temperature-dependence in the L_α phase is emphasized in saturated DMPC or partially saturated lipids (SOPC/POPC/OPPC), due to their increased viscosity compared to solvent molecules or lipids without saturated acyl chains (e.g. Figure 4.2).

For each lipid, we determined the apparent T_m value by identifying the narrow temperature range over which the phase transition occurred, and then interpolating the halfway point. The resulting $T_{m,\,MAS}$ points are marked with dashed red lines in Figure 4.3. As a reference point, the figure also shows the published T_m values for each lipid with vertical red solid lines in Figure 4.3 [184]. In the case of DMPC, we find a $T_{m,MAS}$ of 25 °C (Figure 4.3A), which is close the T_m observed by DSC (23.9 °C; data not shown). MAS NMR heating and cooling runs again yield very similar transition point temperatures (Figure C.9 in Appendix C). Unlike DMPC, but similar to the DOPC/TOCL sample, the SOPC, POPC and OPPC MLVs all have $T_{m,\,MAS}$ values that are systematically lower than their normal T_m temperatures (Figure 4.3B-D). As listed in Table 4.1, SOPC, POPC, and OPPC have a T_m at 6.9, -2.5, and -8.9 °C in calorimetric measurements, but here have $T_{m,\,MAS}$ values of -4, -14, and -19 °C respectively.

Table 4.1. Phase transition temperatures

Species	**Acyl chains**	**$T_{m,\,Lit.}$ (°C)**	**$T_{m,MAS}$ (°C)**	**ΔT_m (°C)**
DMPC	C14:0/C14:0	23.6	25	1.4
SOPC	C18:0/C18:1_c	6.9	-4	-11
POPC	C16:0/C18:1_c	-2.5	-14	-11
OPPC	C18:1_c/C18:0	-8.9	-19	-10

Literature T_m values from are from ref. [184], the listed MAS ssNMR T_m values are from this study, and the final column (ΔT_m) lists the difference in T_m.

4.4 DISCUSSION

4.4.1 Freezing of water under MAS NMR conditions

We previously reported the freezing point of water and the T_m of unilamellar lipid vesicles to be depressed in our MAS ssNMR studies of a peripherally-bound protein [14]. Here, a similar reduction in the freezing point of water was observed in MAS NMR studies of a variety of multilamellar lipid samples – both lipid mixtures and pure lipids. As shown in Figure 4.2 and Figure 4.3, the water freezing point was changed by as much as -25 °C (SOPC MLVs; Figure 4.3B). A similar reduction in the water freezing temperature is commonly observed in MAS ssNMR studies of biological samples [66, 68, 201, 202]. For instance, MAS NMR studies on tightly-packed protein crystals showed that the bulk water did not completely freeze until below -15 °C, while crystal waters remained unfrozen until -25 °C [68]. The observed decrease in the freezing point of water is due to confinement effects, sometimes also referred to as capillary effects [68, 203, 204]. In confined spaces the freezing point of water is very much dependent on the heterogeneous nucleation of water [203], causing e.g. small water droplets to have a much lower freezing point [199, 200]. Another potential contribution to the freezing point reduction in these highly concentrated samples may come from the kind of "concentration" or osmotic effect that explains the dose-dependent effects of solutes on the freezing point of the solvent [205]. MAS ssNMR sample holders (rotors) have μL-sized internal sample volumes: approximately 35 μl for the 3.2 mm (outer diameter) rotors employed in this study. More importantly, protocols for preparing MAS ssNMR samples typically maximize signal-to-noise by densely packing the (non-aqueous) material of interest: lipids, proteins, or other (bio)materials. In our studies [14, 63-65], this is routinely accomplished by pelleting membrane or fibril samples in an ultracentrifuge. In the resulting sample, the amount of 'bulk' water is purposely minimized, whilst (even transient) sample dehydration is reliably avoided.

In the resulting samples of tightly pelleted LUVs the total water content constitutes approximately 77 % of the total sample mass [14]. In MLVs there is little bulk water, with most of the water being either within, or associated with, MLV PC vesicles [206]. To gain an appreciation of the different water pools in densely packed lipid vesicle samples, we constructed a simplified schematic model assuming hard-sphere optimal packing of spherical vesicles. This model is illustrated in Figure 4.4. The vesicle spheres have a diameter of 200 nm and a 5 nm total bilayer thickness. The figure also shows the ~25 Å hydration water layer that is associated with the lipid bilayers [207]. The different types of water pools are indicated: intra-vesicular water, membrane-associated hydration water, and inter-vesicle water pockets. The latter pool has also been described as 'lake water' in prior work [208]. Using this highly schematic model, we calculated the expected relative sizes of the different water pools within the packed pellet (inset; Figure 4.4B). Most water (64 %) is within the vesicles, and 26 % is in the inter-vesicle spaces. In 'real' samples the latter number may be smaller due to the ability of the vesicles to deform during sample packing. None of these water pools have length scales exceeding 200 nm, resulting in a confinement that lowers the water freezing point. This effect is not constrained to MAS NMR samples, as prior non-NMR work also reports non-bulk (e.g. interlamellar and internal) water in phospholipid preparations to experience large reductions in its freezing point [23, 209].

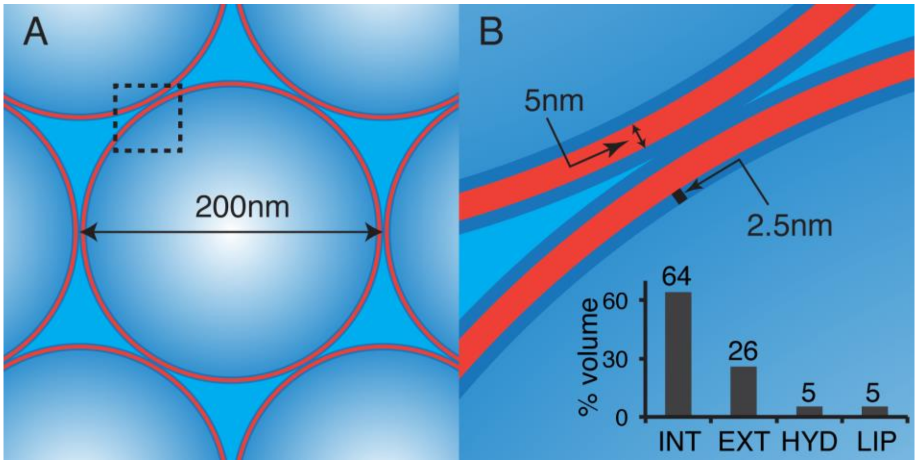

Figure 4.4. Schematic model of the geometry of densely packed LUVs

(A) Hexagonal dense packing of hard-sphere LUVs with a 200 nm diameter. (B) Enlargement of the boxed area from (A). Dimensions of the bilayer (red) and associated hydration water (dark blue) are indicated. The bar graph indicates the volumetric breakdown of water inside the LUVs (INT), between vesicles (EXT), hydration water layers (HYD), and the lipids themselves (LIP).

4.4.2 Lowering of the lipid melting temperatures

Whilst the changes in the freezing point of the hydration water were in line with prior reports on other types of MAS ssNMR samples, we also found a surprising lowering of the T_m of a variety of lipid types and mixtures. Aside from our own recent report [14], we are not aware of prior MAS NMR studies of this particular phenomenon. We find a large reduction (by more than 10 °C) of the T_m of lipids with freezing points that are normally close to, or below, the freezing point of water. In contrast DMPC, which has a T_m near room temperature, showed a much smaller change in its phase behavior. The T_m reduction affects both LUVs and MLVs, in presence and absence of bound protein, and both in pure lipids and mixed lipid vesicles [14].

Thus, this effect appears to be generally applicable to the hydrated lipid bilayers found in these MAS ssNMR samples.

At first glance, there is an apparent analogy between the reductions in the T_m of water and that of the lipid bilayers. Although this may suggest an analogous molecular origin, it is unlikely that similar confinement effects can explain the changed lipid T_m values. Unlike the solvent molecules, the lipid acyl chains are not present in true 3D 'bulk' phase, but are instead constrained to the pseudo-2D lipid bilayer plane. Then, the primary variable in the geometry of lipid vesicles of a certain composition relates to the in-plane bilayer area (i.e. the surface area of spherical vesicles). Neither previous studies, nor our own data, show a strong correlation between this parameter and the observed T_m value, at least in the regime of MLVs and LUVs that we studied. We observe a similar T_m depression in both MLVs and LUVs [14]. Prior work also notes that MLVs and LUVs have very similar T_m values [184, 185]. Thus, the confinement-induced effect does not apply to the lipid phase transition. What is then the cause of the T_m change?

4.4.3 On the potential role of centrifugal forces due to MAS

There are a few experimental parameters that are modulated by the use of MAS, and that conceivably could affect the lipid phase behavior. The centrifugal force caused by MAS can lead to increases in the local pressure and cause dehydration of the lipid bilayers. Both these parameters are known to affect lipids' gel-to-liquid crystalline transitions. Prior studies [210, 211] report that increased pressure causes a shift of the T_m toward higher temperatures. In contrast, we observe a change of T_m toward lower temperatures. We also performed variable temperature measurements on OPPC MLVs at reduced MAS rates of 1 and 5 kHz, with little effect on the detected T_m values (data not shown). Thus, the lowering of the lipid T_m values is not due to increased pressures under MAS.

Centrifugal forces associated with (fast) MAS can also lead to partial dehydration of the lipid headgroups [212]. Might this contribute to the observed lowering of T_m values? First, the dehydration of lipid bilayers is generally only observed at MAS rates well above 10 kHz, whereas all data in this study were obtained at 8.33 kHz or below. Second, dehydration favors the formation the gel phase, as it features fewer water molecules per lipid [213-217]. Indeed, it is well known that dehydration of membranes (and cells) causes a dramatic *increase* in the lipids' T_m, rather than a decrease. Thus, not only is significant lipid dehydration unlikely under the employed conditions, but it would also cause the T_m to change in the opposite direction. Thus, we conclude that the MAS *per se* is not causing the lipid T_m depression.

4.4.4 Connection between lipid T_m and lowering of water's freezing point

We propose that the T_m change of the lipids is an indirect consequence of the freezing point depression of water. Ice formation, gel phase transitions, and membrane dehydration are connected processes [23]. Ice formation in a certain confined pool of water depends on the volume of the water pool, with small volumes or droplets showing dramatically lower freezing points [203]. As a consequence, ice formation happens first in the extra-vesicular bulk water, well before the intra-vesicular or inter-lamellar water pools freeze. This is analogous to the bulk and protein-associated water pools in crystalline and fibrillar protein samples [66, 68, 201, 202]. For lipid vesicles or cellular preparations, the formation of extra-vesicular (or extracellular) ice leads to both a dehydration and a disruption of the lipid bilayer. Dehydration of membranes favors gel formation, and thus causes a dramatic increase in the T_m. Indeed, it is thought that dehydration-induced gel phase formation plays a key role in freezing-induced damage to cells and cellular membranes [23]. As the ice formation happens at much lower temperatures in our samples, the gel-phase-favoring membrane dehydration, which results from the ice formation, does not occur until lower temperatures. Thus, a lower lipid T_m may be achieved if one delays the dehydration effect that accompanies the (normally occurring) ice formation. There may also be another mechanism that takes effect in the absence of ice formation. When the solvent freezes, the lipid headgroup mobility is measurably reduced [14]. The reduced mobility of the headgroups could limit the mobility of the attached acyl chains, which may also favor the gel transition. Lowering of the freezing point of the solvent can delay the gel-phase-transition through one or both of these processes reflecting an indirect coupling of solvent and acyl chain dynamics. Additional insights into their respective contributions may be available via simulation studies [217-219].

4.4.5 Implications

These observations have a number of practical and theoretical implications. First, they enhance our understanding of the fundamental underpinnings of lipid phase behavior, and in particular point to a role for solvent dynamics. The connections between ice formation and cell membrane integrity are also important in ongoing studies of freezing-tolerant organisms and other aspects of cryobiology. A number of prior studies have reported that cryoprotectants, such as trehalose, prevent dehydration-induced T_m increases [220-223]. An interesting aspect of our study is that the freezing point depression was achieved without involvement of direct cryoprotectant-lipid interactions [224]. The obtained results are also of interest for their implications for variable temperature studies of membrane-bound proteins and peptides, as well as whole cells, by MAS ssNMR. This notably includes the ongoing efforts to apply low-temperature dynamic nuclear polarization (DNP) to membrane-embedded proteins and whole cells [225, 226].

4.5 CONCLUSION

We have examined in detail the melting point suppression of aqueous solvent and hydrated lipid bilayers. The solvent's melting point suppression generally affects biomolecular applications of ssNMR, not only to membranes and membrane-associated proteins, but also other kinds of densely packed biological solids. In addition, the surprising impact on the T_m of lipid-based biomembranes enhances our understanding of lipid phase behavior, and may have practical implications ranging from cryobiology to the use of cryoprotectants in the freezing and lyophilization of cells and lipid-based drug-delivery systems [227].

4.6 ACKNOWLEDGMENTS

We thank Joel Gillespie at the Materials Characterization Lab for help with, and training for, the DSC measurements, and thank Mike Delk for help with the NMR instrumentation. Funding support was from the University of Pittsburgh and the National Institutes of Health grant R01 GM113908.

5.0 THESIS SUMMARY

Complete understanding of the mechanism of cyt-c's gain of function during intrinsic apoptosis has implications for Huntington's disease [4, 5] and cancer[6, 7]. However, the study of this system by MAS NMR has certain requirements, such as isotopic labeling and a protocol to pack highly concentrated samples in the rotor. In Chapter 2.0 I highlight the versatility and usefulness of developing such a protocol and discuss in depth the design and use of an ultracentrifugal packing tool that greatly aids in MAS NMR sample preparation. This protocol proved essential for the MAS NMR measurements I was able to obtain on the membrane bound cyt-c sample in Chapter 3.0 Complementing MAS NMR with various other biophysical techniques I was able to verify that the cyt-c does not completely unfold upon membrane binding (Section 3.4.2). These studies allowed for the determination of the cyt-c location on the membrane (Section 3.4.3) and thus we were able to propose a mechanism to explain the peroxidase activity of cyt-c when bound to CL containing liposomes (Section 3.4.4). The peroxidase activity of the system used in the study here is significantly higher in the presence of CL but changes in the experimental system can result in samples with decreased or increased peroxidase activity. Study of these variants can yield more insights into the mechanism of cyt-c's peroxidase activity on a molecular level. This study on cyt-c's peroxidase activity is very timely as many groups have recently published on their investigations in to the structure of the membrane bound cyt-c to gain a better understanding of its peroxidase activity [228-230].

During the course of cyt-c studies we came across interesting phenomena in the MAS rotors where I saw depression in the freezing point of water as well as in the T_m of lipids we used in the study. I investigate these phenomena in detail in Chapter 4.0 These studies on various single lipid vesicle systems and one dual-lipid vesicle system by MAS NMR confirmed the lowering of the lipid melting temperatures (Section 4.4.2). Through these studies I was able to propose a link between the freezing point depression of water in these samples to the decrease in lipid melting temperatures (Section 4.4.4). These results have implications in not only the study of lipid phase behavior, as discussed here, but also in the application of low temperature DNP NMR techniques on membrane embedded proteins and whole cells [225, 226]. Interestingly there may also be implications for our understanding of cryoprotection and cryobiology as this study describes a lowering of lipid T_m without the use of any cryoprotective agents in our samples [224].

APPENDIX A

SUPPLEMENTARY INFORMATION FOR CHAPTER 2

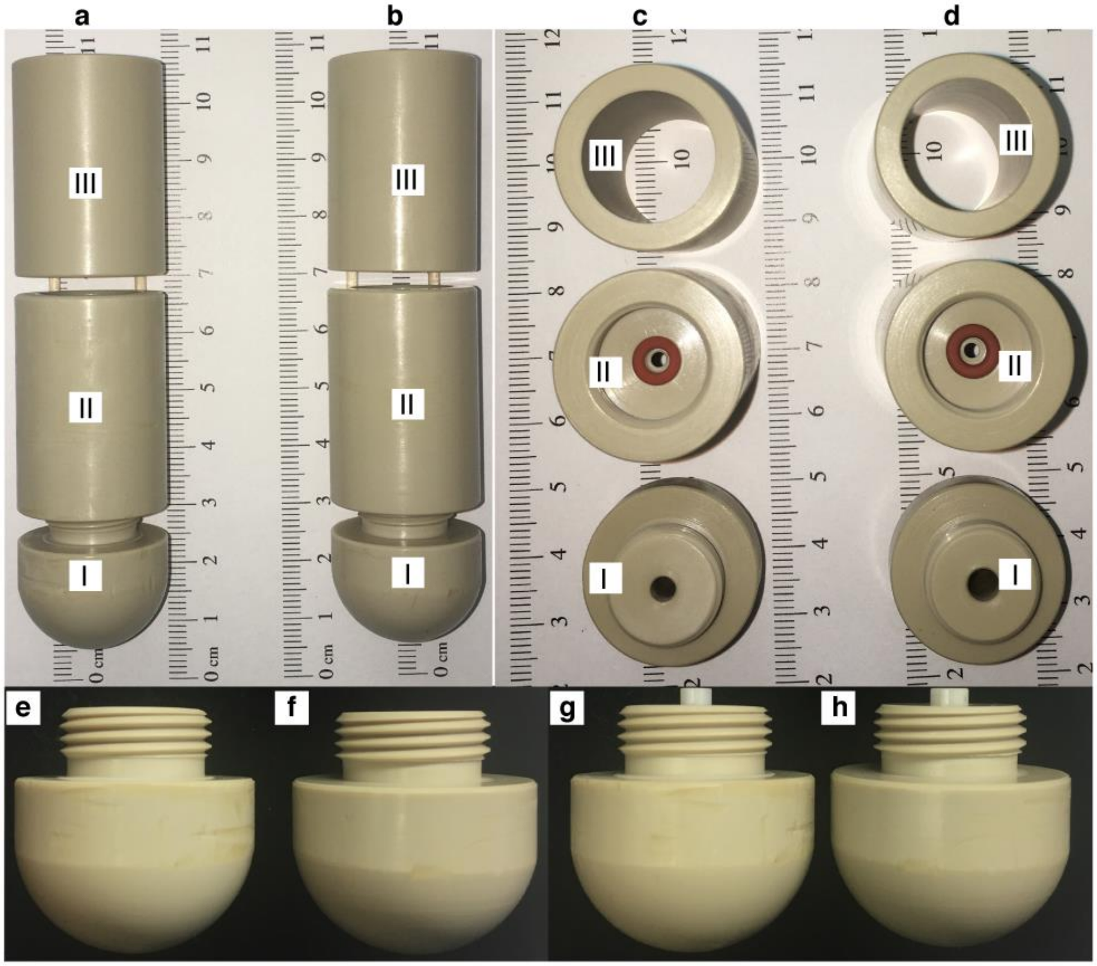

Figure A.1. Photos of the ultracentrifugal devices for packing 3.2 mm and 4 mm Bruker MAS rotors

The component naming scheme is same as in Figure 2.1. *(a) and (c) 3.2 mm packing tool, (b) and (d) 4 mm packing tool. Panels (a) and (b) show the two packing tools side-by-side. Panels (c) and (d) show the internal differences in components I and II between the two tools, necessary to accommodate the different rotor sizes. Part III is identical in both tools. Panels (e,f) show a sideways view of part I of the 3.2 mm packing device, without and with the rotor in place, respectively. Panels (g,h) show a sideways view of part I of the 4 mm packing device, without and with the rotor in place, respectively.*

APPENDIX B

SUPPLEMENTARY INFORMATION FOR CHAPTER 3

Abbreviations: NS, number of scans per t_1 point; Temp., temperature; MAS, magic angle spinning rate; RD, recycle delay; TPPM, ^1H decoupling power during evolution and/or acquisition using the two-pulse phase modulation scheme; P/L, molar protein:lipid ratio.

Table B.1. ***Detailed experimental conditions of ssNMR experiments on the U-^{13}C,^{15}N-cyt-c samples***

Fig	Sample	Expt	NS	Sample Temp (K)	MAS (kHz)	RD (s)	Dec. (kHz)	t_1/t_2 evol. (ms)	Mix (ms)	Contact (ms)	Probe[d]
3.2a	Oxidized U-^{13}C,^{15}N cyt-c (1.7 mg) bound to DOPC/TOCL (4:1) with a P/L of 1:40	^{1}H-^{13}C CP	256	271	8.33	3.2	83	NA	NA	1	Efree
3.2a	Oxidized U-^{13}C,^{15}N cyt-c (1.7 mg) bound to DOPC/TOCL (4:1) with a P/L of 1:40	^{13}C MAS	256	271	8.33	3.2	83	NA	NA	NA	Efree
3.2b	Reduced U-^{13}C,^{15}N cyt-c (0.75 mg) bound to DOPC/TOCL (4:1) with	^{1}H-^{13}C CP	256	271	8.33	4	62.5	NA	NA	1	Efree

Fig	**Sample**	**Expt**	**NS**	**Sample Temp (K)**	**MAS (kHz)**	**RD (s)**	**Dec. (kHz)**	**t_1/t_2 evol. (ms)**	**Mix (ms)**	**Contact (ms)**	**Probe[d]**
	a P/L of 1:40[a]										
3.2b	Reduced U-^{13}C,^{15}N cyt-c (0.75 mg) bound to DOPC/TOCL (4:1) with a P/L of 1:40[a]	^{13}C MAS	256	271	8.33	4	62.5	NA	NA	NA	Efree
3.2c, B.3a	Reduced U-^{13}C,^{15}N cyt-c (0.75 mg) bound to DOPC/TOCL (4:1) with a P/L of 1:40[a]	^{1}H-^{13}C CP	256	257	8.33	4	71	NA	NA	1	Efree
3.2d	Reduced U-^{13}C,^{15}N cyt-c (0.75 mg) bound to DOPC/TOCL (4:1) with a P/L of 1:40[a]	^{1}H-^{13}C CP	256	250	8.33	4	71	NA	NA	1	Efree
3.2e	Reduced U-^{13}C,^{15}N cyt-c (0.75 mg) bound to DOPC/TOCL (4:1) with a P/L of 1:40[a]	^{1}H-^{13}C CP	256	236	8.33	3.2	83	NA	NA	1	Efree
3.2f, B.3b	Reduced U-^{13}C,^{15}N cyt-c (0.75 mg) bound to DOPC/TOCL (4:1) with a P/L of 1:40[a]	^{1}H-^{13}C INEPT	256	257	8.33	4	50	NA	NA	NA	Efree
3.2g	Reduced U-^{13}C,^{15}N cyt-c (0.75 mg)	^{1}H-^{13}C INEPT	256	250	8.33	4	50	NA	NA	NA	Efree

Fig	**Sample**	**Expt**	**NS**	**Sample Temp (K)**	**MAS (kHz)**	**RD (s)**	**Dec. (kHz)**	**t_1/t_2 evol. (ms)**	**Mix (ms)**	**Contact (ms)**	**Probe[d]**
	bound to DOPC/TOCL (4:1) with a P/L of 1:40[a]										
3.2h	Reduced U-^{13}C,^{15}N cyt-c (0.75 mg) bound to DOPC/TOCL (4:1) with a P/L of 1:40[a]	^1H-^{13}C INEPT	256	236	8.33	4	50	NA	NA	NA	Efree
3.2i	Reduced U-^{13}C,^{15}N cyt-c (0.75 mg) bound to DOPC/TOCL (4:1) with a P/L of 1:40[a]	^1H MAS	16	257	8.33	2.5	NA	NA	NA	NA	Efree
3.2j	Reduced U-^{13}C,^{15}N cyt-c (0.75 mg) bound to DOPC/TOCL (4:1) with a P/L of 1:40[a]	^1H MAS	16	250	8.33	2.5	NA	NA	NA	NA	Efree
3.2k	Reduced U-^{13}C,^{15}N cyt-c (0.75 mg) bound to DOPC/TOCL (4:1) with a P/L of 1:40[a]	^1H MAS	16	236	8.33	2.5	NA	NA	NA	NA	Efree
3.3a,b; B.5a, b	Reduced U-^{13}C,^{15}N cyt-c (0.75 mg) bound to DOPC/TOCL (4:1) with a P/L of 1:40[a]	2D ^{13}C-^{13}C DARR	96	236	8.33	3.2	83	350*34.85	15	1	Efree

Fig	Sample	Expt	NS	Sample Temp (K)	MAS (kHz)	RD (s)	Dec. (kHz)	t_1/t_2 evol. (ms)	Mix (ms)	Contact (ms)	Probe[d]
3.3c, B.5c, d	Oxidized U-^{13}C,^{15}N cyt-c (~0.75 mg) bound to DOPC/TOCL (4:1) with a P/L of 1:40[a,b]	2D ^{13}C-^{13}C DARR	192	233	8.33	3	71	310*36	20	1.5	HFCN
3.4a,b	Oxidized U-^{13}C,^{15}N cyt-c (1.7 mg) bound to DOPC/TOCL (4:1) with a P/L of 1:40	2D ^{13}C-^{13}C DARR	192	233	8.33	3/2.5[c]	83	460*34.85	10	1	Efree
3.4d	Oxidized U-^{13}C,^{15}N cyt-c (1.7 mg) bound to DOPC/TOCL (4:1) with a P/L of 1:40	3D NCACX (DARR ^{13}C-^{13}C transfer)	256	233	8.33	2.45	83	34*220.72 / 20*360	10	1 / 5	Efree
3.6	Oxidized U-^{13}C,^{15}N cyt-c (1.7 mg) bound to DOPC/TOCL (4:1) with a P/L of 1:40	^{31}P 1D (static)	512	296	0	3	59	NA	NA	NA	Static
B.3c	DOPC/TOCL (4:1) (no cyt-c)	2D ^{1}H-^{13}C INEPT	64	296	12	2.5	71	288*138.76	NA	NA	4mm MAS

[a] The initially reduced membrane-bound cyt-c sample was unpacked, oxidized while bound to the LUVs, and then re-packed into the same MAS NMR rotor.

[b] Not accounting for minor losses during the re-packing of the sample after oxidation of the protein.

[c] This spectrum was reconstructed by time-domain addition of four experiments with identical conditions except for the recycle delay.

[d] Employed ssNMR probe heads: EFree = 3.2 mm MAS HCN probe outfitted with an "EFree" reduced E-field coil design; HFCN = 3.2 mm MAS HFCN probe with conventional solenoid coil; Static EFree = static ssNMR probe with horizontal "EFree" coil.

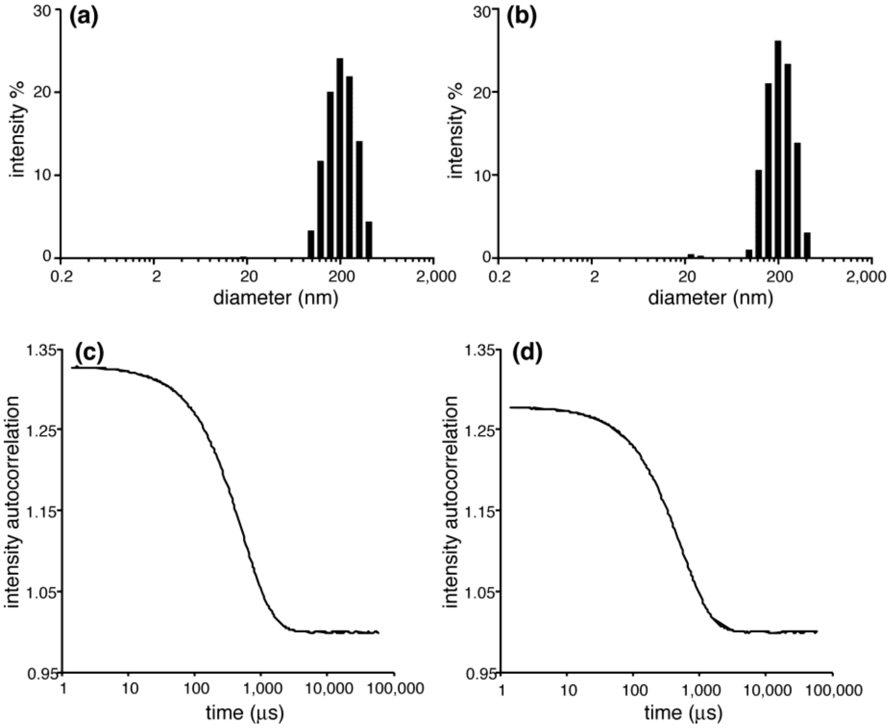

Figure B.2. Dynamic light scattering (DLS) data on the extruded vesicles

DOPC/TOCL (4:1) LUV samples without (a,c) and with (b,d) cyt-c were prepared as described in the main text. The LUVs were obtained by extrusion through a 200 nm membrane, after which either buffer (a,c) or cyt-c stock solution (b,d) is added (for a 40:1 L/P ratio). The vesicles without and with protein have a mean diameter of 216.1 nm with a polydispersity of 37.8nm, or a mean diameter of 216.9 nm with a polydispersity of 34.9 nm, respectively. Panels (a,b) show the histogram plots generated from the autocorrelation data (shown in panels c and d). Measurements were made at room temperature.

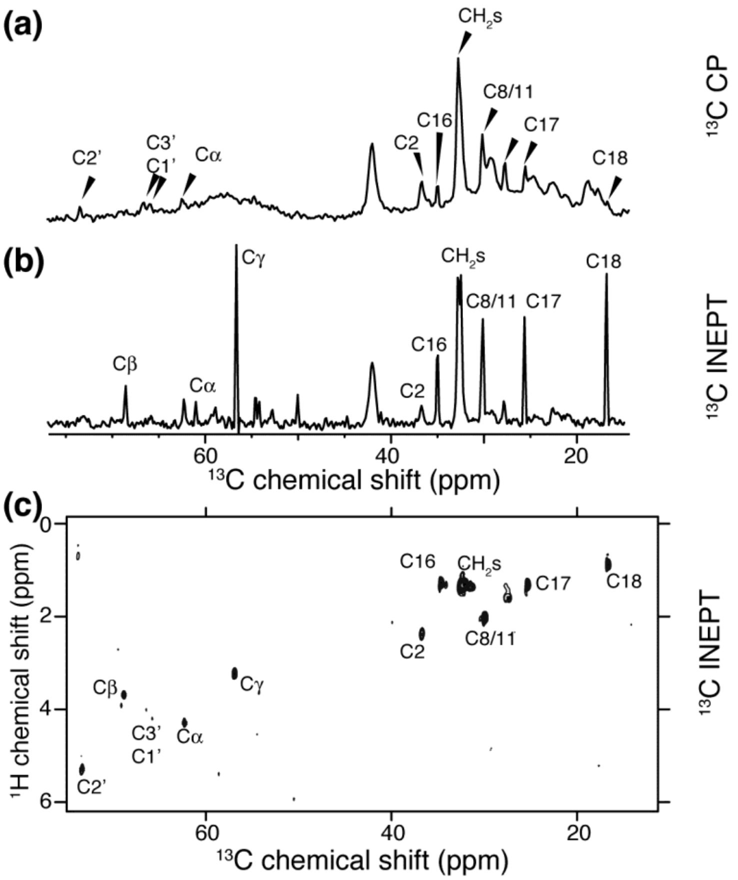

Figure B.3. DOPC/TOCL chemical shifts

1D ^{13}C MAS NMR spectra obtained with (a) ^{1}H-^{13}C CP and (b) ^{1}H-^{13}C refocused INEPT pulse sequences, for the reduced U-^{13}C,^{15}N-labeled cyt-c bound to DOPC/TOCL (4:1 molar ratio) LUVs. Reproduced from Figure 3.2c,f in the main text. The peaks from lipids are indicated, based on comparison to the 2D data in the bottom panel. (c) 2D ^{1}H-^{13}C refocused INEPT-based HETCOR spectrum for DOPC/TOCL vesicles in absence of cyt-c, obtained using a ^{1}H/^{13}C 4-mm MAS probe at room temperature, 12 kHz MAS and 600 MHz (^{1}H frequency). The indicated lipid assignments are based on our prior work and published data [65, 141].

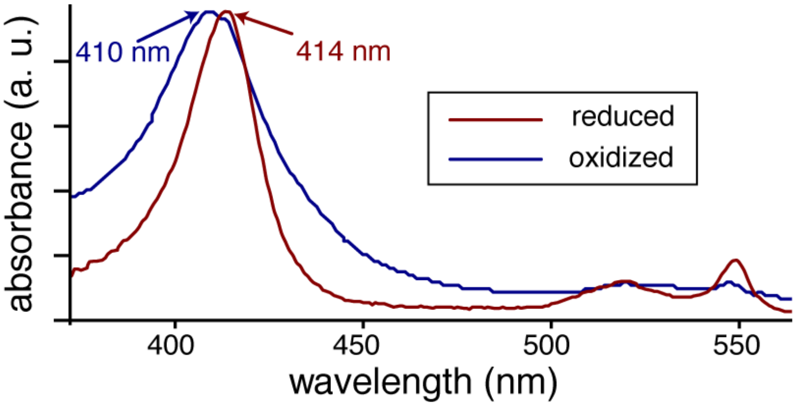

Figure B.4. Monitoring oxidation state of cyt-c by UV-VIS spectra

UV-VIS spectroscopy on LUV-bound U-^{13}C*,*^{15}N*-cyt-c before and after treatment with potassium hexacyanoferrate (III). The characteristic shift in the Soret band maximum near 410 nm is indicated. The obtained scans reproduce the known UV-VIS spectra of reduced and oxidized cyt-c [145]. The measurements were performed at room temperature.*

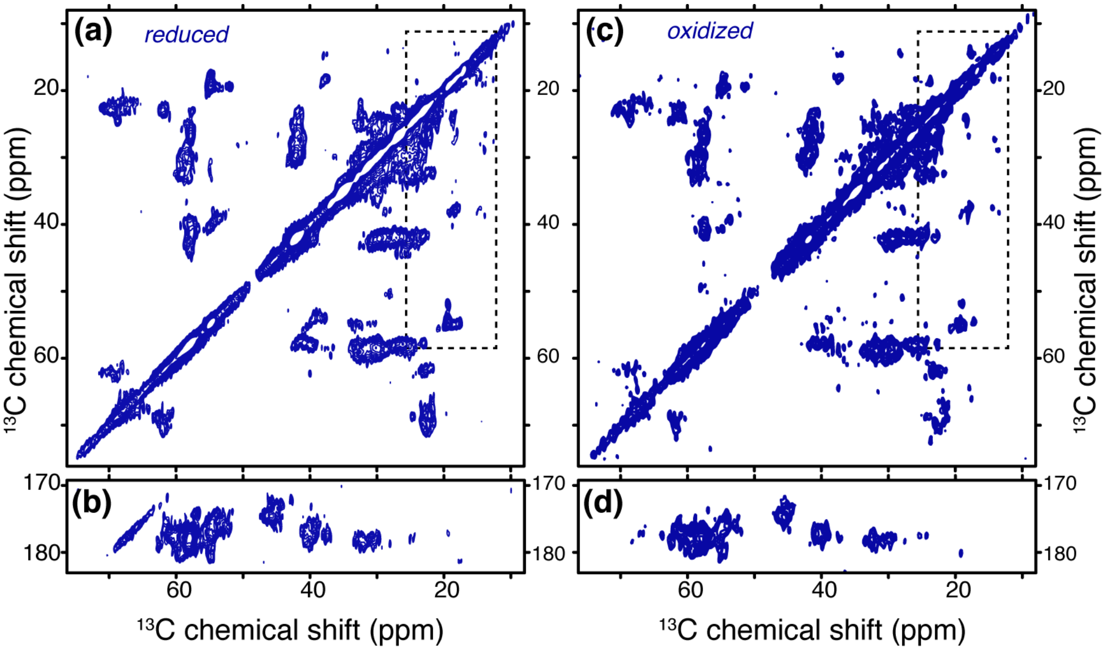

Figure B.5. 2D spectra on cyt-c bound LUVs before and after in-situ oxidation

^{13}C*-*^{13}C *2D spectra on cyt-c bound to DOPC/TOCL LUVs, in the reduced state (a,b) and after in-situ oxidation (c,d). Panels (a,b) are reproductions of Figure 3.3a in the main text. Panels (c,d) reflect the same sample after oxidation. A subsection of panel (c) is shown in the main text as panel (c) of Figure 3.3. The dashed boxes indicate the spectral regions shown in Figure 3.3b-c. For experimental details please refer to Figure 3.3 and Table B.1.*

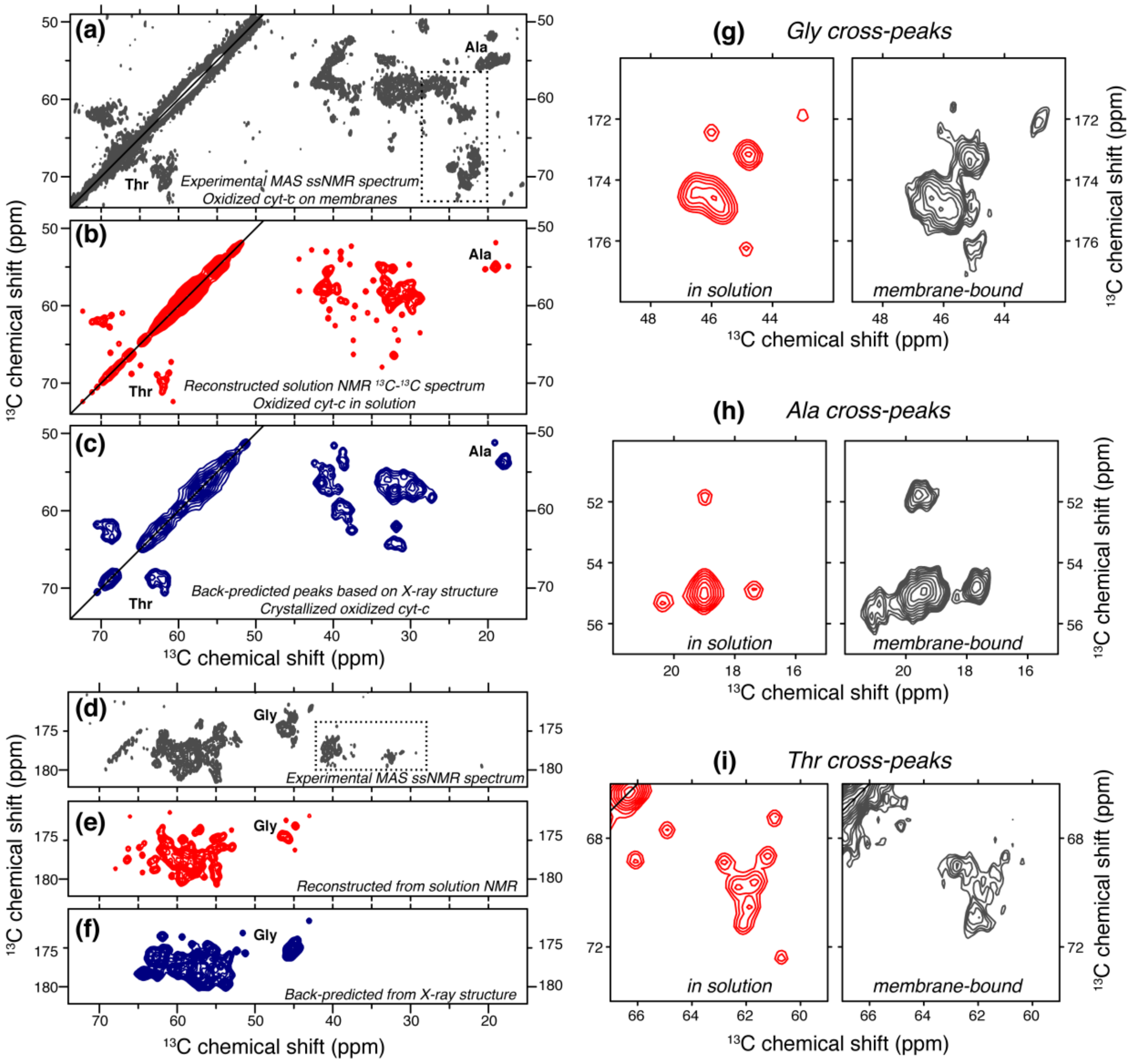

Figure B.6. Comparisons of NMR shifts for the membrane-bound and soluble states of cyt-c

(a,d) Experimental MAS ssNMR ^{13}C-^{13}C spectral regions focusing on the C^{α}-C^{β} and C'-C^{α} cross-peaks (data from *Figure 3.4*). (b,e) Corresponding areas of synthetic spectrum created from the known solution NMR shifts of oxidized cyt-c (BMRB entry 5828; ref. [132]). Utilities in the NMRPipe software suite were used to plot C^{α}-C^{β}/C^{β}-C^{α} cross peaks (b), C'-C^{α} cross peaks (e) and diagonal peak patterns. Well-separated Thr, Gly, and Ala peak groups are indicated. (c,f) Synthetic spectrum created from estimated chemical shifts predicted by the SPARTA+ program [144] based on the known X-ray structure of oxidized cyt-c (PDB entry 1HRC; ref. [16]). The dashed boxes in (a,d) mark peaks that were not included in the simulations used to create the synthetic spectra. (g-i) Enlarged sections from (b/e) and (a/d) panels, highlighting Gly, Ala, and Thr resonances.

APPENDIX C

SUPPLEMENTARY INFORMATION FOR CHAPTER 4

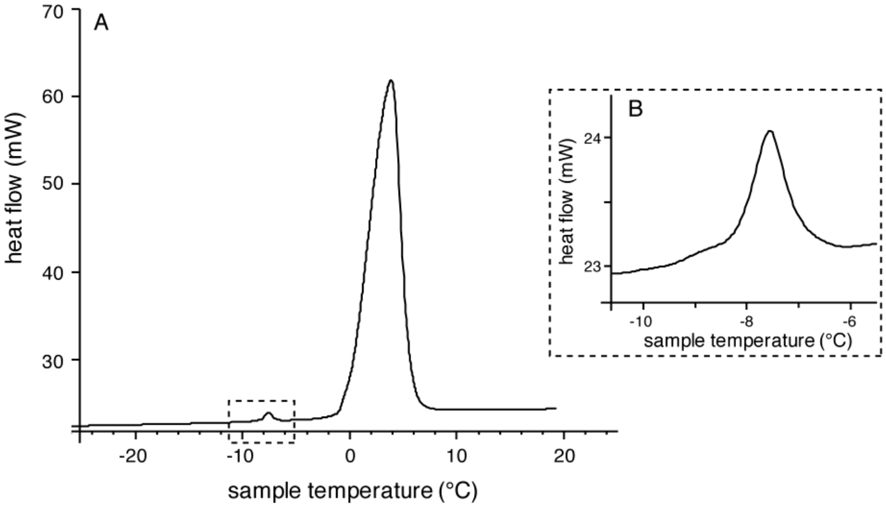

Figure C.7. Differential scanning calorimetry (DSC) of hydrated TOCL

(A) TOCL MLVs, hydrated in excess water, were submitted to DSC measurements using a scanning rate of 2 °C/min. Panel (A) shows the complete heating scan, which includes the TOCL melting transition T_m (boxed) as well as the melting of the water solvent. (B) Enlargement of the lipid transition, showing the TOCL T_m at -8.4 °C. We were unable to locate a prior report of the T_m of TOCL, but note that prior reports on other CL species showed a similar pattern of a CL T_m that is higher than the T_m of the corresponding PC variant (i.e. DOPC in this case) [231, 232].

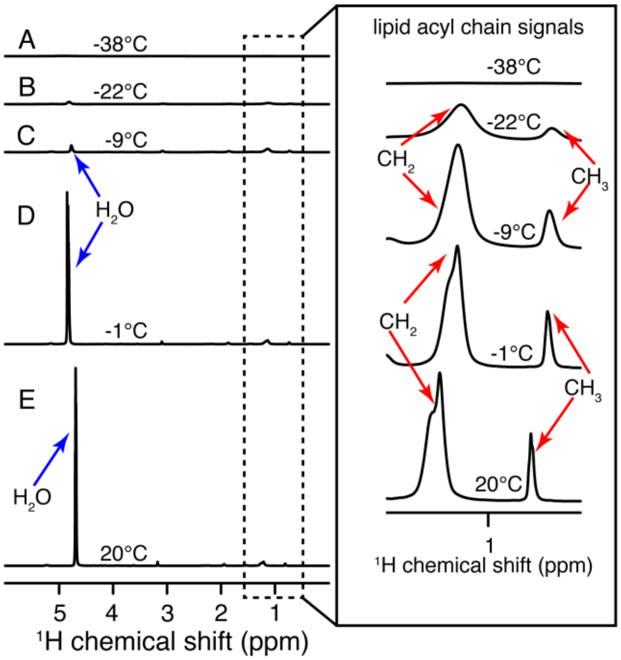

Figure C.8. Heating runs for MAS ^1H NMR analysis of DOPC/TOCL MLVs

(A) At -38 °C all ^1H peaks are broadened beyond detection. (B) At -22 °C: the water shows up as a low intensity, very broad peak (~4.8 ppm), indicating that most of the water is frozen. Lipid CH_2 and CH_3 peaks become visible but are still strongly attenuated. (C) At -9 °C: The water signal is still attenuated, but lipid acyl chain signals have returned to almost full intensity. (D) At -1 °C: Both water and lipid peaks are now narrow and intense indicating liquid-like motion. (E) At room temperature the peaks remain narrow. The inset to the right shows enlarged versions of the lipid acyl chain peaks. The measurements were performed at 750 MHz.

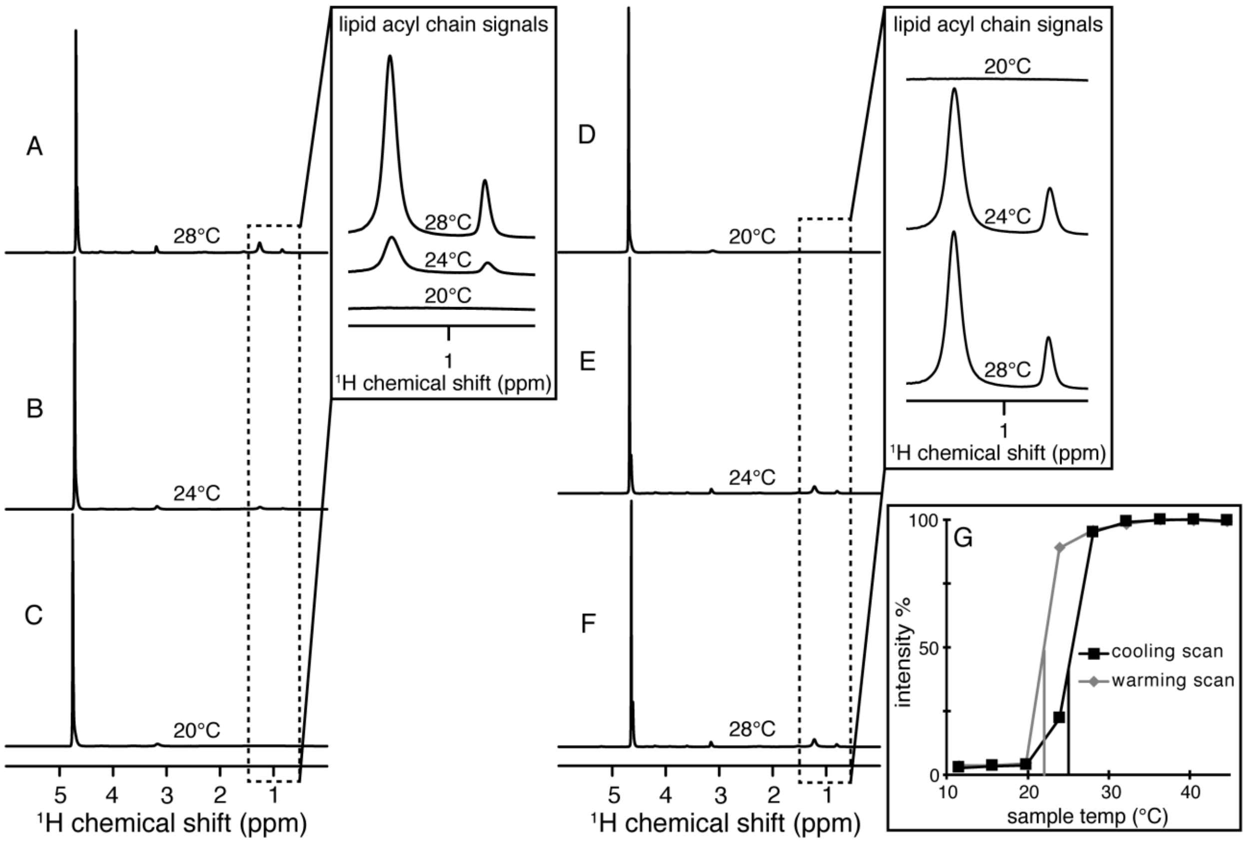

Figure C.9. Heating and cooling runs for hydrated DMPC MLVs

(A-C) ^{1}H MAS NMR spectra from the cooling run show that the transition occurs between 28 and 20 °C. (D-F) Spectra from the warming run show the transition between 20 and 24 °C. (G) Temperature dependent peak heights for lipid acyl chain CH_2 peaks. The transition mid-points in the cooling and heating scans occur at 25 and 22 °C, respectively. All spectra were acquired at 750 MHz.

BIBLIOGRAPHY

1. Montero, J., et al., *Cholesterol and peroxidized cardiolipin in mitochondrial membrane properties, permeabilization and cell death.* Biochim. Biophys. Acta, 2010. **1797**(6-7): p. 1217-1224.
2. Garrido, C., et al., *Mechanisms of cytochrome c release from mitochondria.* Cell Death Differ., 2006. **13**(9): p. 1423-1433.
3. Puchkov, M.N., et al., *Cytochrome c produces pores in cardiolipin-containing planar bilayer lipid membranes in the presence of hydrogen peroxide.* Biochim. Biophys. Acta, 2013. **1828**(2): p. 208-212.
4. Okouchi, M., et al., *Neuronal apoptosis in neurodegeneration.* Antioxid. Redox Signal., 2007. **9**(8): p. 1059-1096.
5. Wang, X., et al., *Inhibitors of cytochrome c release with therapeutic potential for Huntington's disease.* J. Neurosci., 2008. **28**(38): p. 9473-9485.
6. Indran, I.R., et al., *Recent advances in apoptosis, mitochondria and drug resistance in cancer cells.* BBA - Bioenergetics, 2011. **1807**(6): p. 735-745.
7. Fulda, S. and K.-M. Debatin, *Extrinsic versus intrinsic apoptosis pathways in anticancer chemotherapy*. Oncogene, 2006. **25**(34): p. 4798-4811.
8. Kagan, V.E., et al., *Cytochrome c acts as a cardiolipin oxygenase required for release of proapoptotic factors.* Nat. Chem. Biol., 2005. **1**(4): p. 223-232.
9. Elmore, S., *Apoptosis: a review of programmed cell death.* Toxicol. Pathol., 2007. **35**(4): p. 495-516.
10. Reubold, T.F., S. Wohlgemuth, and S. Eschenburg, *Crystal structure of full-length Apaf-1: how the death signal is relayed in the mitochondrial pathway of apoptosis.* Structure, 2011. **19**(8): p. 1074-1083.
11. Yuan, S., et al., *Structure of an apoptosome-procaspase-9 CARD complex.* Structure, 2010. **18**(5): p. 571-583.
12. Osman, C., D.R. Voelker, and T. Langer, *Making heads or tails of phospholipids in mitochondria.* J. Cell Biol., 2011. **192**(1): p. 7-16.
13. Kagan, V.E., et al., *Cytochrome c/cardiolipin relations in mitochondria: a kiss of death.* Free Radical Bio. Med., 2009. **46**(11): p. 1439-1453.
14. Mandal, A., et al., *Structural changes and proapoptotic peroxidase activity of cardiolipin-bound mitochondrial cytochrome c.* Biophys. J., 2015. **109**(9): p. 1873-1884.
15. Kapralov, A.A., et al., *Topography of tyrosine residues and their involvement in peroxidation of polyunsaturated cardiolipin in cytochrome c/cardiolipin peroxidase complexes.* Biochim. Biophys. Acta, 2011. **1808**(9): p. 2147-2155.
16. Bushnell, G.W., G.V. Louie, and G.D. Brayer, *High-resolution three-dimensional structure of horse heart cytochrome c.* J. Mol. Biol., 1990. **214**(2): p. 585-595.

17. Tekpli, X., et al., *Role for membrane remodeling in cell death: implication for health and disease.* Toxicology, 2013. **304**: p. 141-157.
18. van den Brink-van der Laan, E., J.A. Killian, and B. de Kruijff, *Nonbilayer lipids affect peripheral and integral membrane proteins via changes in the lateral pressure profile.* Biochim. Biophys. Acta, 2004. **1666**(1-2): p. 275-288.
19. Siegel, D.P. and R.M. Epand, *The mechanism of lamellar-to-inverted hexagonal phase transitions in phosphatidylethanolamine: implications for membrane fusion mechanisms.* Biophys. J., 1997. **73**(6): p. 3089-3111.
20. Antonov, V.F., et al., *Soft perforation of cardiolipin-containing planar lipid bilayer membrane by cytochrome c and* H_2O_2. Eur. Biophys. J., 2014. **43**(10-11): p. 469-476.
21. de Kruijff, B. and P.R. Cullis, *Cytochrome c specifically induces non-bilayer structures in cardiolipin-containing model membranes.* Biochim. Biophys. Acta, 1980. **602**(3): p. 477-490.
22. Vigh, L., B. Maresca, and J.L. Harwood, *Does the membrane's physical state control the expression of heat shock and other genes?* Trends Biochem. Sci., 1998. **23**(10): p. 369-374.
23. Wolfe, J. and G. Bryant, *Freezing, drying, and/or vitrification of membrane- solute-water systems.* Cryobiology, 1999. **39**(2): p. 103-129.
24. Bryant, G., K.L. Koster, and J. Wolfe, *Membrane behaviour in seeds and other systems at low water content: the various effects of solutes.* Seed Sci. Res., 2001.
25. Mandal, A. and P.C.A. van der Wel, *MAS* ^1H *NMR probes freezing point depression of water and liquid-gel phase transitions in liposomes.* Biophys. J., 2016. **111**(9): p. 1965-1973.
26. Foster, M.P., C.A. McElroy, and C.D. Amero, *Solution NMR of large molecules and assemblies.* Biochemistry, 2007. **46**(2): p. 331-340.
27. Smith, I.C.P. and I.H. Ekiel, *Phosphorus-31 NMR of phospholipids in membranes*, in *Phosphorous-31 NMR: Principles and Applications*, D.G. Gorenstein, Editor. 1984, Academic Press, Inc: Orlando, FL.
28. Metz, G., X.L. Wu, and S.O. Smith, *Ramped-amplitude cross polarization in magic-angle-spinning NMR.* J. Magn. Reson. Ser. A, 1994. **110**(2): p. 219-227.
29. Bennett, A.E., et al., *Heteronuclear decoupling in rotating solids.* J. Chem. Phys., 1995. **103**(16): p. 6951-6958.
30. Morris, G.A. and R. Freeman, *Enhancement of nuclear magnetic resonance signals by polarization transfer.* J. Am. Chem. Soc., 1979. **101**(3): p. 760-762.
31. Sattler, M., J. Schleucher, and C. Griesinger, *Heteronuclear multidimensional NMR experiments for the structure determination of proteins in solution.* Prog. Nucl. Magn. Reson. Spectrosc., 1999. **34**: p. 93-158.
32. Wang, S. and V. Ladizhansky, *Recent advances in magic angle spinning solid state NMR of membrane proteins.* Prog. Nucl. Magn. Reson. Spectrosc., 2014. **82**: p. 1-26.
33. Porcelli, F., et al., *On the role of NMR spectroscopy for characterization of antimicrobial peptides.*, in *Membrane Proteins*, G. Ghirlanda and A. Senes, Editors. 2013, Humana Press. p. 159-180.
34. Loquet, A., B. Habenstein, and A. Lange, *Structural investigations of molecular machines by solid-state NMR.* Acc. Chem. Res., 2013. **46**(9): p. 2070-2079.
35. Nishiyama, Y., *Fast magic-angle sample spinning solid-state NMR at 60-100kHz for natural abundance samples.* Solid State Nucl. Magn. Reson., 2016. **78**: p. 24-36.

36. Ravera, E., et al., *NMR of sedimented, fibrillized, silica-entrapped and microcrystalline (metallo)proteins.* J. Magn. Reson., 2015. **253**: p. 60-70.
37. Weingarth, M. and M. Baldus, *Solid-state NMR-based approaches for supramolecular structure elucidation.* Acc. Chem. Res., 2013. **46**(9): p. 2037-2046.
38. Demers, J.-P., V. Chevelkov, and A. Lange, *Progress in correlation spectroscopy at ultra-fast magic-angle spinning: basic building blocks and complex experiments for the study of protein structure and dynamics.* Solid State Nucl. Magn. Reson., 2011. **40**(3): p. 101-113.
39. Grant, C.V., C.H. Wu, and S.J. Opella, *Probes for high field solid-state NMR of lossy biological samples.* J. Magn. Reson., 2010. **204**(2): p. 180-188.
40. Dillmann, B., et al., *A novel low-E field coil to minimize heating of biological samples in solid-state multinuclear NMR experiments.* J. Magn. Reson., 2007. **187**(1): p. 10-18.
41. Higman, V.A., et al., *Assigning large proteins in the solid state: a MAS NMR resonance assignment strategy using selectively and extensively ^{13}C-labelled proteins.* J. Biomol. NMR, 2009. **44**(4): p. 245-260.
42. Zhang, Z., et al., *Solid-state NMR shows that dynamically different domains of membrane proteins have different hydration dependence.* J. Phys. Chem. B, 2014. **118**(32): p. 9553-9564.
43. Schirò, G., et al., *Translational diffusion of hydration water correlates with functional motions in folded and intrinsically disordered proteins.* Nat. Commun., 2015. **6**: p. 6490.
44. Khodadadi, S., et al., *Dynamics of biological macromolecules: not a simple slaving by hydration water.* Biophys. J., 2010. **98**(7): p. 1321-1326.
45. Ball, P., *Water as an active constituent in cell biology.* Chem. Rev., 2008. **108**(1): p. 74-108.
46. Gallat, F.X., et al., *Dynamical coupling of intrinsically disordered proteins and their hydration water: comparison with folded soluble and membrane proteins.* Biophys. J., 2012. **103**(1): p. 129-136.
47. Gawrisch, K., et al., *Hydration of POPC bilayers studied by ^{1}H-PFG-MAS-NOESY and neutron diffraction.* Eur. Biophys. J., 2007. **36**(4-5): p. 281-291.
48. Ulrich, A.S. and A. Watts, *Molecular response of the lipid headgroup to bilayer hydration monitored by ^{2}H-NMR.* Biophys. J., 1994. **66**(5): p. 1441-1449.
49. Tang, H., et al., *^{13}C MAS NMR studies of the effects of hydration on the cell walls of potatoes and chinese water chestnuts.* J. Agric. Food Chem., 1999. **47**(2): p. 510-517.
50. Bertini, I., et al., *SedNMR: on the edge between solution and solid-state NMR.* Acc. Chem. Res., 2013. **46**(9): p. 2059-2069.
51. Böckmann, A. and B. Meier, *Prions.* Prion, 2014. **4**(2): p. 72-79.
52. Martin, R.W. and K.W. Zilm, *Preparation of protein nanocrystals and their characterization by solid state NMR.* J. Magn. Reson., 2003.
53. Petkova, A.T., et al., *A structural model for Alzheimer's β-amyloid fibrils based on experimental constraints from solid state NMR.* Proc. Natl. Acad. Sci. U.S.A., 2002. **99**(26): p. 16742-16747.
54. Antzutkin, O.N., et al., *Multiple quantum solid-state NMR indicates a parallel, not antiparallel, organization of β-sheets in Alzheimer's β-amyloid fibrils.* Proc. Natl. Acad. Sci. U.S.A., 2000. **97**(24): p. 13045-13050.
55. Verel, R., et al., *Polymorphism in an amyloid-like fibril-forming model peptide.* Angew. Chem. Int. Ed., 2008. **47**(31): p. 5842-5845.

56. Kloepper, K.D., et al., *Solid-state NMR spectroscopy reveals that water is nonessential to the core structure of α-synuclein fibrils.* J. Phys. Chem. B, 2007. **111**(47): p. 13353-13356.
57. Vilar, M., et al., *The fold of α-synuclein fibrils.* Proc. Natl. Acad. Sci. U.S.A., 2008. **105**(25): p. 8637-8642.
58. Sharpe, S., W.-M. Yau, and R. Tycko, *Structure and dynamics of the HIV-1 Vpu transmembrane domain revealed by solid-state NMR with magic-angle spinning.* Biochemistry, 2006. **45**(3): p. 918-933.
59. Das, N., D.T. Murray, and T.A. Cross, *Lipid bilayer preparations of membrane proteins for oriented and magic-angle spinning solid-state NMR samples.* Nat. Protoc., 2013. **8**(11): p. 2256-2270.
60. Hisao, G.S., et al., *An efficient method and device for transfer of semisolid materials into solid-state NMR spectroscopy rotors.* J. Magn. Reson., 2016. **265**: p. 172-176.
61. van der Wel, P.C.A., J.R. Lewandowski, and R.G. Griffin, *Solid-state NMR study of amyloid nanocrystals and fibrils formed by the peptide GNNQQNY from yeast prion protein Sup35p.* J. Am. Chem. Soc., 2007. **129**(16): p. 5117-5130.
62. Sivanandam, V.N., et al., *The aggregation-enhancing huntingtin N-terminus is helical in amyloid fibrils.* J. Am. Chem. Soc., 2011. **133**(12): p. 4558-4566.
63. Li, J., et al., *Amyloid-like fibrils from a domain-swapping protein feature a parallel, in-register conformation without native-like interactions.* J. Biol. Chem., 2011. **286**(33): p. 28988-28995.
64. Hoop, C.L., et al., *Huntingtin exon 1 fibrils feature an interdigitated β-hairpin-based polyglutamine core.* Proc. Natl. Acad. Sci. U.S.A., 2016. **113**(6): p. 1546-1551.
65. Hoop, C.L., et al., *Structural characterization of the caveolin scaffolding domain in association with cholesterol-rich membranes.* Biochemistry, 2012. **51**(1): p. 90-99.
66. Hoop, C.L., et al., *Polyglutamine amyloid core boundaries and flanking domain dynamics in huntingtin fragment fibrils determined by solid-state nuclear magnetic resonance.* Biochemistry, 2014. **53**(42): p. 6653-6666.
67. Merg, A.D., et al., *Peptide-directed assembly of single-helical gold nanoparticle superstructures exhibiting intense chiroptical activity.* J. Am. Chem. Soc., 2016: p. jacs.6b07322.
68. Böckmann, A., et al., *Characterization of different water pools in solid-state NMR protein samples.* J. Biomol. NMR, 2009. **45**(3): p. 319-327.
69. Gardiennet, C., et al., *A sedimented sample of a 59 kDa dodecameric helicase yields high-resolution solid-state NMR spectra.* Angew. Chem. Int. Ed., 2012. **51**(31): p. 7855-7858.
70. Van Melckebeke, H., et al., *Probing water accessibility in HET-s(218-289) amyloid fibrils by solid-state NMR.* J. Mol. Biol., 2011. **405**(3): p. 765-772.
71. Bertini, I., et al., *Solid-state NMR of proteins sedimented by ultracentrifugation.* Proc. Natl. Acad. Sci. U.S.A., 2011. **108**(26): p. 10396-10399.
72. Mainz, A., et al., *Large protein complexes with extreme rotational correlation times investigated in solution by magic-angle-spinning NMR spectroscopy.* J. Am. Chem. Soc., 2009. **131**(44): p. 15968-15969.
73. Bertini, I., et al., *On the use of ultracentrifugal devices for sedimented solute NMR.* J. Biomol. NMR, 2012. **54**(2): p. 123-127.

74. White, E.T., et al., *The density of a protein crystal.* Powder Technol., 2007. **179**(1-2): p. 55-58.
75. Bell, D.J., et al., *The density of protein precipitates and its effect on centrifugal sedimentation.* Biotechnol. Bioeng., 1982. **24**(1): p. 127-141.
76. Schmidt, H.L.F., et al., *NMR determination of protein pKa values in the solid state.* J. Phys. Chem. Lett., 2010. **1**(10): p. 1623-1628.
77. Gelis, I., et al., *Solid-state NMR enhanced by dynamic nuclear polarization as a novel tool for ribosome structural biology.* J. Biomol. NMR, 2013. **56**(2): p. 85-93.
78. Scalise, M., et al., *Proteoliposomes as tool for assaying membrane transporter functions and interactions with xenobiotics.* Pharmaceutics, 2013. **5**(3): p. 472-497.
79. Veshaguri, S., et al., *Direct observation of proton pumping by a eukaryotic P-type ATPase.* Science, 2016. **351**(6280): p. 1469-1473.
80. LeBarron, J. and E. London, *Effect of lipid composition and amino acid sequence upon transmembrane peptide-accelerated lipid transleaflet diffusion (flip-flop).* Biochim. Biophys. Acta, 2016. **1858**(8): p. 1812-1820.
81. Narayanan, T., et al., *pHLIP® peptide interaction with membrane monitored by SAXS.* J. Phys. Chem. B, 2016.
82. Stepanyants, N., et al., *Cardiolipin's propensity for phase transition and its reorganization by dynamin-related protein 1 form a basis for mitochondrial membrane fission.* Mol. Biol. Cell, 2015. **26**(17): p. 3104-3116.
83. New, R.R.C., *Influence of liposome characteristics on their properties and fate*, in *Liposomes as Tools in Basic Research and Industry*, J.R. Philippot and F. Schuber, Editors. 1994, CRC Press. p. 3-20.
84. Sharma, A. and U.S. Sharma, *Liposomes in drug delivery: progress and limitations.* Int. J. Pharm., 1997. **154**(2): p. 123-140.
85. Tortorella, D., N.D. Ulbrandt, and E. London, *Simple centrifugation method for efficient pelleting of both small and large unilamellar vesicles that allows convenient measurement of protein binding.* Biochemistry, 1993. **32**(35): p. 9181-9188.
86. Tortorella, D. and E. London, *Method for efficient pelleting of small unilamellar model membrane vesicles.* Anal. Biochem., 1994. **217**(2): p. 176-180.
87. Abe, M., et al., *Molecular mechanisms for the induction of peroxidase activity of the cytochrome c-cardiolipin complex.* Biochemistry, 2011. **50**(39): p. 8383-8391.
88. Zschörnig, O., et al., *Modulation of lysozyme charge influences interaction with phospholipid vesicles.* Colloids Surf. B, 2005. **42**(1): p. 69-78.
89. van der Wel, P.C.A., J.R. Lewandowski, and R.G. Griffin, *Structural characterization of GNNQQNY amyloid fibrils by magic angle spinning NMR.* Biochemistry, 2010. **49**(44): p. 9457-9469.
90. Li, J. and P.C.A. van der Wel, *Spinning-rate encoded chemical shift correlations from rotational resonance solid-state NMR experiments.* J. Magn. Reson., 2013. **230**: p. 117-124.
91. Cai, H., et al., *High-resolution ^1H NMR spectroscopy of fish muscle, eggs and small whole fish via Hadamard-encoded intermolecular multiple-quantum coherence.* PLoS ONE, 2014. **9**(1): p. e86422.
92. Renault, M., et al., *Slow-spinning low-sideband HR-MAS NMR spectroscopy: delicate analysis of biological samples.* Sci. Rep., 2013. **3**: p. 3349.

93. Han, Y., et al., *Solid-state NMR studies of HIV-1 capsid protein assemblies.* J. Am. Chem. Soc., 2010. **132**(6): p. 1976-1987.
94. Chimon, S., et al., *Evidence of fibril-like β-sheet structures in a neurotoxic amyloid intermediate of Alzheimer's β-amyloid.* Nat. Struct. Mol. Biol., 2007. **14**(12): p. 1157-1164.
95. Chimon, S. and Y. Ishii, *Capturing intermediate structures of Alzheimer's β-amyloid, Aβ(1-40), by solid-state NMR spectroscopy.* J. Am. Chem. Soc., 2005. **127**(39): p. 13472-13473.
96. Comellas, G., et al., *Structured regions of α-synuclein fibrils include the early-onset Parkinson's disease mutation sites.* J. Mol. Biol., 2011. **411**(4): p. 881-895.
97. Tuttle, M.D., et al., *Preparation of amyloid fibrils for magic-angle spinning solid-state NMR spectroscopy*, in *Protein Amyloid Aggregation*, D. Eliezer, Editor. 2016, Springer New York. p. 173-183.
98. van Loo, G., et al., *The role of mitochondrial factors in apoptosis: a Russian roulette with more than one bullet.* Cell Death Differ., 2002. **9**(10): p. 1031-1042.
99. Xun, Z., et al., *Targeting of XJB-5-131 to mitochondria suppresses oxidative DNA damage and motor decline in a mouse model of Huntington's disease.* Cell Rep., 2012. **2**(5): p. 1137-1142.
100. Schug, Z.T. and E. Gottlieb, *Cardiolipin acts as a mitochondrial signalling platform to launch apoptosis.* Biochim. Biophys. Acta, 2009. **1788**(10): p. 2022-2031.
101. Garcia Fernandez, M., et al., *Early changes in intramitochondrial cardiolipin distribution during apoptosis.* Cell Growth Differ., 2002. **13**(9): p. 449-455.
102. Scorrano, L., et al., *A distinct pathway remodels mitochondrial cristae and mobilizes cytochrome c during apoptosis.* Dev. Cell, 2002. **2**(1): p. 55-67.
103. Eckmann, J., et al., *Mitochondria: mitochondrial membranes in brain ageing and neurodegeneration.* Int. J. Biochem. Cell Biol., 2013. **45**(1): p. 76-80.
104. Epand, R.F., et al., *The apoptotic protein tBid promotes leakage by altering membrane curvature.* J. Biol. Chem., 2002. **277**(36): p. 32632-32639.
105. Gonzalvez, F. and E. Gottlieb, *Cardiolipin: setting the beat of apoptosis.* Apoptosis, 2007. **12**(5): p. 877-885.
106. Kagan, V.E., et al., *Mitochondrial targeting of electron scavenging antioxidants: Regulation of selective oxidation vs random chain reactions.* Adv. Drug Deliver. Rev., 2009. **61**(14): p. 1375-1385.
107. Brown, L.R. and K. Wüthrich, *A spin label study of lipid oxidation catalyzed by heme proteins.* Biochim. Biophys. Acta, 1977. **464**(2): p. 356-369.
108. Kagan, V.E., et al., *Cardiolipin signaling mechanisms: collapse of asymmetry and oxidation.* Antioxid. Redox Signal., 2015. **22**(18): p. 1667-1680.
109. Spooner, P.J. and A. Watts, *Reversible unfolding of cytochrome c upon interaction with cardiolipin bilayers. 1. Evidence from deuterium NMR measurements.* Biochemistry, 1991. **30**(16): p. 3871-3879.
110. Spooner, P.J. and A. Watts, *Reversible unfolding of cytochrome c upon interaction with cardiolipin bilayers. 2. Evidence from phosphorus-31 NMR measurements.* Biochemistry, 1991. **30**(16): p. 3880-3885.
111. Hong, Y., et al., *Origin of the conformational heterogeneity of cardiolipin-bound cytochrome c.* J. Am. Chem. Soc., 2012. **134**(45): p. 18713-18723.

112. Hanske, J., et al., *Conformational properties of cardiolipin-bound cytochrome c.* Proc. Natl. Acad. Sci. U.S.A., 2012. **109**(1): p. 125-130.
113. Bernabeu, A., L.M. Contreras, and J. Villalaín, *Two-dimensional infrared correlation spectroscopy study of the interaction of oxidized and reduced cytochrome c with phospholipid model membranes.* Biochim. Biophys. Acta, 2007. **1768**(10): p. 2409-2420.
114. Choi, S. and J.M. Swanson, *Interaction of cytochrome c with cardiolipin: an infrared spectroscopic study.* Biophys. Chem., 1995. **54**(3): p. 271-278.
115. Rytömaa, M. and P.K.J. Kinnunen, *Reversibility of the binding of cytochrome c to liposomes. Implications for lipid-protein interactions.* J. Biol. Chem., 1995. **270**(7): p. 3197-3202.
116. Kalanxhi, E. and C.J.A. Wallace, *Cytochrome c impaled: investigation of the extended lipid anchorage of a soluble protein to mitochondrial membrane models.* Biochem. J., 2007. **407**(2): p. 179-187.
117. Tuominen, E.K.J., C.J.A. Wallace, and P.K.J. Kinnunen, *Phospholipid-cytochrome c interaction: evidence for the extended lipid anchorage.* J. Biol. Chem., 2002. **277**(11): p. 8822-8826.
118. Sinibaldi, F., et al., *Extended cardiolipin anchorage to cytochrome c: a model for protein-mitochondrial membrane binding.* J. Biol. Inorg. Chem., 2010. **15**(5): p. 689-700.
119. McClelland, L.J., et al., *Structure of a mitochondrial cytochrome c conformer competent for peroxidase activity.* Proc. Natl. Acad. Sci. U.S.A., 2014. **111**(18): p. 6648-6653.
120. Lan, W., et al., *Structural basis for cytochrome c Y67H mutant to function as a peroxidase.* PLoS ONE, 2014. **9**(9): p. e107305.
121. Watts, A., *Solid-state NMR approaches for studying the interaction of peptides and proteins with membranes.* Biochim. Biophys. Acta, 1998. **1376**(3): p. 297-318.
122. Hong, M., Y. Zhang, and F. Hu, *Membrane protein structure and dynamics from NMR spectroscopy.* Annu Rev Phys Chem, 2012. **63**: p. 1-24.
123. Eddy, M.T., et al., *Lipid dynamics and protein-lipid interactions in 2D crystals formed with the β-barrel integral membrane protein VDAC1.* J. Am. Chem. Soc., 2012. **134**(14): p. 6375-6387.
124. van der Wel, P.C.A., *Lipid dynamics and protein-lipid interactions in integral membrane proteins: insights from solid-state NMR.* eMagRes, 2014. **3**: p. 111-118.
125. Wylie, B.J., M.P. Bhate, and A.E. McDermott, *Transmembrane allosteric coupling of the gates in a potassium channel.* Proc. Natl. Acad. Sci. U.S.A., 2014. **111**(1): p. 185-190.
126. Waltham, M.C., B.A. Cornell, and R. Smith, *Association of ferri- and ferro-cytochrome c with lipid multilayers: a ^{31}P solid-state NMR study.* Biochim. Biophys. Acta, 1986. **862**(2): p. 451-456.
127. Spooner, P.J. and A. Watts, *Cytochrome c interactions with cardiolipin in bilayers: a multinuclear magic-angle spinning NMR study.* Biochemistry, 1992. **31**(41): p. 10129-10138.
128. Spooner, P.J., et al., *Dynamics in a protein-lipid complex: nuclear magnetic resonance measurements on the headgroup of cardiolipin when bound to cytochrome c.* Biophys. J., 1993. **65**(1): p. 106-112.
129. Pinheiro, T.J. and A. Watts, *Resolution of individual lipids in mixed phospholipid membranes and specific lipid-cytochrome c interactions by magic-angle spinning solid-state phosphorus-31 NMR.* Biochemistry, 1994. **33**(9): p. 2459-2467.

130. Kim, S.-m., et al., *The interactions of ferric and ferrous cytochrome c with cardiolipin in phospholipid membranes studied by solid-state ^{2}H and ^{31}P NMR.* J. Mol. Struct., 1998. **441**(2-3): p. 183-188.
131. Rumbley, J.N., L. Hoang, and S.W. Englander, *Recombinant equine cytochrome c in escherichia coli: high-level expression, characterization, and folding and assembly mutants.* Biochemistry, 2002. **41**(47): p. 13894-13901.
132. Liu, W., et al., *Backbone and side-chain heteronuclear resonance assignments and hyperfine NMR shifts in horse cytochrome c.* Protein Sci., 2003. **12**(9): p. 2104-2108.
133. Pollock, W.B.R., et al., *Bacterial expression of a mitochondrial cytochrome c. Trimethylation of Lys72 in yeast iso-1-cytochrome c and the alkaline conformational transition.* Biochemistry, 1998. **37**(17): p. 6124-6131.
134. Takegoshi, K., S. Nakamura, and T. Terao, *^{13}C–^{1}H dipolar-assisted rotational resonance in magic-angle spinning NMR.* Chem. Phys. Lett., 2001.
135. Dvinskikh, S.V., V. Castro, and D. Sandström, *Heating caused by radiofrequency irradiation and sample rotation in ^{13}C magic angle spinning NMR studies of lipid membranes.* Magn. Reson. Chem., 2004. **42**(10): p. 875-881.
136. Thurber, K.R. and R. Tycko, *Measurement of sample temperatures under magic-angle spinning from the chemical shift and spin-lattice relaxation rate of ^{79}Br in KBr powder.* J. Magn. Reson., 2009. **196**(1): p. 84-87.
137. Delaglio, F., et al., *NMRPipe: A multidimensional spectral processing system based on UNIX pipes.* J. Biomol. NMR, 1995. **6**(3): p. 1-18.
138. Stevens, T.J., et al., *A software framework for analysing solid-state MAS NMR data.* J. Biomol. NMR, 2011. **51**(4): p. 437-447.
139. Vranken, W.F., et al., *The CCPN data model for NMR spectroscopy: development of a software pipeline.* Proteins, 2005. **59**(4): p. 687-696.
140. Harris, R.K., et al., *Further conventions for NMR shielding and chemical shifts (IUPAC recommendations 2008).* Magn. Reson. Chem., 2008. **46**(6): p. 582-598.
141. Zorin, V., et al., *Heteronuclear chemical shift correlation and J-resolved MAS NMR spectroscopy of lipid membranes.* Magn. Reson. Chem., 2010. **48**(12): p. 925-934.
142. Tang, M., A.J. Waring, and M. Hong, *Effects of arginine density on the membrane-bound structure of a cationic antimicrobial peptide from solid-state NMR.* BBA - Biomembranes, 2009. **1788**(2): p. 514-521.
143. Morcombe, C.R. and K.W. Zilm, *Chemical shift referencing in MAS solid state NMR.* J. Magn. Reson. Ser. A, 2003. **162**(2): p. 479-486.
144. Shen, Y. and A. Bax, *SPARTA+: a modest improvement in empirical NMR chemical shift prediction by means of an artificial neural network.* J. Biomol. NMR, 2010. **48**(1): p. 13-22.
145. Margoliash, E. and N. Frohwirt, *Spectrum of horse-heart cytochrome c.* Biochem. J., 1959. **71**(3): p. 570-572.
146. Zhou, M., et al., *A stable nonfluorescent derivative of resorufin for the fluorometric determination of trace hydrogen peroxide: applications in detecting the activity of phagocyte NADPH oxidase and other oxidases.* Anal. Biochem., 1997. **253**(2): p. 162-168.
147. Wang, T., S.D. Cady, and M. Hong, *NMR determination of protein partitioning into membrane domains with different curvatures and application to the influenza M2 peptide.* Biophys. J., 2012. **102**(4): p. 787-794.

148. Zhong, L., et al., *Solid-state NMR spectroscopy of 18.5 kDa myelin basic protein reconstituted with lipid vesicles: spectroscopic characterisation and spectral assignments of solvent-exposed protein fragments.* Biochim. Biophys. Acta, 2007. **1768**(12): p. 3193-3205.
149. Berghuis, A.M. and G.D. Brayer, *Oxidation state-dependent conformational changes in cytochrome c.* J. Mol. Biol., 1992. **223**(4): p. 959-976.
150. Volkov, A.N., et al., *Redox-dependent conformational changes in eukaryotic cytochromes revealed by paramagnetic NMR spectroscopy.* J. Biomol. NMR, 2012. **52**(3): p. 245-256.
151. Letellier, L. and E. Shechter, *Correlations between structure and spectroscopic properties in membrane model system. Fluorescence and circular dichroism of the cytochrome c-cardiolipin system.* Eur. J. Biochem., 1973. **40**(2): p. 507-512.
152. Oldfield, E. and A. Allerhand, *Cytochrome c: observation of numerous single-carbon sites of the reduced and oxidized species by means of natural-abundance* ^{13}C *nuclear magnetic resonance spectroscopy.* Proc. Natl. Acad. Sci. U.S.A., 1973. **70**(12): p. 3531-3535.
153. Luca, S., et al., *Secondary chemical shifts in immobilized peptides and proteins: a qualitative basis for structure refinement under magic angle spinning.* J. Biomol. NMR, 2001. **20**(4): p. 325-331.
154. Heimburg, T. and D. Marsh, *Investigation of secondary and tertiary structural changes of cytochrome c in complexes with anionic lipids using amide hydrogen exchange measurements: an FTIR study.* Biophys. J., 1993. **65**(6): p. 2408-2417.
155. Reis, O., R. Winter, and T.W. Zerda, *The effect of high external pressure on DPPC-cholesterol multilamellar vesicles: a pressure-tuning Fourier transform infrared spectroscopy study.* Biochim. Biophys. Acta, 1996. **1279**(1): p. 5-16.
156. Bergstrom, C.L., et al., *Cytochrome c causes pore formation in cardiolipin-containing membranes.* Proc. Natl. Acad. Sci. U.S.A., 2013. **110**(16): p. 6269-6274.
157. van der Wel, P.C.A., et al., *Tryptophan-anchored transmembrane peptides promote formation of nonlamellar phases in phosphatidylethanolamine model membranes in a mismatch-dependent manner.* Biochemistry, 2000. **39**(11): p. 3124-3133.
158. Brumm, T., et al., *Macroscopic orientation effects in broadline NMR-spectra of model membranes at high magnetic field strength.* Biophys. J., 1992. **61**(4): p. 1018-1024.
159. Pott, T. and E.J. Dufourc, *Action of melittin on the DPPC-cholesterol liquid-ordered phase: a solid state* ^{2}H*-and* ^{31}P*-NMR study.* Biophys. J., 1995. **68**(3): p. 965-977.
160. Costello, A.L. and T.M. Alam, *Investigating the impact of cholesterol on magnetically aligned sphingomyelin/cholesterol multilamellar vesicles using static* ^{31}P *NMR.* Chem. Phys. Lipids, 2010. **163**(6): p. 506-513.
161. Pinheiro, T., M.J. Duer, and A. Watts, *Phospholipid headgroup dynamics in DOPG-d5-cytochrome c complexes as revealed by* ^{2}H *and* ^{31}P *NMR: The effects of a peripheral protein on collective lipid fluctuations.* Solid State Nucl. Magn. Reson., 1997. **8**(1): p. 55-64.
162. Belikova, N.A., et al., *Peroxidase activity and structural transitions of cytochrome c bound to cardiolipin-containing membranes.* Biochemistry, 2006. **45**(15): p. 4998-5009.
163. de Jongh, H.H.J., T. Ritsema, and J.A. Killian, *Lipid specificity for membrane mediated partial unfolding of cytochrome c.* FEBS Lett., 1995. **360**(3): p. 255-260.

164. Su, Y. and M. Hong, *Conformational disorder of membrane peptides investigated from solid-state NMR line widths and line shapes.* J. Phys. Chem. B, 2011. **115**(36): p. 10758-10767.
165. Krishna, M.M.G., et al., *Cooperative omega loops in cytochrome c: role in folding and function.* J. Mol. Biol., 2003. **331**(1): p. 29-36.
166. Su, Y., et al., *Membrane-bound dynamic structure of an arginine-rich cell-penetrating peptide, the protein transduction domain of HIV TAT, from solid-state NMR.* Biochemistry, 2010. **49**(29): p. 6009-6020.
167. Oellerich, S., et al., *Peripheral and integral binding of cytochrome c to phospholipids vesicles.* J. Phys. Chem. B, 2004. **108**(12): p. 3871-3878.
168. Rytömaa, M., P. Mustonen, and P.K.J. Kinnunen, *Reversible, nonionic, and pH-dependent association of cytochrome c with cardiolipin-phosphatidylcholine liposomes.* J. Biol. Chem., 1992. **267**(31): p. 22243-22248.
169. Heimburg, T. and D. Marsh, *Protein surface-distribution and protein-protein interactions in the binding of peripheral proteins to charged lipid membranes.* Biophys. J., 1995.
170. Rytömaa, M. and P.K.J. Kinnunen, *Evidence for two distinct acidic phospholipid-binding sites in cytochrome c.* J. Biol. Chem., 1994. **269**(3): p. 1770-1774.
171. Pinheiro, T.J., et al., *Structural and kinetic description of cytochrome c unfolding induced by the interaction with lipid vesicles.* Biochemistry, 1997. **36**(42): p. 13122-13132.
172. Zuckermann, M.J. and T. Heimburg, *Insertion and pore formation driven by adsorption of proteins onto lipid bilayer membrane-water interfaces.* Biophys. J., 2001. **81**(5): p. 2458-2472.
173. Gawrisch, K., N.V. Eldho, and L.L. Holte, *The structure of DHA in phospholipid membranes.* Lipids, 2003. **38**(4): p. 445-452.
174. Feller, S.E., K. Gawrisch, and A.D. MacKerell, *Polyunsaturated fatty acids in lipid bilayers: intrinsic and environmental contributions to their unique physical properties.* J. Am. Chem. Soc., 2002. **124**(2): p. 318-326.
175. Bachar, M., et al., *Molecular dynamics simulation of a polyunsaturated lipid bilayer susceptible to lipid peroxidation.* J. Phys. Chem. B, 2004. **108**(22): p. 7170-7179.
176. Marsh, D., *Lateral pressure profile, spontaneous curvature frustration, and the incorporation and conformation of proteins in membranes.* Biophys. J., 2007. **93**(11): p. 3884-3899.
177. Zhou, H.-X. and T.A. Cross, *Influences of membrane mimetic environments on membrane protein structures.* Annu. Rev. Biophys., 2013. **42**(1): p. 361-392.
178. Laganowsky, A., et al., *Membrane proteins bind lipids selectively to modulate their structure and function.* Nature, 2014. **510**(7503): p. 172-175.
179. Nagle, J.F. and S. Tristram-Nagle, *Structure of lipid bilayers.* Biochim. Biophys. Acta, 2000. **1469**(3): p. 159-195.
180. de Kruijff, B., *Lipid polymorphism and biomembrane function.* Curr. Opin. Chem. Biol., 1997. **1**(4): p. 564-569.
181. Aibara, S., et al., *Changes in positional distribution of fatty acids in the phospholipids of Escherichia coli after shift-down in temperature.* Biochim. Biophys. Acta, 1972. **270**(3): p. 301-306.
182. Weerkamp, A. and W. Heinen, *Effect of temperature on the fatty acid composition of the extreme thermophiles, Bacillus caldolyticus and Bacillus caldotenax.* J. Bacteriol., 1972. **109**(1): p. 443-446.

183. Huang, C.H., *Mixed-chain phospholipids: structures and chain-melting behavior.* Lipids, 2001. **36**(10): p. 1077-1097.
184. Koynova, R. and M. Caffrey, *Phases and phase transitions of the phosphatidylcholines.* BBA - Rev. Biomembranes, 1998. **1376**(1): p. 91-145.
185. Silvius, J.R., *Thermotropic phase transitions of pure lipids in model membranes and their modifications by membrane proteins*, in *Lipid-Protein Interactions*. 1982, John Wiley & Sons: New York.
186. Fenske, D.B. and P.R. Cullis, *Lipid polymorphism.* eMagRes, 2007.
187. Nowacka, A., et al., *Polarization transfer solid-state NMR for studying surfactant phase behavior.* Langmuir, 2010. **26**(22): p. 16848-16856.
188. Dufourc, E.J., et al., *Dynamics of phosphate head groups in biomembranes. Comprehensive analysis using phosphorus-31 nuclear magnetic resonance lineshape and relaxation time measurements.* Biophys. J., 1992. **61**(1): p. 42-57.
189. Gross, J.D., D.E. Warschawski, and R.G. Griffin, *Dipolar recoupling in MAS NMR: a probe for segmental order in lipid bilayers.* J. Am. Chem. Soc., 1997. **119**(4): p. 796-802.
190. Forbes, J., C. Husted, and E. Oldfield, *High-field, high-resolution proton "magic-angle" sample-spinning nuclear magnetic resonance spectroscopic studies of gel and liquid crystalline lipid bilayers and the effects of cholesterol.* J. Am. Chem. Soc., 1988. **110**(4): p. 1059-1065.
191. Polozov, I.V. and K. Gawrisch, *Characterization of the liquid-ordered state by proton MAS NMR.* Biophys. J., 2006. **90**(6): p. 2051-2061.
192. Holland, G.P. and T.M. Alam, *Multi-dimensional ^{1}H-^{13}C HETCOR and FSLG-HETCOR NMR study of sphingomyelin bilayers containing cholesterol in the gel and liquid crystalline states.* J. Magn. Reson. Ser. A, 2006. **181**(2): p. 316-326.
193. Purusottam, R.N., et al., *Probing the gel to liquid-crystalline phase transition and relevant conformation changes in liposomes by ^{13}C magic-angle spinning NMR spectroscopy.* Biochim. Biophys. Acta, 2015. **1848**(12): p. 3134-3139.
194. Hong, M., Y. Zhang, and F. Hu, *Membrane protein structure and dynamics from NMR spectroscopy.* Annu. Rev. Phys. Chem., 2012. **63**(1): p. 1-24.
195. Baker, L.A. and M. Baldus, *Characterization of membrane protein function by solid-state NMR spectroscopy.* Curr. Opin. Struc. Biol., 2014. **27**: p. 48-55.
196. Banigan, J.R., A. Gayen, and N.J. Traaseth, *Correlating lipid bilayer fluidity with sensitivity and resolution of polytopic membrane protein spectra by solid-state NMR spectroscopy.* BBA - Biomembranes, 2014.
197. Sarkar, R., et al., *An NMR thermometer for cryogenic magic-angle spinning NMR: the spin-lattice relaxation of ^{127}I in cesium iodide.* J. Magn. Reson., 2011. **212**(2): p. 460-463.
198. Cavanagh, J., et al., *Protein NMR Spectroscopy: Principles and Practice*. 2nd ed. 2010: Elsevier Science.
199. Tsukahara, T., et al., *NMR study of water molecules confined in extended nanospaces.* Angew. Chem. Int. Ed., 2007. **46**(7): p. 1180-1183.
200. Hansen, E.W., M. Stöcker, and R. Schmidt, *Low-temperature phase transition of water confined in mesopores probed by NMR. Influence on pore size distribution.* J. Phys. Chem., 1996. **100**(6): p. 2195-2200.
201. Lewandowski, J.R., et al., *Direct observation of hierarchical protein dynamics.* Science, 2015. **348**(6234): p. 578-581.

202. Kloepper, K.D., et al., *Temperature-dependent sensitivity enhancement of solid-state NMR spectra of α-synuclein fibrils.* J. Biomol. NMR, 2007. **39**(3): p. 197-211.
203. Christenson, H.K., *Confinement effects on freezing and melting.* J. Phys.: Condens. Matter, 2001. **13**(11): p. R95-R133.
204. Szyperski, T. and J.L. Mills, *NMR-based structural biology of proteins in supercooled water.* J. Struct. Funct. Genomics, 2011. **12**(1): p. 1-7.
205. Koschke, K., et al., *Freezing point depression in model Lennard-Jones solutions.* Mol. Phys., 2015. **113**(17-18): p. 2725-2734.
206. Doherty, T. and M. Hong, *2D ^{1}H-^{31}P solid-state NMR studies of the dependence of inter-bilayer water dynamics on lipid headgroup structure and membrane peptides.* J. Magn. Reson., 2009. **196**(1): p. 39-47.
207. Rand, R.P. and V.A. Parsegian, *Hydration forces between phospholipid bilayers.* BBA - Rev. Biomembranes, 1989. **988**(3): p. 351-376.
208. Nagle, J.F., et al., *Re-analysis of magic angle spinning nuclear magnetic resonance determination of interlamellar waters in lipid bilayer dispersions.* Biophys. J., 1999. **77**(4): p. 2062-2065.
209. Gleeson, J.T., S. Erramilli, and S.M. Gruner, *Freezing and melting water in lamellar structures.* Biophys. J., 1994. **67**(2): p. 706-712.
210. Potekhin, S.A., et al., *High pressure effect on the main transition from the ripple gel P'_{β} phase to the liquid crystal (L_{α}) phase in dipalmitoylphosphatidylcholine. Microcalorimetric study.* BBA - Biomembranes, 2008. **1778**(11): p. 2588-2593.
211. Tada, K., et al., *Barotropic and thermotropic bilayer phase behavior of positional isomers of unsaturated mixed-chain phosphatidylcholines.* BBA - Biomembranes, 2009. **1788**(5): p. 1056-1063.
212. Gawrisch, K. and H.C. Gaede, *Measurement of lateral diffusion rates in membranes by pulsed magnetic field gradient, magic angle spinning-proton nuclear magnetic resonance*, in *Methods in Membrane Lipids*, A.M. Dopico, Editor. 2007, Humana Press: Totowa, NJ. p. 257-265.
213. Janiak, M.J., D.M. Small, and G.G. Shipley, *Temperature and compositional dependence of the structure of hydrated dimyristoyl lecithin.* J. Biol. Chem., 1979. **254**(13): p. 6068-6078.
214. Smith, G., et al., *Structure of the L_{β} phases in a hydrated phosphatidylcholine multimembrane.* Phys. Rev. Lett., 1988. **60**(9): p. 813-816.
215. Faure, C., L. Bonakdar, and E.J. Dufourc, *Determination of DMPC hydration in the L_{α} and $L_{\beta'}$ phases by ^{2}H solid state NMR of D_2O.* FEBS Lett., 1997. **405**(3): p. 263-266.
216. Nowacka, A., et al., *Small polar molecules like glycerol and urea can preserve the fluidity of lipid bilayers under dry conditions.* Soft Matter, 2012. **8**(5): p. 1482-1491.
217. Kowalik, B., et al., *Combination of MD simulations with two-state kinetic rate modeling elucidates the chain melting transition of phospholipid bilayers for different hydration levels.* J. Phys. Chem. B, 2015. **119**(44): p. 14157-14167.
218. Knecht, V., A.E. Mark, and S.-J. Marrink, *Phase behavior of a phospholipid/fatty acid/water mixture studied in atomic detail.* J. Am. Chem. Soc., 2006. **128**(6): p. 2030-2034.
219. Coppock, P.S. and J.T. Kindt, *Determination of phase transition temperatures for atomistic models of lipids from temperature-dependent stripe domain growth kinetics.* J. Phys. Chem. B, 2010. **114**(35): p. 11468-11473.

220. Crowe, J.H., et al., *Interactions of sugars with membranes.* BBA - Rev. Biomembranes, 1988. **947**(2): p. 367-384.
221. Rudolph, A.S., J.H. Crowe, and L.M. Crowe, *Effects of 3 stabilizing agents proline, betaine, and trehalose on membrane phospholipids.* Arch. Biochem. Biophys., 1986. **245**(1): p. 134-143.
222. Green, J.L. and C.A. Angell, *Phase relations and vitrification in saccharide-water solutions and the trehalose anomaly.* J. Phys. Chem., 1989. **93**(8): p. 2880-2882.
223. Koster, K.L., et al., *Effects of vitrified and nonvitrified sugars on phosphatidylcholine fluid-to-gel phase transitions.* Biophys. J., 2000. **78**(4): p. 1932-1946.
224. Moiset, G., et al., *Disaccharides impact the lateral organization of lipid membranes.* J. Am. Chem. Soc., 2014. **136**(46): p. 16167-16175.
225. Renault, M., et al., *Solid-state NMR spectroscopy on cellular preparations enhanced by dynamic nuclear polarization.* Angew. Chem. Int. Ed., 2012. **51**(12): p. 2998-3001.
226. Kaplan, M., et al., *Probing a cell-embedded megadalton protein complex by DNP-supported solid-state NMR.* Nat. Methods, 2015. **12**(7): p. 649-652.
227. Wissing, S.A., O. Kayser, and R.H. Müller, *Solid lipid nanoparticles for parenteral drug delivery.* Adv. Drug Deliver. Rev., 2004. **56**(9): p. 1257-1272.
228. Kooijman, E.E., et al., *Magic angle spinning ^{31}P NMR spectroscopy reveals two essentially identical ionization states for the cardiolipin phosphates in phospholipid liposomes.* BBA - Biomembranes, 2017. **1859**(1): p. 61-68.
229. Zeng, L., et al., *Analyzing structural properties of heterogeneous cardiolipin-bound cytochrome c and their regulation by surface-enhanced infrared absorption spectroscopy.* Anal. Chem., 2016.
230. Kobayashi, H., S. Nagao, and S. Hirota, *Characterization of the cytochrome c membrane-binding site using cardiolipin-containing bicelles with NMR.* Angew. Chem., 2016. **128**(45): p. 14225-14228.
231. Lewis, R.N.A.H. and R.N. McElhaney, *The physicochemical properties of cardiolipin bilayers and cardiolipin-containing lipid membranes.* Biochim. Biophys. Acta, 2009. **1788**(10): p. 2069-2079.
232. Boscia, A.L., et al., *X-ray structure, thermodynamics, elastic properties and MD simulations of cardiolipin/dimyristoylphosphatidylcholine mixed membranes.* Chem. Phys. Lipids, 2014. **178**: p. 1-10.